2020

Cerium Oxide based Nanocomposites for Supercapacitors

Aadithya Jeyaranjan
University of Central Florida

CERIUM OXIDE BASED NANOCOMPOSITES FOR SUPERCAPACITORS

by

AADITHYA JEYARANJAN
M.S. Materials Science and Engineering, University of South Florida, 2015

A dissertation submitted in partial fulfillment of the requirements
for the degree of Doctor of Philosophy in Materials Science and Engineering
in the Department of Materials Science and Engineering
in the College of Engineering and Computer Science
at University of Central Florida
Orlando, Florida

Spring Term
2020

Major Professor: Sudipta Seal

ABSTRACT

Access to clean, and sustainable energy is one of the biggest challenges of our generation. With the rapid growth of renewable energy harvesters, developing electrochemical energy storage devices (EEDs) that respond well to them is of significant interest. Supercapacitors are a class of EEDs with exceptional power densities and ultra-long cycle life. These properties make them an attractive candidate as a replacement, or to be used in combination with batteries and other EEDs.

In this dissertation, nano cerium oxide (nano CeO_2) based materials are examined as an active material for supercapacitor applications. The first part of this work details how the morphology and selective crystal planes can lead to significantly improved charge storage; and how a combination of high surface area and exposure of high energy crystal planes ({110}, {100}) can lead up to 1.5 times higher charge storage capacity. The remainder of the thesis examines how nano CeO_2 can effectively be used as an additive to improve the electrochemical properties of other supercapacitor materials. The second part describes a method to drastically improve the poor cycle life of conductive polymer-based materials by the addition of nano CeO_2 and graphene through scalable spraydrying process. The ternary composite exhibits a high energy density (46.3 Wh Kg^{-1}) and stable cycle life (92% capacitance retention after 6000 cycles). The third part details how nano CeO_2 can be used as an active mechanical spacer for graphene aerogel based material. Here, nano CeO_2 not only contributes towards charge storage but also prevents the restacking of graphene layers. The hybrid aerogels exhibit a high specific capacitance of 503 F g^{-1} and minimal capacitance fade

after 10,000 cycles. This work highlights how engineering nanostructures beyond simple size reduction can lead to superior electrochemical properties and ultimately EEDs with improved safety, high power, and energy density.

Keywords: Supercapacitor, Electrochemical Energy Storage, Cerium Oxide, Polyaniline, Graphene, Aerogel, MD simulation.

This work is dedicated to my family.

ACKNOWLEDGMENTS

I thank my advisor Dr. Sudipta Seal for his constant support, motivation, and guidance throughout my Ph.D. I also like to thank my committee members Dr. Raj Vaidyanathan, Dr. Linan An, Dr. Swaminathan Rajaraman, Dr. Tenfi Jiang, and Dr. Alfons Schulte.

I thank my lab mates who made this research possible, especially: Dr. Nileshi Saraf, Craig J. Neal and Dr. Tamil Selvan Sakthivel for the stimulating discussions and constructive feedback. I also acknowledge my other lab members Dr. Ankur Gupta, Yifei Fu, Udit Kumar, Dr. Shashank Saraf, Dr. Swetha Barkam for their support on collaborative projects. I extend my kind thanks to Kowsik Sampath Kumar for immensely helping me with my initial supercapacitor testing experiments. Special thanks to UCF MSE administrative team – Pamela, Sandra, Angie, Jodi & Cheryl.

I like to acknowledge the UCF's Dean's dissertation completion scholarship, UCF SGA for multiple travel awards. NASA, Autoliv & Garmor Inc for funding support. ASM International for giving me an opportunity to serve as student board member. I also kindly thank TMS, SNO, NGA, ACerS for multiple travel grants and scholarships.

I thank my beloved wife Kavya Ganapathy for the all the love, encouragement, patience and support. I also kindly thank my friends, especially: Karthik Sathiyamoorthi and Mohamed Al Hasan for their support. Finally, I am immensely grateful to my parents (Rani & Jeyaranjan), who have constantly supported my pursuits.

TABLE OF CONTENTS

LIST OF FIGURES

LIST OF TABLES

LIST OF ABBREVIATIONS

CNP	CeO_2 nanoparticles
CNR	CeO_2 nanorods
CNC	CeO_2 nanocubes
PANI	Polyaniline
rGO	Reduced graphene oxide
SC	Specific capacitance of electrode
I	Current
μ	Scan rate
Δt	Discharge time
ΔV	Potential window
m	Mass of active material on electrode
C_s	Specific capacitance of device
E	Energy density
P	Power density

CHAPTER 1:INTRODUCTION

1.1 Need for Electrochemical Energy Storage Devices

Energy storage is one of the biggest challenges of our generation. Access to clean, abundant and efficient energy is a key socio-economic issue. This has been attributed to our dependence on fossil fuels for energy production, environmental and climatic concerns associated with fossil fuels and a growing population. As major population growth is expected in South Asia and Africa, the U.S. Energy Information Administration (EIA) projects the global energy consumption would double by 2050 (**Figure 1a**).[1] With the rapid demand for energy, EIA also projects renewables-hydropower, wind, and solar as the fastest-growing source of electricity generation. This could reasonably mitigate issues of sustainability in energy generation. Electrochemical energy storage devices (EEDs) could play an important role in the newly evolving energy landscape.

EEDs store energy in a chemical form, which can be reversibly converted to electrical form. Examples of EEDs include batteries, fuel cells, capacitors, and electrochemical capacitors (or supercapacitors). Batteries and supercapacitors are the two main candidates of EED. They pose various advantages such as mobility, high energy density, and low cost. The Ragone plot, which describes the specific energy vs specific power of different electrochemical energy storage devices is shown in **Figure 1.2**. Traditional capacitors have very high specific power and low specific energy. Batteries, on the other hand, exhibit high specific energy and low specific power.

Electrochemical capacitors act as a bridge between traditional capacitors and batteries. The difference in the specific energy and specific power of batteries and capacitors can be attributed to the fundamental mechanism of charge storage.

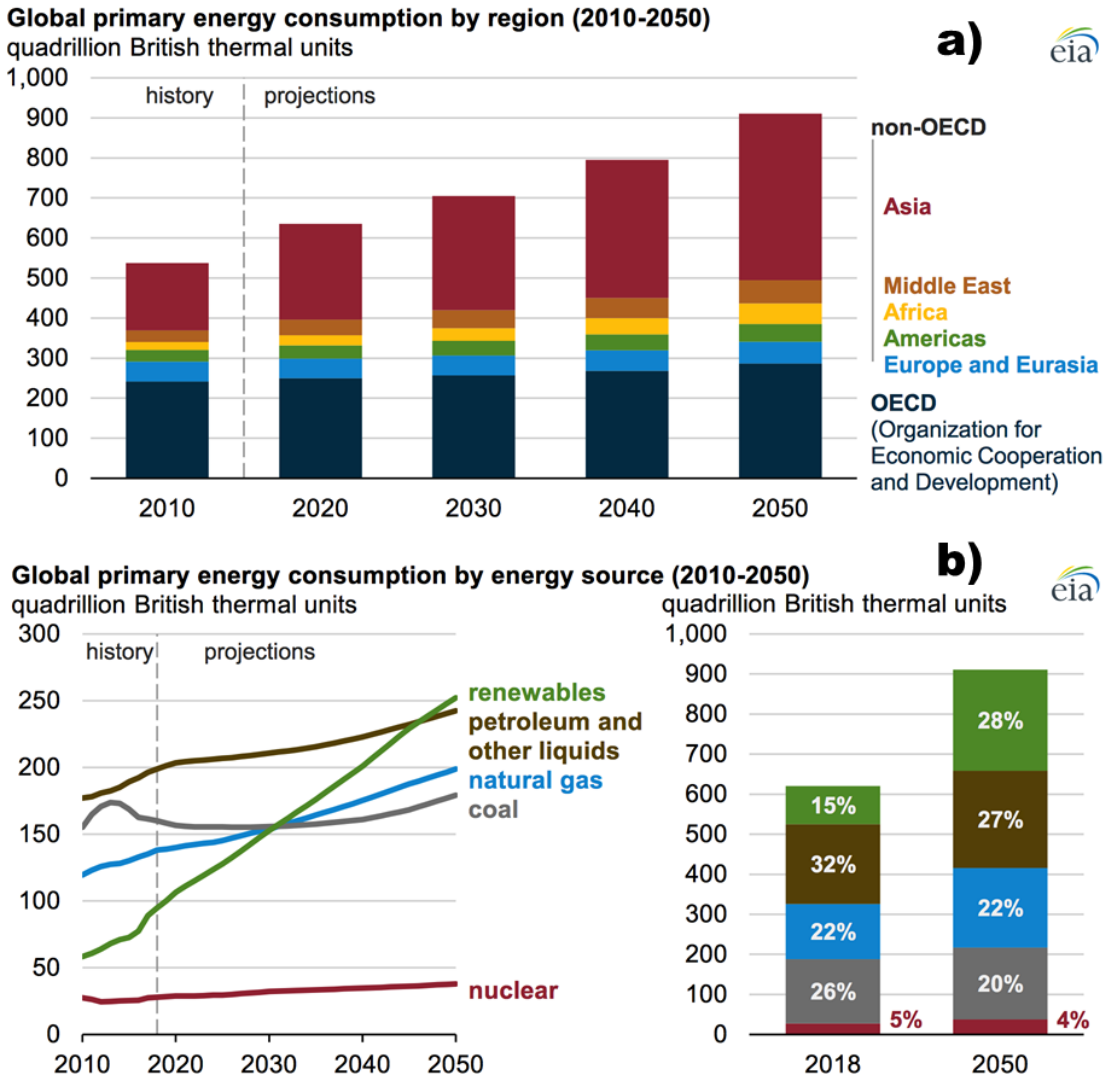

Figure 1.1: *a) The U.S. Energy Information Administration projects the global energy consumption would increase by ~50% by 2050. b) Renewables- hydro power, wind, and solar is the fastest growing source of electricity generation*. Reproduced from Ref.[1]

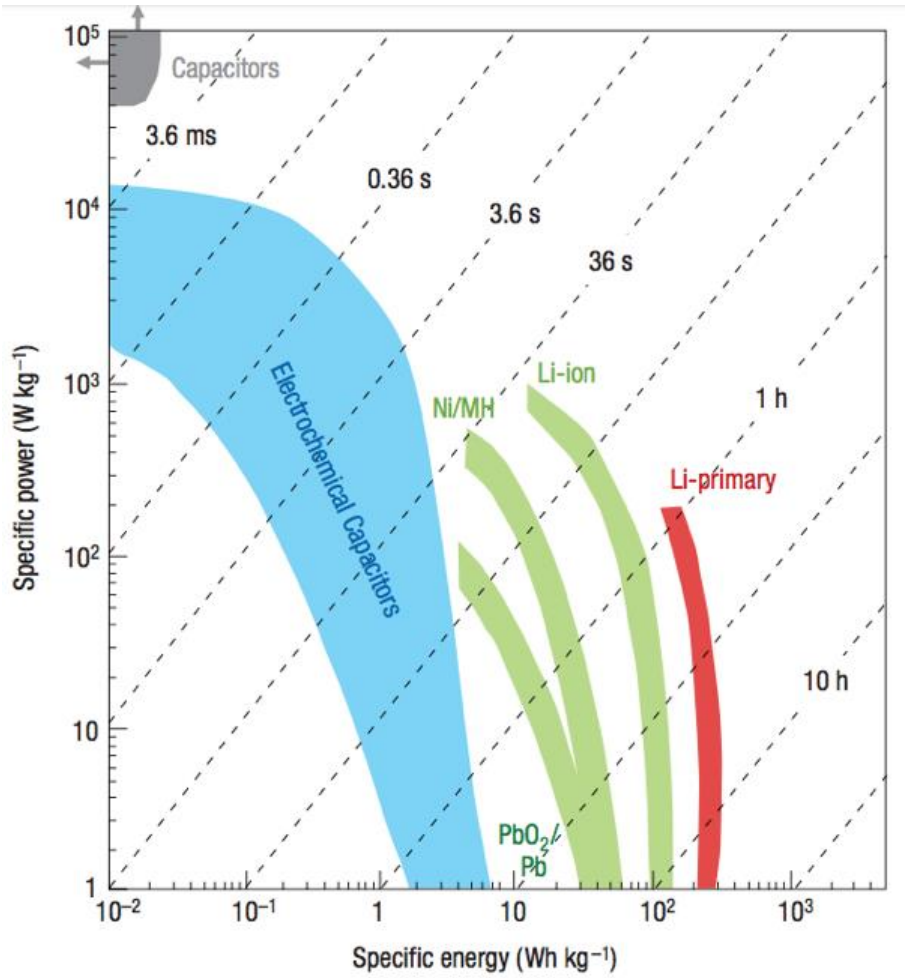

Figure 1.2: Ragone plots of different electrochemical energy storage devices. Electrochemical capacitors act as a bridge between traditional capacitors and batteries. Reproduced from Ref. [2]

Batteries exhibit bulk charge storage and thereby higher specific energy. Capacitors and electrochemical capacitors store primarily of the surface which gives them higher specific power. The Ragone plot also shows the typical response times of different EEDs. Generally, electrochemical capacitors store specific energy between 1-10 Wh Kg^{-1} in less than a minute and batteries store 10-200 Wh Kg^{-1} in hours.

Electrochemical capacitors and batteries should not be viewed as competing technologies but as complementary EEDs. [2, 3].

From a historical perspective, electrochemical capacitors were developed almost more than a century later than batteries. The first porous carbon based electrochemical capacitors were developed in the early 1960s by SOHIO. The concept of pseudocapacitance was first observed by Trassati et al for RuO_2 in 1971 for which the theoretical framework was developed by Conway and others. This thesis work deals with exploring nano cerium oxide (CeO_2) as an active material for supercapacitor applications.

1.2 Thermodynamics of Electrochemical Charge Storage

The Gibbs free energy stored in a capacitor operating at a potential *V* can be expressed as:

$$G = \frac{1}{2} Q dE = \frac{1}{2} C V^2 \tag{1.1}$$

where *Q* is the charge and d*E* is the potential difference. From **Equation 1.1**, it is can be observed that the voltage of the capacitor linearly varies (not constant) with the amount of charge, which can be expressed by the following reaction:

$$V = \frac{Q}{C} \; or \; \frac{dV}{dQ} = \frac{1}{C} \tag{1.2}$$

where *C* is the capacitance, which is a proportionality constant. The capacitance is dependent on the properties of the electrode and electrolyte materials and is expressed as:

$$C = \frac{A\varepsilon}{d} \tag{1.3}$$

where *A* is the surface area of the electrode material, ε is the permittivity of the electrolyte and *d* is the double-layer distance. However, the maximum Gibbs free energy in a battery can be expressed as:

$$G = QdE \tag{1.4}$$

which is twice the energy stored in a capacitor. The potential of the battery material is related to the chemical potential (ΔU) and the Gibbs free energy (ΔG) through the Nernst equation, which can be expressed as follows:

$$E° = \frac{-\Delta G}{nF} = \frac{-\Delta \mu}{nF} \tag{1.5}$$

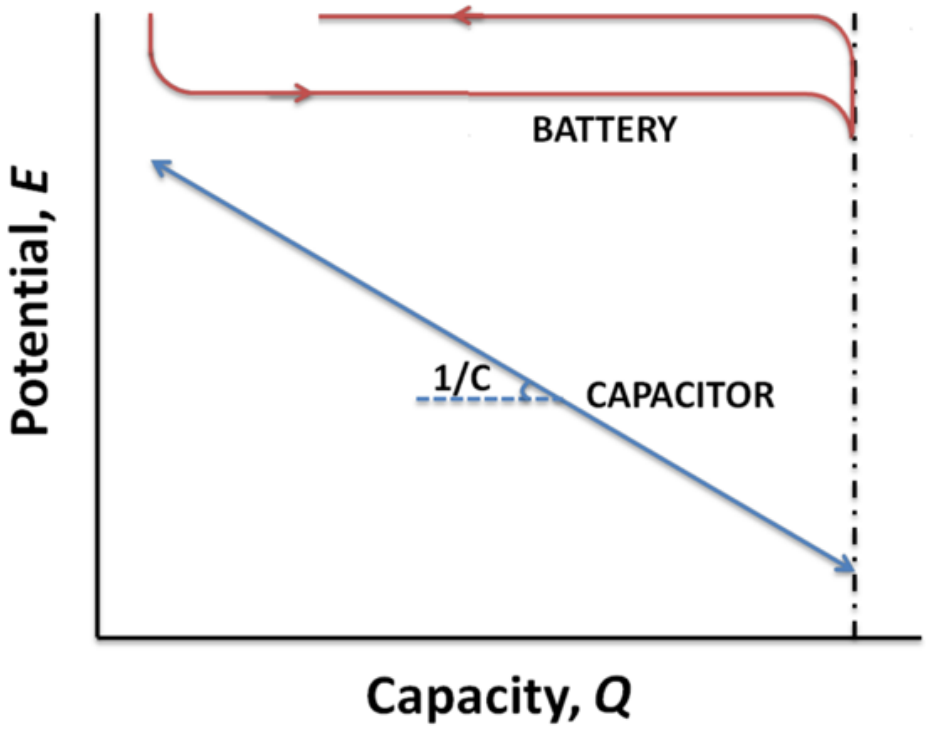

Figure 1.3: Potential vs charging curves showing the difference between an ideal electrochemical capacitor and battery. Adapted from Ref. [4]

The difference between electrochemical capacitors and batteries is clear from the potential vs charging curves shown in **Figure 1.3**. The potential of an ideal battery is constant during charge/discharge due the already existing thermodynamic potential irrespective of the charge being added. However, this is not the case with an electrochemical capacitor and the voltage of the capacitor is not constant and linearly varies with the amount of charge[4, 5].

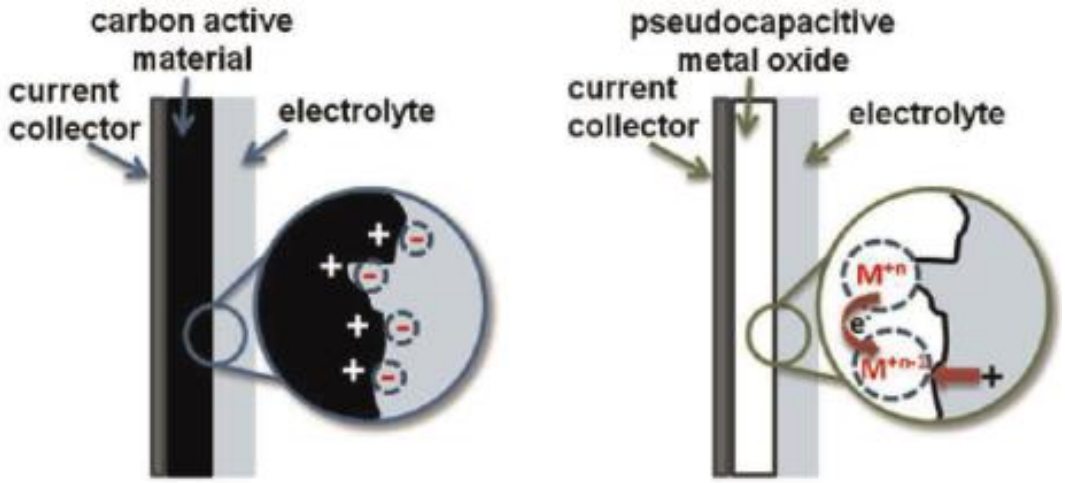

Figure 1.4: Different mechanisms of charge storage in the a) electric double-layer capacitors and b) pseudocapacitors. Reproduced from Ref. [6]

1.3 Types of Electrochemical Capacitors

Based on the mechanism of charge storage, electrochemical capacitors can be classified into two types: electric double-layer capacitors (ELDCs) and pseudocapacitors. As the name suggests, EDLCs stores charge through a thin double-layer at the electrode-electrolyte interface. The charge storage in EDLCs are purely electrostatic and a non-faradaic process, i.e. there is no electron transfer at the electrode-electrolyte interface. Pseudocapacitors stores charge through rapid redox

reactions, which is similar to the energy storage mechanism in batteries. However, the kinetics of the redox reactions is in a pseudocapacitor is much faster, as a result the response is capacitor like. The charge storage in pseudocapacitor is a Faradaic process i.e there is electron transfer as a result of redox reactions. **Figure1.4 (a-b)**. shows the different mechanisms of charge storage in the two types of electrochemical capacitors.

1.3.1 Electrical Double Layer Capacitors

The arrangement of the charges and dipoles at the metal-solution interface is termed the electrical double layer. The solution side of the double layer consists of several layers. A schematic description of the double layer, based on the Grahame model, is shown in **Figure 1.5**. The innermost layer, which is closest to the electrode is the inner Helmholtz layer. This consists of specifically adsorbed species and neutral molecules. The second layer is the outer Helmholtz layer, which primarily consists of solvated ions that are not specifically absorbed. The third layer is the Gouy-Chapman diffuse layer, which consists of solvated ions distributed randomly in a three-dimensional space due to the weak long-range electrostatic interactions and thermal agitations in the solution. The diffuse layer extends from the outer Helmholtz layer to the bulk of the solution. The charge storage in a double layer capacitor contains contributions from the Helmholtz and Gouy-Chapman layers, which can be assumed to be two capacitors arranged in series. The smaller of the two components is more important in determining the properties of the double layer.

The double-layer formed at each electrode of EDLC is analogous to a dielectric capacitor. However, a single electrode with a double-layer cannot be used to assemble

a practical device, it must be coupled with another electrode. Thus, the circuit diagram of an EDLC is composed of two capacitors C_1 and C_2 attached in series, which corresponds to the two electrodes. The total capacitance of the EDLC, C_{EDLC} can be estimated as:

$$\frac{1}{C_{EDLC}} = \frac{1}{C_1} + \frac{1}{C_2} \tag{1.6}$$

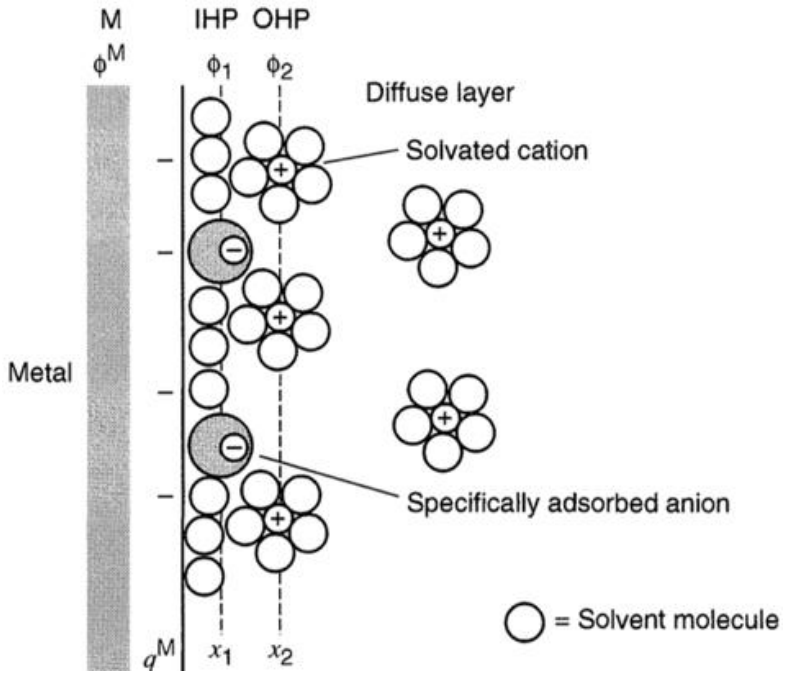

Figure 1.5: Schematic description of the double layer. IHP- Inner Helmholtz plane, OHP- Outer Helmholtz plane. Reproduced from Ref. [4]

1.3.2 Pseudocapacitors

Pseudocapacitance is another mechanism for capacitive type charge storage. This was first observed in 1971 in RuO_2. Here, the mechanism of charge storage is no more electrostatic. However, the response is very similar to EDLCs due to the fast kinetics. Several faradaic processes produce pseudocapacitance. Among them, the

three most important mechanisms are: (1) redox pseudocapacitance, (2) underpotential deposition, and (3) intercalation pseudocapacitance. The electrochemically adsorbed ions at the electrode-electrolyte interface is the basis of redox pseudocapacitance. Underpotential deposition happens when the ions form a monolayer on the electrode surface at a potential much lower than its redox potential. Common examples include the underpotential deposition of Pb and Cu on noble metals (Au, Pt). The faradaic charge transfer due to the intercalation of ions through the layered or tunneled structures in active material with no associated phase change gives raise to intercalation pseudocapacitance. The schematic representation of the three popular faradaic mechanisms for pseudocapacitance is shown in **Figure 1.6**.

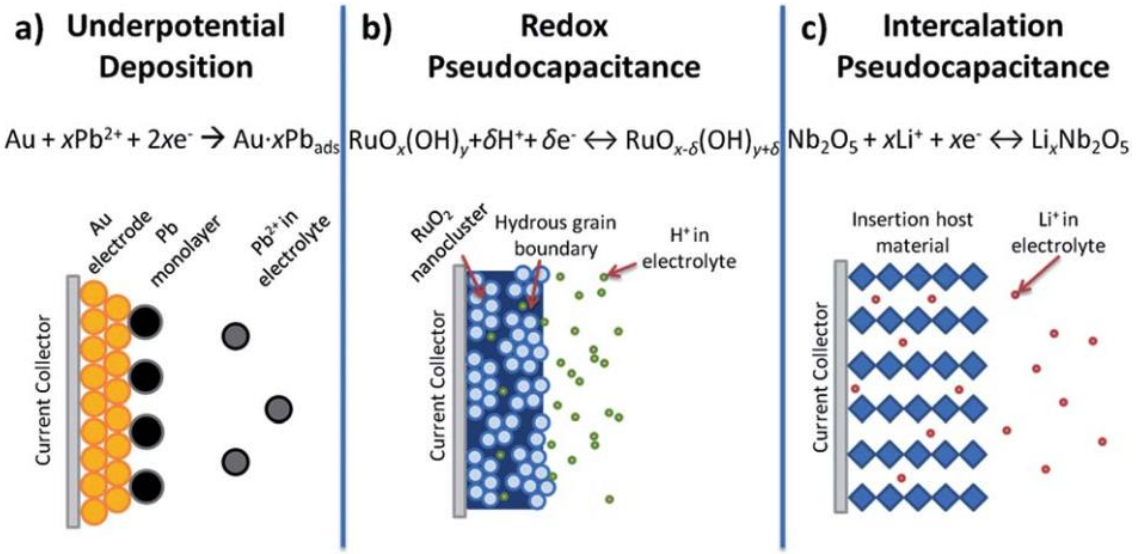

Figure 1.6: Various Faradaic mechanisms that produces pseudocapacitance: a) underpotential deposition, b) redox pseudocapacitance, and c) intercalation pseudocapacitance. Reproduced from Ref. [7]

1.4 Nanostructured Materials for Electrochemical Energy Storage

Nanomaterials are usually defined as materials with one of their dimensions in the nanoscale i.e 1-100 nm. Nanomaterials generally exhibit unique physiochemical properties compared to their bulk counterparts, which have been attributed to the high surface to volume ratio and quantum confinement effects. Since electrochemistry fundamentally involves electrode-electrolyte interfaces, the activity of nanomaterials is much higher due to higher available surface sites. Moreover, the potential of a redox reaction is related to the Gibbs free energy according to Equation 1.7. The high surface to volume ratios in nanomaterials adds a Gibbs-Thomson effect term to the Gibbs free energy:

$$\Delta_f G^{\circ}_{nano} = \Delta_f G^{\circ}_{bulk} + 2\sum \vartheta_j \frac{\gamma_j}{r_j} V_j \tag{1.7}$$

Where $\Delta_f G°_{nano}$, $\Delta_f G°_{bulk}$ are the Gibbs free energy of the nanomaterial and the bulk form, ϑ is the reaction coefficient, r is the radius, and γ is the surface tension. In nanomaterials, as the result of the Gibbs-Thomson effect is that the chemical potential at the surface is much higher than that of the bulk material.

1.5 Applications of Electrochemical Energy Storage

Though originally used to power complementary metal oxide semiconductor (CMOS) chips and volatile clock chips in computers, electrochemical capacitors are currently used in a wide range of applications. Early generations of capacitors were rated at few volts and exhibited a capacity only up to few farads. In ~40 years, electrochemical capacitors have come a long way from those early days. Modern

electrochemical capacitors have a working potential of up to 1000V and exhibit capacitance up to a few kF.

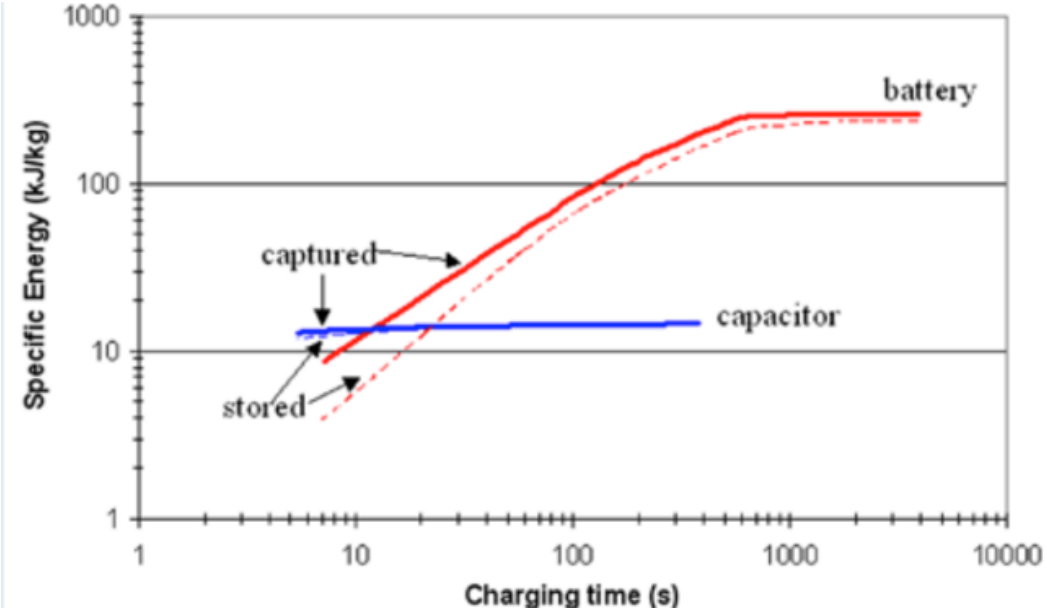

Figure 1.7: Performance of a typical 3000 F 2.7 V electrochemical capacitor and a 2.8 V Li-ion battery. Reproduced from Ref. [8]

Miller et al. compared the performance of a typical 3000 F 2.7 V electrochemical capacitor and a 2.8 V Li-ion battery (**Figure 1.7**). It is clear that for charging times greater than ~500 s, the specific energy of Li-ion battery can reach up to ~15 times than the capacitor. However, this difference is diminished for shorter time periods. For example, the specific energy of the battery is only ~5 times higher than the capacitor after 100 s. At a 10 s charge, the specific energy of both the devices is similar. However, the capacitor retains ~95 % of its charge whereas the battery retains only ~ 50% of the original charge. Thus, use of a battery with higher energy density could

result in a lighter EED. However, for applications that require rapid response times an electrochemical capacitor would be a better choice. Moreover, batteries would require a much bigger and sophisticated thermal management system. This study clearly disproves the common misconception that batteries are better EEDs.

Figure 1.8: ~ 50 MJ electrochemical capacitor based energy storage system in the Caterpillar 6120 H FS 1400-ton hybrid mining shovel. Reproduced from Ref.[9]

1.5.1 Application 1: Heavy Machinery

Electrochemical capacitors have been employed in cranes, rock crushers and mining equipment. In heavy machinery, it serves two purposes: (i) Store energy during swing decelerations and boom-down operations that would otherwise be dissipated and wasted as heat. (ii) Deploy the stored energy during peak power operations. Proper design of the capacitor package can significantly reduce the size of the primary power source such as an IC engine. Other advantages of using capacitors include reduced fuel emissions and fuel savings up to 25-30%. **Figure 1.7**. shows an image of the

Caterpillar 6120 H FS 1400-ton hybrid mining shovel fitted with ~ 50 MJ electrochemical capacitor-based energy storage system.

1.5.2 Application 2: Hybrid Electric Vehicles

Hybrid electric vehicles (HEV) are another application where electrochemical capacitors have been heavily used. There are different places in HEV where electrochemical capacitors are used. Pulse energy storage which provides an intermittent burst of energy at high power such as the ignition system is an example of the use of capacitors in HEV. Electrochemical capacitors are also used in the regenerative braking energy (RBE) storage system. The RBE in HEV is usually not as big as those in the heavy machinery but in the range of few kJ- MJ.

1.5.3 Application 3: Power Tools

The high power density, fast charge capability, and high cycle life make electrochemical capacitors a good fit for home power tools. Due to infrequent usage, home power tools such as screwdrivers are usually left in a state of partial to complete discharge. This requires charging the tool before any project. The approximate charge time of a high-rate battery Li-ion powered tool is generally 5-10 min. However, an electrochemical capacitor powered tool could be charged in a few seconds. Capacitor powered tools may require more frequent charging due to their lower specific energy. However, better charge retention, low operating times of the tool, and high cycle life can offset this drawback. **Figure 1.8**. shows a capacitor powdered Coleman screwdriver that is completely charged in 90 s.

Figure 1.9: Coleman screwdriver that be completely charged in 90 s. Reproduced from Ref. [8]

1.6 Economics of Supercapacitors in Regenerative Energy Storage

This section examines the cost of RBE associated with a typical hybrid city bus. Suppose a city bus weighs 15 tons and an has an average velocity of 35 mph. Then, the kinetic energy (K.E) is ~ 1.8 MJ or 0.51 kWh. Let's assume the average cost of energy is $0.15 /kWh. Then the cost associated with the K.E of the bus is $0.15 x 0.51 kWh = $0.08. Further assuming the bus makes ~1,000 stops per day and operates 300 days per year. Then, the maximum energy that can be recovered from the bus, annually, is $0.08 x 1000 x 300 =~$ 22,950.

Currently, Li-ion batteries cost much lesser than electrochemical capacitors. The approximate cost of commercial Li-ion batteries and electrochemical capacitors is ~ $1,000/ kWh and $20,000/ kWh. Thus, capturing the K.E of 0.51 kWh will cost ~$10,200 using capacitor technology and only ~$510 using Li-ion batteries. Though the cost

associated with Li-ion batteries appears much lower, there are other complications that add to the cost of Li-ion batteries. The cycle life and performance of battery packs are heavily dependent on various factors like operating temperature, depth of discharge and charge/discharge rate. Thus, battery packs often require oversizing, especially in this application where the charging time is very short. The nominal stopping time of the bus ~ 15 s. Moreover, oversizing up to 20 times is also required so that the battery pack does not experience more than 5% of its initial state of charge, which might lead to thermal runaway (electrochemical capacitors require no oversizing). This drives up the cost of the battery pack to a point where it is very similar to that of the capacitor system.

Although both EEDs have similar costs, various advantages of the electrochemical capacitor system such as very high cycle life, low maintenance, better charge retention and lower probability of thermal runaway make them an economically better option for RBE applications.

1.7 Supercapacitor Electrode Materials

1.7.1 EDLC Materials

Charge storage in carbonaceous materials is through an EDLC mechanism. The cyclic voltammograms (CV) of carbonaceous materials in aqueous and organic electrolytes are almost rectangular, which is similar to an ideal capacitor (**Figure 1.10**). Three essential properties of an EDLC type material required for maximum charge storage are: (i) High surface area, as EDLC charge storage is restricted to the surface. (ii) Good electrolyte accessibility through interconnected pores in carbonaceous materials. (iii) Excellent inter and intra-particle conductivity.

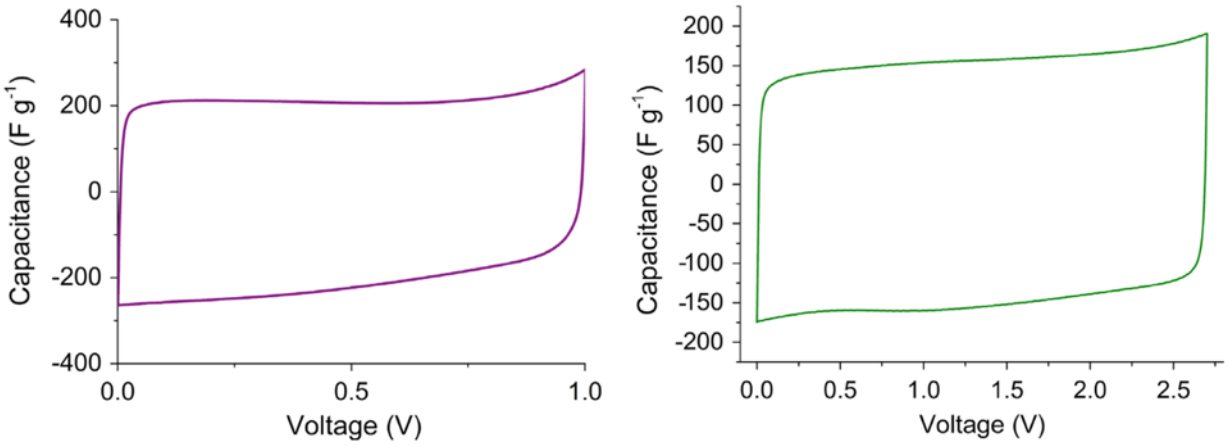

Figure 1.10: Rectangular cyclic voltammograms of carbon-based electrochemical capacitors in (a) aqueous 6M KOH and (b) non-aqueous 1M thertaethyl ammonium tetra fluoroborate electrolytes. Reproduced from Ref.[10]

Activated carbon (AC) is one of the most commonly employed electrode materials for electrochemical capacitors. AC is generally synthesized from a carbon rich source, which include a wide range of materials such as coconut shell, pitch, coke, and polymers. The synthesis involves a two-step process: carbonization and activation. Carbonization involves the thermal-chemical conversion of the carbon rich source to amorphous carbon. Activation is done to achieve a high surface area. Carbon materials can be either physically (H_2O, CO_2) activated or chemically (KOH, chlorides etc.) activated. The net result of the activation process is a carbon with high porosity and specific surface area (up to 3000 $m^2\ g^{-1}$ have been reported). Most of the commercially available electrochemical capacitors have AC based electrodes in an organic electrolyte that operates at a 2.7 V and has a specific capacity in the range of 100-150 Fg^{-1}.

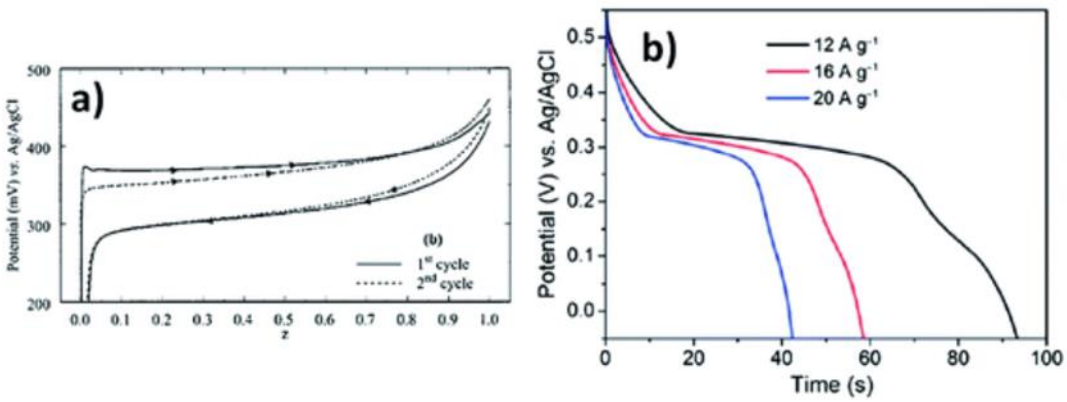

Figure 1.11: Comparison of the battery and pseudocapacitive type charge storage in Ni(OH)2. (a) Bulk $Ni(OH)_2$ displays flat battery type charge-discharge curves. Nanostructured $Ni(OH)_2$ contains both battery (flat) and captive type (sloping) regions in the discharge. Reproduced from Ref.[7]

1.7.2 Pseudocapacitive Materials

Materials that store charge through a pseudocapacitive mechanism are classified as pseudocapacitive materials. Pseudocapacitance can either be an intrinsic material property or extrinsically rendered through material engineering. Intrinsic pseudocapacitors are materials (such as MnO_2 and $RuO_2.nH_2O$) that exhibit capacitive type charge storage for a wide range of size and morphology. Extrinsic pseudocapacitor materials do not exhibit capacitive type charge storage in their bulk forms. This could be attributed to several reasons such as poor conductivity, phase transformation, and longer diffusion distance. However, by increasing the surface area to volume ratio through nanostructuring, these materials start exhibiting pseudocapacitive type charge storage. For example, bulk metal hydroxide such as $Ni(OH)_2$ exhibit battery type charge storage. However, nanostructured layered hydroxides pseudocapacitance behavior and

capacitance as high as 1750 F g^{-1} have been reported. **Figure 1.11** compares the charge-discharge profiles of a bulk and nanostructured $Ni(OH)_2$[7].

Conductive polymers are an extensive sub-class of pseudocapacitive materials that show high potential for supercapacitor application due to high conductivity, low cost, excellent chemical and thermal stability, fast kinetics and ease of synthesis[11-13]. However, the fundamental mechanism of charge storage in conductive polymers also severely restricts its cycle life. The repeated mechanical changes due to the doping/de-doping of the ions during the intercalation/de-intercalation process leads to severe structural degradation of the polymer. To overcome this drawback conductive polymers are combined with other capacitive materials to form binary and ternary composites.

1.8 Organization of the thesis

The primary goal of this work is to characterize nano CeO_2 for aqueous electrochemical capacitor applications. The present dissertation is organized in the following chapters.

In Chapter 1, the fundamental differences in charge storage in a battery and supercapacitor is discussed from a thermodynamically viewpoint. This followed by a discussion on different charge storage mechanisms and classifications of supercapacitor materials. The economics of supercapacitors vs batteries and a few practical applications of supercapacitors are also discussed. Finally, Nano CeO_2 is introduced as a potential supercapacitor material.

Chapter 2 focuses on the morphology and crystal plane dependent charge storage in nano CeO2. Here, the electrochemical properties of three CeO2

nanostructures are analyzed using cyclic voltammetry and galvanic charge-discharge to understand its pseudocapacitive behavior. Collaborative MD simulations were also performed to generate reactivity maps of the nanosctrutures. The goal of this study was to understand whether the charge storage behavior is dependent on nanostructure descriptors other than its surface area (such as morphology and exposed crystal planes.)

In Chapter 3 explores the idea of using nano CeO_2 as an additive to improve the electrochemical properties of other supercapacitor materials. Here, the best performing CeO2 nanostructure (nanorods) from the previous study is used in combination with graphene to effectively combat the poor cyclic performance of polyaniline (a conductive polymer). An industry scalable process to synthesize 3D hierarchical compound composed of polyaniline nanofibers, CeO_2 nanorods, and graphene sheets is proposed. Electrochemical investigations reveal that the charge storage and cyclic performance of the ternary compound is much better than the state-of-the-art conductive polymer-based compounds.

Chapter 4 describes a method to produce hybrid nano CeO_2- graphene aerogels using a bottom-up approach. Here, nano CeO_2 is explored as an active spacer to effectively suppress the restacking issue associated with grapheneous material. The hybrid aerogels exhibit superior electrochemical properties and ultra-long cycle life. The kinetics of charge storage and the surface vs the bulk contributions were also estimated.

CHAPTER 2: MORPHOLOGY AND CRYSTAL PLANES EFFECTS ON SUPERCAPACITANCE OF CERIA NANOSTRUCTURES

The work presented in this chapter has been published in

Particle & Particle Systems Characterization, 2018, 35(10), 1800176.

DOI: 10.1002/ppsc.201800176

2.1 Introduction

The Internet of Things (IoTs) is a network of thousands of smart sensors, actuators and other devices interconnected through a digital medium that can have dramatic impacts on our daily lives. IoTs can monitor a variety of systems like power grids, wind turbines and traffic surveillance.[14-16] The sensors connected to these networks can work independently and in tandem with other devices to collect monitoring data that can significantly improve the overall performance of systems. More importantly, monitoring various crucial parameters helps to predict the failure of systems, before they can actually happen.[17] The huge potential and remarkable applications of IoTs have led to their widespread usage. [18] With the proliferation of these sensors and actuators, comes the concern of their energy autonomy;[19-21] in an effort to develop green and sustainable systems, energy harvesters could be used to power them. However, the intermittent nature of renewable energy sources mandates the use of an appropriate EEDs alongside the harvesters.[22]

The nature of applications for these sensors requires EEDs with high power densities and long cycle life. Pseudocapacitors are a type of EED that stores charge by fast redox reactions. Due to the rapid surface and sub-surface redox reactions, pseudocapacitors exhibit higher energy densities than traditional electrolytic double layer capacitors (EDLCs), which work by the accumulation of electrolyte ions onto the surface of the active material. They also show power densities higher than conventional batteries. These advantages, combined with the very high cycle life (almost 10x that of conventional batteries), make pseudocapacitors an excellent fit to power the remote sensors and actuators, in the IoTs network. Besides being used as a standalone EED, they can also be used in combination with batteries and other EEDs.[3, 23]

Though RuO_2 is the gold standard for pseudocapacitor materials, the high toxicity and even higher cost has limited its large-scale commercialization.[5, 24] As a result, other redox active metal oxides that can potentially replace RuO_2 have predominantly been tested as pseudocapacitor material; these include: MnO_2, NiO, CoO_x, V_2O_5, etc. [2, 25-33] However, these metal oxides also suffer from various problems like dissolution, poor cycle life and high cost. Besides metal oxides, various materials like metal chalcogenides, MXenes, polymers and rare earth oxides are also being tested as alternate active material for pseudocapacitors.[34-37]

One such material- cerium oxide (CeO_2), a rare earth oxide, is gaining a lot of attention due to its surplus availability, very low toxicity, highly reversible oxidation states ($3^+/4^+$), no phase change at operational conditions and low cost.[38-46] Though nano CeO_2 is a relatively new supercapacitor material, its unique properties have found

extensive use in a wide range of other applications; like catalytic converters, oxygen storage, solid oxide fuel cells, and biosensors.

Although highly redox active, CeO_2 does not exhibit a 2D layered structure or have 1D tunnels in the structure, like traditional EED materials, which provide pathways for insertion/exertion of ions. As a result, bulk CeO_2 cannot be used to assemble a practical EED. However, this limitation can be successfully overcome by adopting a nanostructuring strategy. Nanostructuring CeO_2 boosts its surface area to volume ratio to a very large amount.[47, 48]

Like many other metal oxides, CeO_2, a ceramic material, suffers from an inherently low electrical conductivity. Thus, nano CeO_2 has been used as supercapacitor material, often in combination with carbonaceous materials like graphene, reduced graphene oxide (rGO), graphene oxide, nitrogen doped reduced graphene oxide and carbon nanotubes.[39, 40, 49-52] Supporting CeO_2 over these carbonaceous material improves the conductivity and thereby increases charge storage. Padmanathan et al. showed that CeO_2 nanoparticles and carbon coated CeO_2 nanorods synthesized by a simple hydrothermal process exhibits a specific capacitance of 381F g^{-1} and 400 F g^{-1} respectively.[53] Further, doping with metals has also shown to improve the capacitance. Ag and Pt doped CeO_2, in combination with rGO, have been shown to exhibit up to five times and ten times, respectively, higher specific capacitance over their undoped counterparts.[41] The specific capacitance can also be improved by increasing the specific surface area. A larger specific surface area exposes more redox active sites to the electrolyte, thereby yielding higher charge storage. Sandipan et al.

used this strategy and synthesized CeO_2 nanostructures using a metal organic framework (MOF) sacrificial template. The obtained nanostructure retained the open structure of the template and displayed a high surface area. These MOF derived CeO_2 nanostructures, when used with KOH electrolyte, exhibited charge storage close to its theoretical capacitance (560 F g^{-1}). In case of a $K_4Fe(CN)_6$ doped KOH electrolyte, the same material showed a higher specific capacitance of 1204 F g^{-1} at a current density of 0.2 A g^{-1}. [54]

The small form factor and remote location of sensors, in IoTs, dictate size restrictions on the EEDs. This has directly led to the advent of micron-sized supercapacitors which use nano-sized active material for charge storage.[55] Considering the minuscule amounts of active material used in these EEDs, it is crucial to optimize them for maximum charge storage. In light of this matter, nanostructures synthesized with highly reactive exposed crystal planes could be employed to maximize energy storage; as such nanostructures have shown enhanced performance in a variety of application.[56-58] Recently, it has been shown that CeO_2 nanostructures dominated by highly reactive crystal planes exhibited increased oxygen storage[59] and catalytic activity.[60 61] Thus, morphological control of CeO_2 nanostructures will also have an effect on electrochemical charge storage, as highly reactive planes will undergo higher redox activity. Nanostructures dominated by highly reactive planes can also display better rate capability due to the improved rate of redox reactions.

Recently, we reported the shape controlled synthesis of different CeO_2 nanostructures by a one-step hydrothermal synthesis method and also established a

morphological phase diagram for the same.[62] However, the relationship between the morphology of nanostructured CeO_2 and crystal plane effect on charge storage capacity has not yet been reported. In this regard, three different morphologies; namely, CeO_2 nano-particles (CNPs), CeO_2 nano-rods (CNRs) and CeO_2 nano-cubes (CNCs) were engineered to contain specifically exposed crystallographic planes. All of these nanostructures were synthesized through a one-step hydrothermal process by varying the reaction temperature and the concentration of the precursors. The effects of surface area and differentially exposed planes of the nanostructures on the supercapacitance have specifically been analyzed using different electrochemical techniques. Our experimental evidence is supported by molecular dynamics models and discussed within the relevant literature.

2.2 Experimental Section

2.2.1 Materials

Cerium nitrate hexahydrate ($Ce(NO_3)_3.6H_2O$), sodium hydroxide (NaOH) and potassium hydroxide (KOH) were all purchased from Aldrich Chemical Co. (Milwaukee, WI). All reagents were used without any additional purification.

2.2.2 Synthesis Procedure

The procedure to selectively synthesize different morphologies, CNPs, CNRs and CNCs, uses a template free hydrothermal process by varying the caustic condition, time and temperature of the reaction. The details of which can be found in Sakthivel et al.[62] Briefly, appropriate amounts of $Ce(NO_3)_3.6H_2O$ and NaOH were separately mixed to 20ml of deionized water (DI H_2O). The two solutions were then mixed together with

vigorous stirring. The thoroughly mixed solution was transferred to a Teflon lined stainless-steel autoclave to about 85% capacity. Finally, the sealed autoclave was placed in an electric oven and held at 80-160 °C for 6-24 h to yield different CeO_2 morphologies. After this hydrothermal process, the pale-yellow precipitates (CNP or CNR) or the white precipitates (CNC) were collected, washed several times and then dried at 70°C for 12h. The schematic of the synthesis process is depicted in **Figure 2.1a)**.

2.2.3 Electrochemical Measurements

The electrochemical measurements were performed in a three electrode configuration with 3M KOH aqueous electrolyte at room temperature. A Pt mesh and saturated Ag/AgCl (saturated NaCl) were used as the counter and reference electrode respectively. Nickel (Ni) foam was used as the current collector. Before fabricating the working electrode, the Ni foam was cleaned thoroughly by first ultra-sonicating in 1M HCl for 5 min, followed by ultra-sonication in ethanol for 15 min. The cleaned Ni foam was then dried and stored for future use. The working electrodes were fabricated by thoroughly mixing nano CeO_2 with carbon black and polytetrafluoroethylene (PTFE, Alfa) in an 85:10:5 mass ratio. A small volume of N-methyl-2pyrollideone (NMP, Alfa) was then added to this mixture to aid the formation of a homogeneous slurry. This slurry was applied on to a clean Ni foam and dried under vacuum overnight at 120°C. All working electrodes were 1 cm x 1 cm in dimension and contained approximately 2-3 mg of active material loaded. The electrochemical measurements were carried out with potentiostat (Bio-logic). CVs were measured over a voltage range of -0.1 V to 0.45 V at

sweep rates from 5 to 100 mV/s. GCDs were measured over the voltage range of -0.1 V to 0.45 V at specific currents from 1 to 32 A/g.

2.2.4 Instrument Characterization

The x-ray diffraction (XRD) patterns of the different CeO_2 nanostructures were acquired using a Rigaku D/MAX diffractometer with a Cu X-ray source from 15° to 80° at a scan speed of 2°/min. The shape and size of the nanostructures were analyzed using high-resolution transmission electron microscopy (HRTEM; Philips Tecnai 300kV). Surface area measurements were performed using the Brunauer–Emmett–Teller (BET) nitrogen adsorption method (*Quantachrome Nova-e* surface area analyzer). The specific surface areas of all three CeO_2 morphologies were obtained by N_2 absorption-desorption isotherms at 77 K. All surface area measurements were performed after degassing the nanostructures under vacuum at 120 °C for 8 h.

2.2.5 Computational Methods

Atom-level models of a ceria nanoparticle, nanorod and nanocube were generated using previously developed methods.[63, 64] Specifically, MD simulation using the DL_POLY code,[65, 66] was used to amorphise and then crystallize each nanostructure. Simulating crystallization enables microstructural features, such as exposed (reactive) surfaces and surface faceting, intrinsic point defects, grain-boundaries, and evolution of dislocations: all analogous to the real nanomaterial. The atoms were then colored according to their Madelung energies along a gradiented scale.[63]

2.3 Results and discussion

2.3.1 Structural Characterization of CeO_2 nanostructures

The XRD patterns of CNR, CNC, and CNP are shown in **Figure 2.1b**. All the peaks in the XRD spectra were effectively indexed as (111), (200), (220), (311), (222), (400), (331), and (420) plane reflections, of the pure cubic fluorite phase (JCPDS 34-0394, space group Fm3-m). CNPs and CNRs showed broader peaks, which is associated with smaller crystal size and higher lattice strain. The sharp peaks in CNCs suggested a larger crystal size and lower lattice strain. Crystallite size of all three nanostructures was calculated using the Scherrer formula ($D = k\lambda/B\cos\theta$), where D is the mean crystallite size, k is a crystallite dependent shape factor, λ is the X-ray wavelength, B is the full width at half maximum intensity and θ is the Bragg Angle. The calculated crystallite sizes of CNRs, CNCs, and CNPs were 39.77 nm, 52.14 nm, and 27.79 nm, respectively.

Figures 2.1 (c-h) show the TEM and HRTEM images of the as-obtained CNP, CNR, and CNC. The uniform CNPs from **Figure 2.1c** displayed size ranging from 15 to 20 nm. The clear lattice fringes from the HRTEM image in **Figure 2.1f** can be attributed to (111) and (200) planes, which have interplanar spacings of 0.31 nm and 0.28 nm, respectively. This indicated that the CNPs were octahedral in shape enclosed by {111} and truncated by {100} facets. The CNR in Fig 1 d) exhibited lengths spanning 150–200 nm and widths of 10–20 nm. **Figure 2.1g** depicts an HRTEM image of a CNR revealing three lattice fringes representing the (111), (220), and (200) planes, with interplanar spacings of 0.31 nm, 0.19 nm, and 0.28 nm, respectively. The CNRs were enclosed by

(111), (220), and (200) planes and showed a 1D growth along the [110] direction. **Figure 2.1e** shows a TEM image of as-prepared CNCs, which displayed size ranging 20–40 nm. The HRTEM image of CNCs in **Figure 2.1h** shows clear (200) lattice fringes with an interplanar spacing of 0.28 nm, which suggested CNCs exposed just the {100} surfaces.

It can be seen from **Figures 2.2 (a-c)** the atomistic models of the nanostructures generated by computer simulations is in accord with our experimentally synthesized nanostructures. The CNPs exhibited an octahedral structure enclosed by eight {111} and six {100} planes. CNRs showed growth in the [110] direction and were enclosed by the {100} and {110} planes, and CNCs were bound by six {100} planes. The {100} surfaces in CeO_2 were less stable compared to {111} and may facet into {111} surfaces. Close inspection of the CNRs and CNCs revealed considerable faceting of {100} surfaces into {111} together with steps and edges. In addition, the corners were not atomistically flat; rather they also faceted to {111}.

Brunauer-Emmett-Teller (BET) surface areas of the CNR, CNP and CNC were estimated to be 61.18 $m^2 g^{-1}$, 44.01 $m^2 g^{-1}$ and 38.27 $m^2 g^{-1}$ respectively. These surface area values are in good agreement with previously reported values in literature.[59] The surface area of CNR was ~50% greater than the other morphologies, whereas, CNC and CNP had comparable surface areas. Since charge storage in supercapacitors is predominantly a surface phenomenon, the large difference in surface area implies that CNR could yield better supercapacitor performance than CNC and CNP.

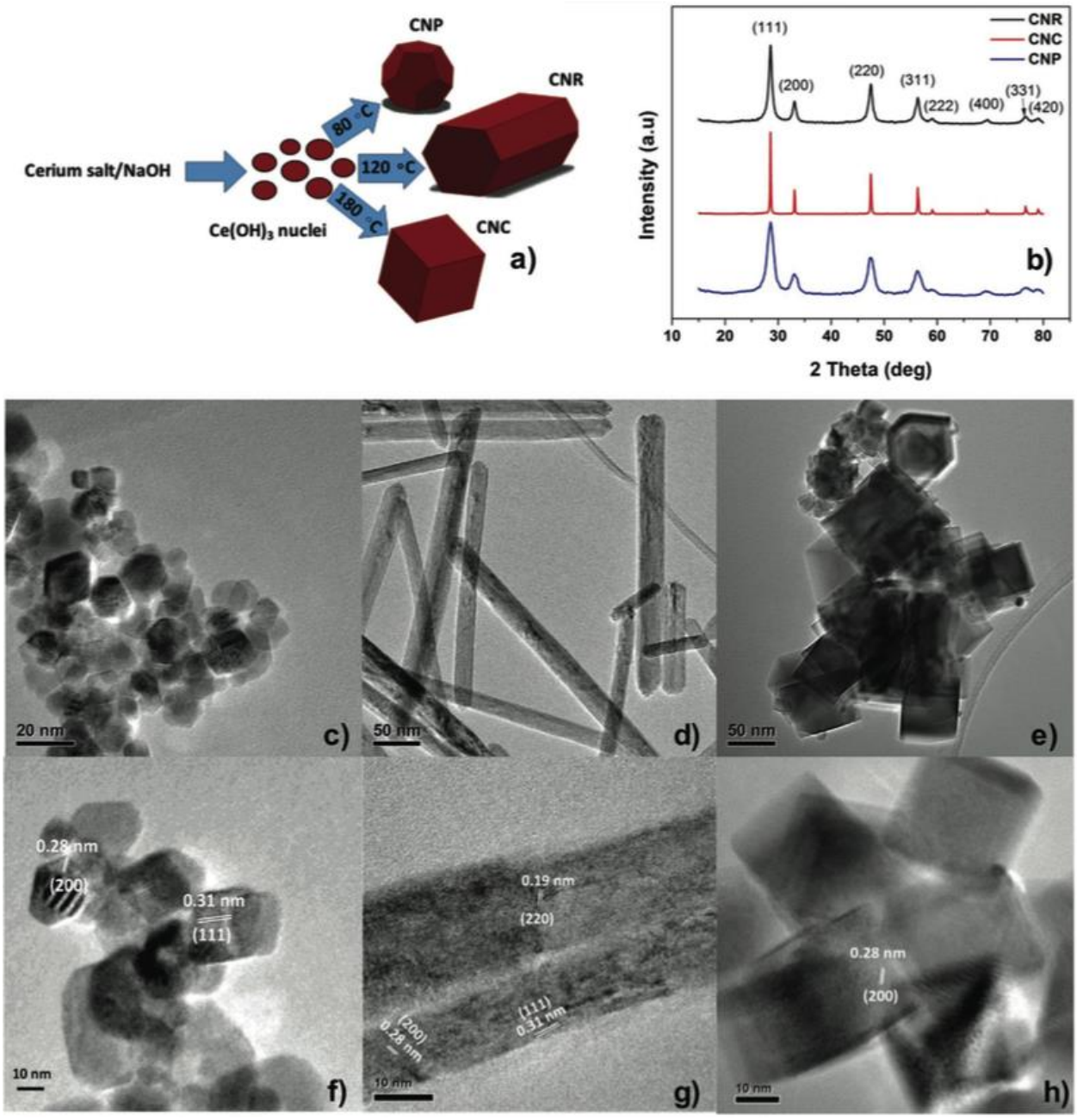

Figure 2.1: Synthesis and physical characterization of different CeO2 nanostructures. a) Synthesis schematics of CeO2 nanostructures through a one-step hydrothermal technique. b) XRD patterns of CNR, CNC and CNP. c)-e) TEM images and f)-h) HRTEM images of CNP, CNR, and CNC, respectively

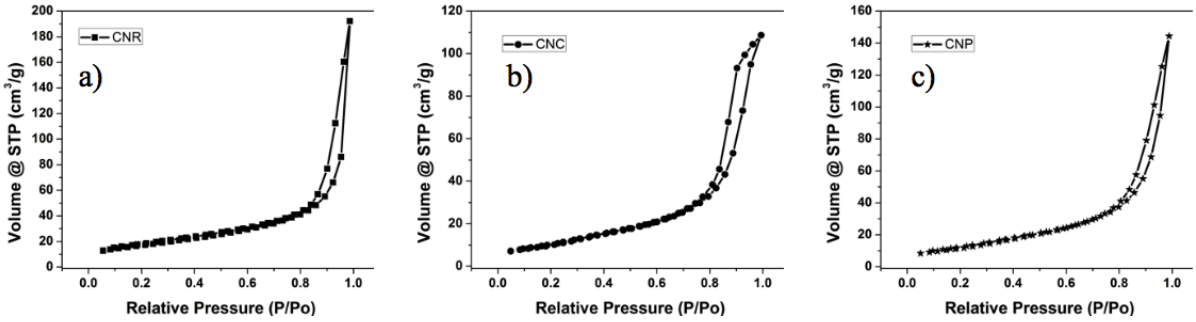

Figure 2.2: Adsorption and desorption isotherms measured at 77K for different CeO_2 nanostructures a) nano-rods b) nano-cubes and c) nano-particles.

2.4 Electrochemical properties of CeO_2 nanostructures

The supercapacitor performance of CNR, CNP and CNC were first analyzed by cyclic voltammetry (CV) in 3M KOH electrolyte between -0.1 V and 0.45 V at various scan rates from 5 to 100 mV s^{-1}. **Figures 2.3 (a-c)** show typical CV curves of CNR, CNP and CNC at different scan rates. A rectangular shaped CV is a characteristic feature of EDLC type charge storage.[67] It is clear from **Figure 2.3 (a-d)** that the CV curves of all three nanostructures clearly exhibit a non-rectangular shape, which suggests that the charge storage in CeO_2 nanostructures was predominantly pseudocapacitance.[53] The CV curves show a pair of redox peaks which correspond to oxidation and reduction of nano CeO_2 ($Ce^{4+} \leftrightarrow Ce^{3+}$). The redox process is the basis of charge storage and this mechanism can be expressed by the following faradaic reaction:

$$Ce^{IV}O_2 + K^+ + e^- \leftrightarrow Ce^{III}O.OK^+ \quad (2.1)$$

Besides the redox process, charge storage could be attributed to two other mechanisms when the electrode is immersed into the electrolyte: The first is the classical EDLC type charge storage. This is a non-faradaic mechanism that results from the accumulation of electrolyte ions onto the interface between the electrode surface

and the electrolyte. The second is another faradaic mechanism, which is due to the reversible electrochemical adsorption of the electrolyte cations onto the electrode surface. This can be expressed as follows:

$$(CeO_2)_{surf} + K^+ + e^- \leftrightarrow (CeO_2K^+)_{surf} \quad (2.2)$$

The latter two mechanisms of charge storage are restricted to the surface of the electrode. However, redox type charge storage (pseudocapacitance) is not restricted to the surfaces of the electrode material and can also occur in the sub-surface redox active sites.[38]

A linear increase in anodic and cathodic peak current with increase in scan rate (**Figure 2.4 (a-c)**) suggests fast kinetics of the redox reactions. Peak shifts were also observed in the CV curves of all three morphologies. This results from the high diffusion resistance at higher scan rates, which shifts the anodic peak current slightly to the positive side and the cathodic peak current slightly to the negative side. The redox peaks clearly visible even at a high scan rate of 100 mV s^{-1} signified fast redox reactions and high kinetic reversibility of the electrode. [68, 69]

For the same scan rate and normalized mass, it can be observed from **Figure 2.3d** that the area enclosed by the CV curve is highest for CNR, which is followed by CNC and CNP. This clearly suggested that the charge storage among the three morphologies followed the order CNR > CNC > CNP. From the CV curves, the specific capacitance (SC) of the electrodes can be calculated by the following equation:

$$SC = \frac{\int ivdv}{2\vartheta m\Delta V} \quad (2.3)$$

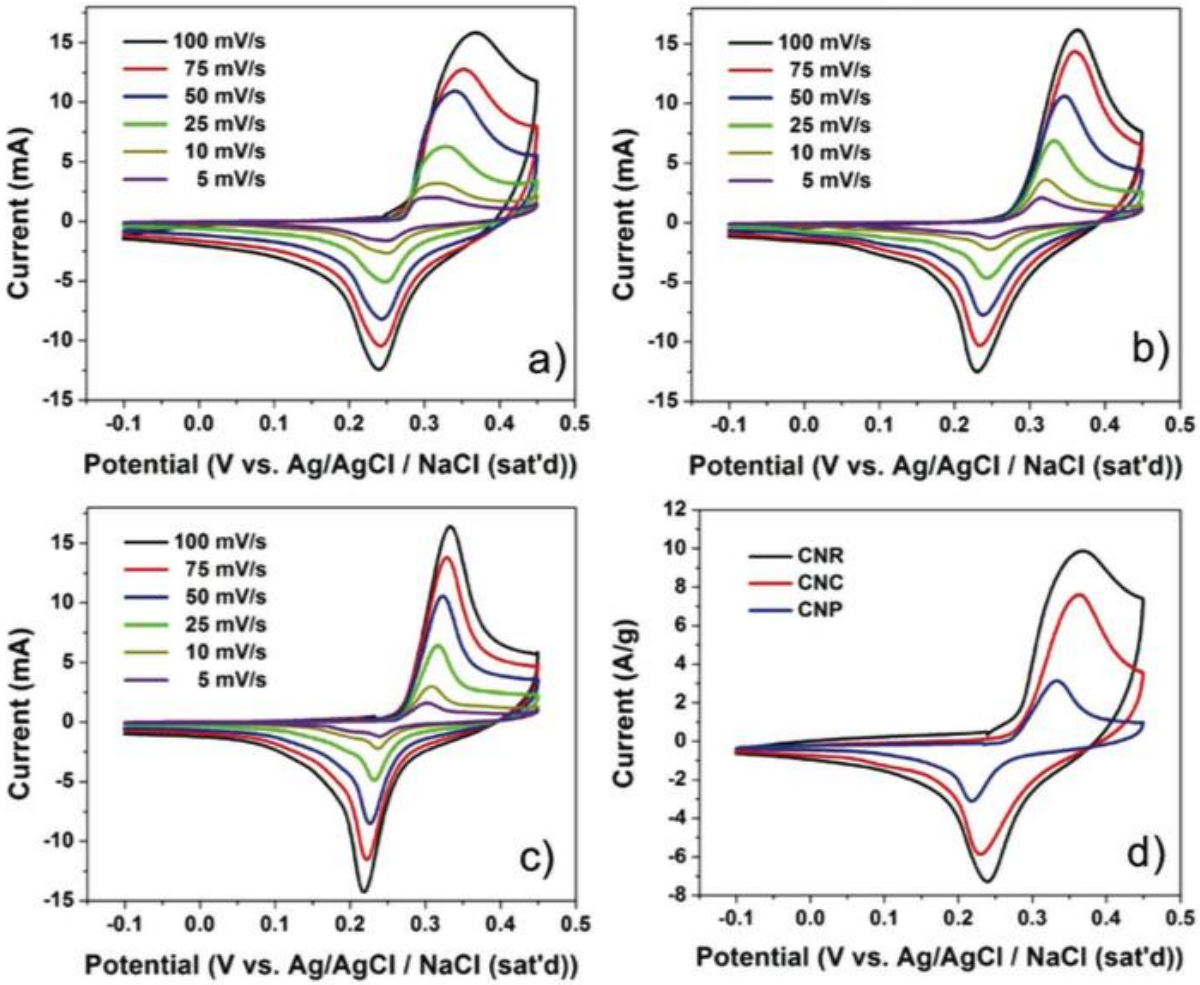

Figure 2.3: Electrochemical characterization of CeO2 nanostructures in 3M KOH. CV curves of a) CNRs, b) CNCs and c) CNPs at potential scan rates from 5 mV s-1 to 100 mV s-1. d) Comparison of the CV curves of the three morphologies at a scan rate of 100 mV s-1. *The SC shows a strong dependence on morphology and followed the order: SC of CNR > CNC > CNP.*

where *SC* is the specific capacitance (F g^{-1}), *v* is the potential (V), *i* is the response current (A) in the CV curve, μ is the scan rate (mV s^{-1}), *m* is the mass (*g*) of the active electrode material and ΔV is the potential range. The specific capacitances of CNR, CNC and CNP were 61.55 F g^{-1}, 45.30 F g^{-1} and 27.01 F g^{-1} respectively, at a scan rate

of 100 mV s^{-1} and 130.20 F g^{-1}, 119.22 F g^{-1} and 63.76 F g^{-1} respectively, for a scan rate of 5 mV s^{-1}.

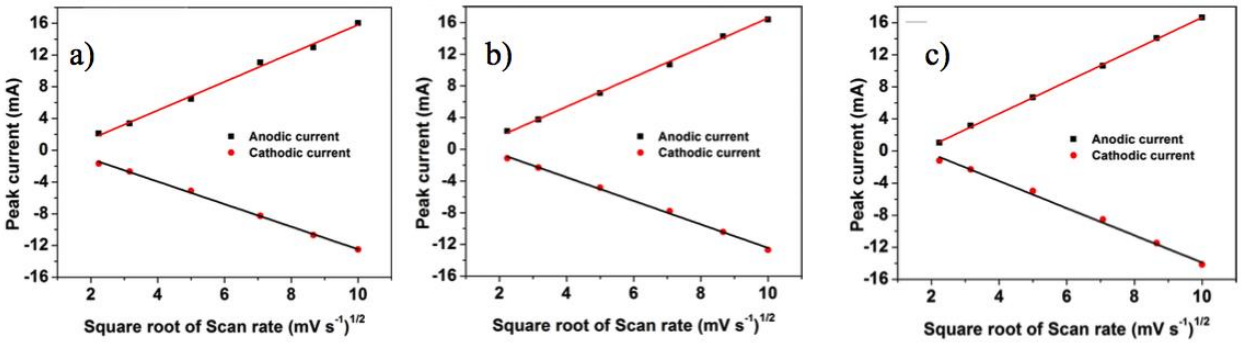

Figure 2.4: Cathodic and Anodic peak currents from CVs as a function of square root of scan rate a) nano-rods b) nano-cubes and c) nano-particles. A linear increase in anodic and cathodic peak current with increase in scan rate suggests fast kinetics of the redox reactions.

The specific capacitance decreases with increasing scan rate (**Figure 2.5d**). At lower scan rates, the electrolyte ions have ample time to diffuse into the electrode material. This allows for charge storage not only at the surface available redox active sites but also at the interior redox active sites in the bulk of the material, which can be attributed to the high specific capacitance.[70, 71] However, this was not the case at higher scan rates, where the diffusion of the electrolyte K^+ ions becomes limited. The limited diffusion results in underutilization of the available redox active sites in the electro-active material, which directly translates into lower specific capacitance as charge storage is mostly limited to the surface of the electrode material.[72]

To further understand the supercapacitor properties of the three CeO_2 morphologies, galvanostatic charge- discharge (GCD) measurements were carried out in a potential range between -0.1 V and 0.45 V. **Figures 2.5 (a-c)** show typical GCD curves of CNR, CNP and CNC at different current densities from 1 A g^{-1} to 32 A g^{-1}. It can be seen that the discharge portion of the curve first shows an iR drop, which is due to the internal resistance of active electrode material. This is followed by a small region where the potential linearly varies with time, which is due to the EDLC type charge storage. The third is a predominant non-linear region, which is associated with pseudocapacitive charge storage.[73-75] The specific capacitance, SC of all electrodes can be estimated from the GCD curves using equation (4).

$$SC = \frac{I\Delta t}{m\Delta V} \tag{2.4}$$

where *I* is the current (A), Δt is the discharge time (s), ΔV is the potential window (V) and *m* is the mass (g) of the active electrode material. The specific capacitances of CNR, CNC and CNP were 162.47 F g^{-1}, 149.03 F g^{-1}, and 97.72 F g^{-1} at 1 A g^{-1}, and, 58.59 F g^{-1}, 50.23 F g^{-1}, and 20.52 F g^{-1} at 32 A g^{-1}. The pattern of results obtained from GCD is in clear agreement with the results from the CV curves.

The specific capacitance decreases monotonically with an increase in current density (**Figure 2.5e**). It can be observed from **Figures 2.5d** and **e**, the SC of CNRs was consistently much higher than other nanostructures. The highest SC in CNRs can be attributed to two factors: high surface area and exposure of highly redox active crystal planes. As stated previously, the specific surface area of CNRs was almost 50% higher than CNCs and CNPs. This high surface area implied a higher number of redox

active sites were exposed to the electrolyte. This can explain the better performance of CNRs, as charge storage in supercapacitors is primarily a surface phenomenon. Furthermore, the exposure of highly reactive {110} and {100} surfaces also accounted for the high SC.

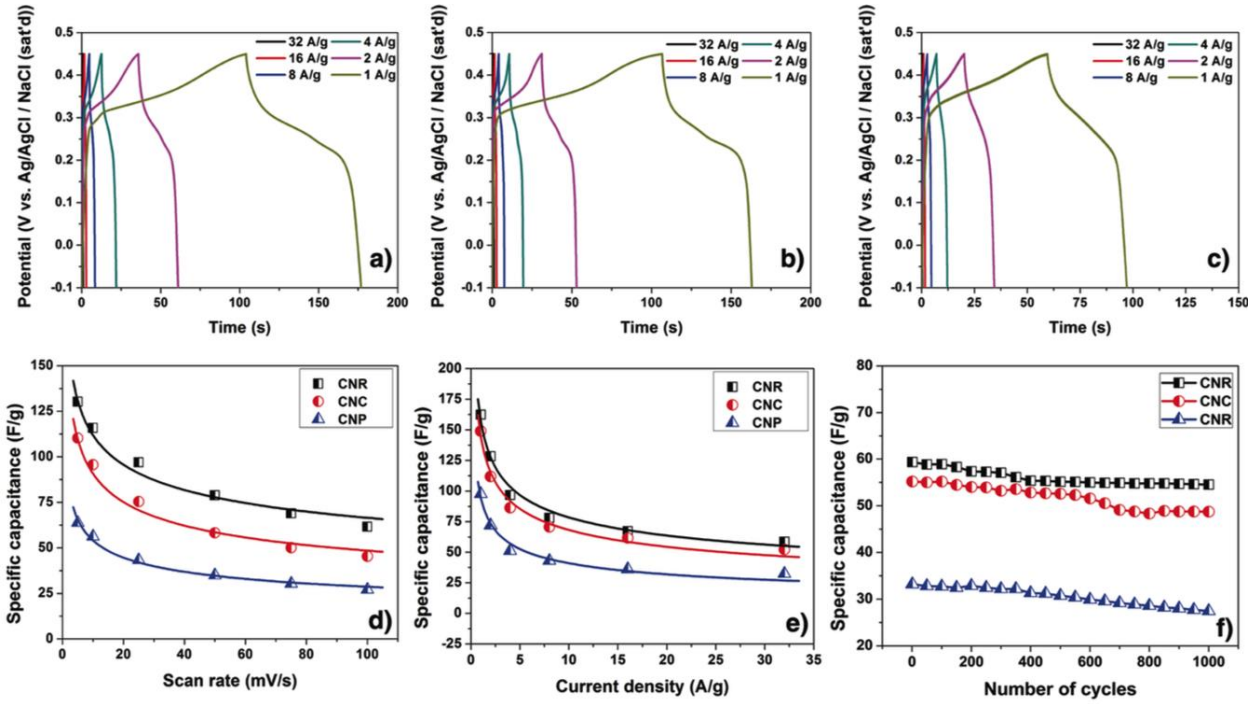

Figure 2.5: Supercapacitor performance of CeO2 nanostructures. Galvanostatic charge discharge curves of a) CNRs, b) CNCs and c) CNPs, at current densities from 1 A g-1 to 32 A g-1. Specific capacitance of CeO2 nanostructures as a function of d) scan rate and e) current density. f) Cyclic performance of CeO_2 nanostructures at 10 A g^{-1}. The higher SC of CNRs can be attributes to the large difference in surface area and high exposure of the more redox active {100} and {100} surfaces. Though CeO_2 nano-cubes and CeO_2 nano-particles have comparable specific surface areas, the high exposure of more active {100} facets in CeO_2 nano-cubes facilitate them with higher SC.

Although high surface area is crucial for charge storage, at comparable surface areas, it is inferred that exposed crystal planes has a more profound effect on charge storage. For instance, it can be observed from **Figures 2.5 d** and **e**, despite a slightly lower surface area, CNCs exhibit higher charge storage than CNPs. The higher surface area of CNPs may facilitate it with higher EDLC type charge storage, as this type of charge storage is directly proportional to the surface area accessible to the electrolyte. [76] However, the primary mechanism of charge storage in nano CeO_2 is pseudocapacitance.[38, 53] Thus, CNCs, with a large exposure of high energy crystal planes that favor redox reactions, exhibited higher SC than CNPs. From **Figure 2.5 e** it can be seen that CNRs and CNCs consistently exhibit better rate capability than CNPs. For example, at a high current density of 8 Ag^{-1}, the SC of CNRs and CNCs reduced to 78.15 F g^{-1} and 70.74 F g^{-1}, respectively, but the SC of CNPs reduced to 38.22 F g^{-1}. This indicates that the exposure of highly reactive surfaces - {110} and {100} in CNRs and {100} in CNCs equip these nanostructures with better rate performance than the low energy {111} dominated CNPs. **Table 2.1** lists the particle size, specific surface area, exposed planes and specific capacitance of all three morphologies.

Thus, our results in contrast to EDLC type material, clearly indicate that even with a high surface area, crystalline pseudocapacitive materials can yield low SC values in the absence of highly redox-active exposed crystal planes. This is in good agreement with previous reports that state surface area has a limited effect on charge storage in pseudocapacitive materials. [26, 70, 77]

Table 2.1: Summary of the characterization performed on three different nano CeO_2 nanostructures.

	CeO_2 nano-rods	CeO_2 nano-cubes	CeO_2 nano-particle
TEM particle size (nm)	**W 10-20 L 100-200**	**20-40**	**15-20**
Specific surface area (m^2/g)	**61.18**	**38.27**	**44.01**
Exposed planes	**{100} + {110} + {111}**	**{100}**	**{111} + {100}**
Specific capacitance @1A/g (F/g)	**162.47**	**149.03**	**87.73**

The longtime cyclic performance of CNRs, CNPs, and CNCs were also evaluated. **Figure 2.5 f** shows the cyclic performance of the electrodes cycled for 1000 cycles in GCD at 10 A g^{-1}. All morphologies showed excellent cyclic stability with only a slight decrease in SC after 1000 continuous cycles. CNRs and CNCs showed about 90.1% and 88.3% capacitance retention. CNPs exhibited slightly lower capacitance retention at 86.4%. The slight decrease in SC can be attributed to a number of factors. During the charge-discharge process, the active materials were exposed to repeated mechanical expansion/contraction due to the insertion/exertion of the electrolyte ions. This process could lead to the detachment of the loosely bound active material. Also, the repeated mechanical strain could force the aggregation of some nanostructures. Aggregated nanostructures would expose a lower number of redox active sites and increased internal resistance, which contribute towards the capacitance fade.[41, 53]

2.5 MD simulated Reactivity Maps of CeO_2 nanostructures

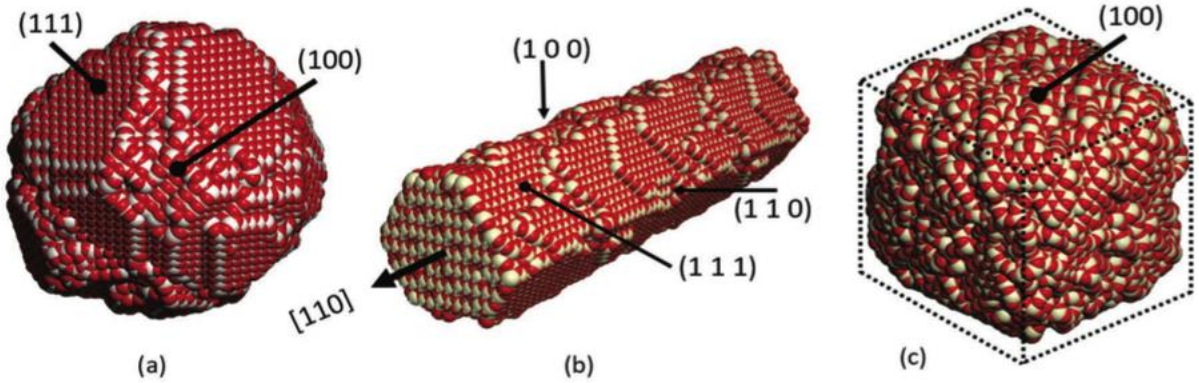

Figure 2.6: Atomistic models of CeO2 nanostructures generated by MD simulations. Ce atoms colored white and oxygen colored red. MD simulation revealed a) CNP exhibits an octahedral morphology with {111} truncated by {100} surfaces. b) CNRs are enclosed by {100} and {110} surfaces and show a unidirectional growth in the [110] direction. c) CNCs exposed six {100} surfaces. The MD simulations are in good agreement with TEM images.

Molecular dynamics simulations were used to further understand the effect of different exposed crystal planes on the supercapacitance of CeO_2 nanostructures. As stated previously, pseudocapacitance is linked to the ability of nano CeO_2 to be reduced. The conversion of Ce^{4+} to Ce^{3+} leads to the formation of oxygen vacancies. As a result, crystal planes with easily removable oxygen ions are more redox active and will offer higher redox type charge storage compared to crystal planes with strongly bound oxygen ions. Thus, it can be inferred that the amount of redox type charge storage of the crystal planes can be predicted by calculating their respective oxygen vacancy formation energies. Previous research based on Density Functional Theory (DTF)

calculations have demonstrated that different surfaces possess different enthalpies of reduction. It is easier to remove oxygen from the {110} surface compared to {100} and {111} surfaces. The most stable {111} surface has the highest reduction enthalpy as expected. However, the lowest is associated with the {110} surface rather than the least stable {100} surface, which is due to a higher oxygen concentration at the {110} surfaces compared to the {100} surfaces. [78]

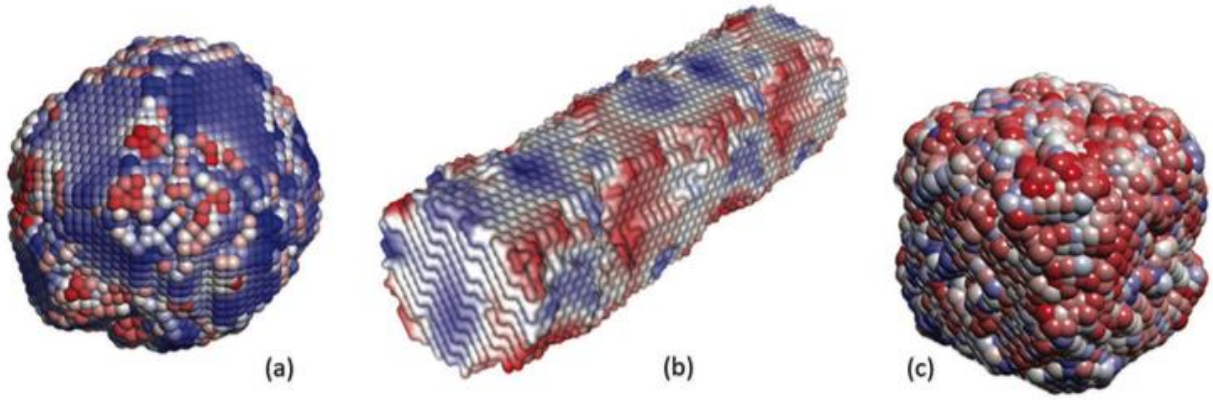

Figure 2.7: Reactivity maps of nanostructures predicted through Madelung energy. a) CNPs, b) CNCs and c) CNPs. Atoms colored according to calculated Madelung energy – red-white-blue gradient scale indicates low to high Madelung energy. The image shows that atoms on the {100} surfaces have predominantly low Madelung energies, which indicates they more easily reduced compared to ions on the {111} surface. It can be observed corners and edges are more reactive than the plateau {111} surface.

While DFT has been used to calculate the reduction energies on low index CeO_2 surfaces, the computational cost is high and therefore only perfect surfaces can be considered. Conversely, for nanoparticles and nanorods, there is considerable structural

perturbation and ionic relaxation emanating from: surface steps, edges corners, point and extended defects, such as dislocations and grain boundaries. Clearly, the reduction energy at a corner site would be very different from the perfect planer surface and each atom site would likely be associated with a different reduction energy. Accordingly, to determine the reduction energy associated with a ceria nanomaterial, a model of the whole nanomaterial is required. A ceria nanomaterial 10 nm in diameter typically comprises about 30,000 atoms, which is computationally prohibitive to consider quantum mechanically. Accordingly, classical mechanics is required to capture the effect of nanostructuring on the reducibility.

Previously, we showed that the Madelung energy of surface oxygen species is correlated with the energy required to extract it (oxygen vacancy formation energy). [79] Accordingly, the Madelung energy provides a rapid and computationally inexpensive measure of reducibility, and hence pseudocapacitance, for different nanostructures. [80] **Figures 2.7 (a-c)** show images of the model nanoparticle, nanorod, and nanocube, colored according to their Madelung energy. [81, 82] Visual inspection of the models reveals regions on the surfaces of the CeO_2 nanomaterials that can (energetically) be easily reduced (colored red) and regions that are relatively more difficult to reduce (colored blue). It is also evident that CNRs and CNCs have more surface sites that are redox active compared to the CNPs, which may help explain their higher specific capacitance.

In general, the simulations reveal that oxygen ions on {100} surfaces are energetically easier to remove as compared to the oxygen on {111} surfaces for both

the CNPs and CNRs. [83] [78] This suggests that high energy {100} surfaces are more redox active than low energy {111} surfaces. [84] It can also be observed that the corners, edges and rifts are more active than plateau {111} surfaces. We note that the CNRs and CNCs had higher proportions of {100} compared to {111} surfaces; all six of the CNCs surfaces were {100}. At comparable surface areas, the higher exposure of the more reactive planes equips CNCs with better energy storage than CNPs. Though CNCs and CNRs expose a large number of redox active crystal planes, the significantly higher surface area equips CNRs with the highest charge storage among the three nanostructures. Thus, from an energy perspective, our experimental results (SC of CNR > CNC > CNP) is supported by the simulation data that showed CeO_2 nanostructures with a higher number of {110} and {100} planes are more redox active than their {111} dominated counterparts.

We note that the reduction energies of individual Ce atoms can be very different – even on the same surface. For example, if one inspects **Figure 2.7 b**, one can see that {111} surface regions are both blue and red; some sites are easy to reduce (red), while others are energetically more difficult (blue). This can be attributed to the structural complexity including: steps, edges, corners and ionic relaxation at curved surfaces. Such insight is currently not possible using quantum mechanical methods and therefore classical mechanics can provide unique insight. Moreover, stating that a particular (perfect) surface is reducible is overly simplistic and could even be incorrect because of the structural complexity of a nanomaterial. This argument also helps

explain why a nanomaterial is catalytically more active than the parent (bulk) material that exposes reactive {100} surfaces.

The merit of this work lies in understanding the fundamental effect of exposed crystal planes on charge storage in CeO_2 nanostructures. From electrochemical and M.D studies it is clear that exposed crystal planes play a crucial role in charge storage. It can be observed that even with a low surface area, the exposure of highly reactive crystal planes in the nanostructures leads to increased charge storage. And a combination of high surface area and exposure of highly reactive planes is needed for maximum charge storage. To the best of our knowledge, we show here for the first time, supercapacitance as evidenced by the calculated reducibility, using full atom-level models. These cost-effective MD simulations could potentially be employed to improve the charge storage performance of other crystalline material systems beyond cerium oxide.

We are cautious not to suggest that a direct correlation exists between pseudocapacitance and the relative areas of redox active surfaces because the situation is more complex. In particular, during our MD simulations, we observe some faceting of CeO_2 {100} and {110} surfaces into {111} surfaces, which is thermodynamically driven to reduce the surface energy of the nanomaterial. Nevertheless, some CeO_2 {100} and {110} surfaces remain and the nanomaterial still has to navigate the high curvature and therefore redox active sites, such as atoms on steps, edges, and corners - are still exposed.

2.6 Conclusion

In summary, we report the influence of morphology on the supercapacitance of CeO_2 nanostructures using electrochemical techniques and molecular dynamics derived reactivity maps. Three different morphologies were synthesized by a one-step hydrothermal process. Electrochemical studies showed the supercapacitance of nanostructured CeO_2 followed the order: nano-rods > nano-cubes > nano-particles. Our findings indicate the difference in supercapacitance among the nanostructures is heavily influenced by two factors. The first is the specific surface area. A high specific surface area exposes a large number of redox active spots that facilitate pseudocapacitance type charge storage. This is clearly observed in the case of CeO_2 nano-rods, which has ~50% more surface area than the other two morphologies. The substantially high surface area facilitates CeO_2 nano-rods with the highest supercapacitance. The second is the type of the crystal plane exposed by a specific morphology. At comparable surface areas, morphologies that expose high-energy crystal planes, which are easily reduced and oxidized, exhibit higher charge storage. This was clearly observed in the case of CeO_2 nano-cubes that exhibited higher supercapacitance than CeO_2 nano-particles due to the higher exposure of the more reactive {100} planes, despite a slightly lower specific surface area. Selecting CeO_2 nano-rods over CeO_2 nano-particles could lead up to a two-fold increase in the charge storage capacity. Thus, this work provides a promise in designing supercapacitors with improved charge storage through a nanostructure morphology selection strategy.

CHAPTER 3:SCALABLE TERNARY HIERARCHICAL MICROSPHERES COMPOSED OF PANI/ RGO/ CEO_2 FOR HIGH PERFORMANCE SUPERCAPACITOR APPLICATIONS

The work presented in this chapter has been published in

Carbon 117 151 (2019) 192e202; DOI: 10.1016/j.carbon.2019.05.043

Reproduced by permission of Elsevier

3.1 Introduction

With the proliferation of electric vehicles, natural energy harvesters, kinetic energy recovery systems, and regenerative braking, developing electrochemical energy storage devices (EEDs) that respond well to them is a subject matter of significant interest. [23, 85] Supercapacitors, a class of EEDs, with their exceptional power densities and long cycle life makes them an attractive candidate as a replacement, or to be used in combination with battery packs, fuel cells and/or other EEDs [3, 4, 8, 9, 86] The active materials in supercapacitors fall into three broad categories: carbonaceous materials, [87-90] conductive polymers, [11, 12] and metal oxides. [7, 29, 91] Charge storage in carbonaceous materials is purely electrostatic (EDLC), while conductive polymers [5, 92] and metal oxides also stores charge through rapid redox reactions (pseudocapacitance) apart from the EDLC mechanism. [7, 29]

Polyaniline (PANI) is an extensively researched conductive polymer for supercapacitor application due to low cost, excellent chemical and thermal stability, fast kinetics and ease of synthesis. [11-13] However, the fundamental mechanism of charge

storage in PANI also severely restricts its cycle life. The repeated mechanical changes due to the doping/de-doping of the ions during the intercalation/de-intercalation process leads to severe structural degradation of the polymer. [11, 93] To overcome this drawback PANI is generally combined with other capacitive materials to form binary and ternary composites. [12, 13]

Nano cerium oxide (CeO_2) is a highly redox active ceramic oxide material which is gaining significant attention as an energy storage material. [27, 94, 95] CeO_2 is highly redox active and shows excellent cyclability. Despite these advantages, CeO_2 suffers from inherently low electrical conductivity, like many other pseudocapacitor materials. [94, 95] Recently, we studied the morphology and crystal plane dependent charge storage in CeO_2 using three different nano-morphologies: nanoparticles, nanorods, and nanocubes through electrochemical studies and molecular dynamics simulations. Among these three morphologies, nanorods showed considerably higher specific capacitance and rate performance. The superior electrochemical properties of the nanorods were ascribed to a combinational effect of high surface area and exposure of high energy crystal facets. [96] Graphene, an EDLC type material, shows great potential as a supercapacitor material due to its high theoretical capacitance, excellent chemical stability, and high electrical conductivity. [88, 89] Though graphene has traditionally been associated with high production costs, recent advancements in synthesis techniques have feasibly produced graphene at high throughput and low cost. [97, 98] However, re-stacking of the 2D graphene sheets due to the strong - interactions during cycling produces a significant capacitance fade. [99, 100] Since each of these materials has their

own set of advantages and drawbacks, it is logical to formulate a ternary compound, which exploits the advantage of one type of material to effectively suppresses the drawback of the other.

Though the reduced dimensions of nanomaterials pose various advantages such as shorter diffusion distances of the electrolyte ions and better electrochemical rate kinetics, the repeated cycling leads to agglomeration. This phenomenon eventually leads to undesirable outcomes such as an increase in internal resistance of the electrode and significant loss in capacitance.

A smart solution to overcome this problem is by taking advantage of hierarchical microstructures. Hierarchical microstructures are the assembly of nanostructured building blocks (0D,1D, and 2D nanomaterials) to form a 3D superstructure by a bottom-up approach. Hierarchical microstructures have a two-fold advantage; specifically, the micron-sized structure significantly helps the composites retain their structural stability during cycling without compromising the advantages of the nano-scale substructures. These advantages have made hierarchical microstructures popular in a wide range of applications like batteries, [101, 102] catalysts, [103, 104] sensors, [105, 106] and supercapacitors. [107-109] Moreover, hierarchical microstructures with a good distribution of different types of pores (micro, meso, and macro) have shown to be highly beneficial for charge storage application. This is due to the fact that the pores act as electrolyte ions buffer reservoirs, ensuring active material electrolyte contact even in the interior regions. [110]

The fabrication hierarchical microstructures by solution-based wet chemical techniques provide a promising route towards large scale synthesis. However, the self-

assembly of nanostructures usually involves the use of complex synthesis strategies and capping agents.[111] And porous hierarchical microstructures involve the use of templates. The main disadvantage associated with the use of the templates is the partial collapse of the structure during the template removal process. [112, 113] Furthermore, it is important to adopt an industry-scalable technique for the fabrication of hierarchical microstructures.

In this regard, we report here a template-free spray drying method to fabricate porous ternary hierarchical microspheres composed of PANI nanofibers, rGO, and CNRs. Spray drying is a well-established robust technique capable of mass production that is regularly used in the food, [114] pharmaceutical, [115] and thermal spray industry. [116, 117] Apart from its mass production capability, the ability of the process to tailor make structures with tunable surface area, internal structure, geometry, size, and porosity make it an attractive and well-suited process to synthesize multicomponent hierarchical structures. [118, 119]

The spray dried ternary hierarchical structure exhibited a high specific capacitance 684 F g^{-1} at a current density of 1 A g^{-1} in 1M H_2SO_4, excellent cyclability (~91% capacitance retention for 6000 cycles), and good rate capability. Moreover, an asymmetric device assembled with the ternary compound and rGO exhibits a wide operating voltage window (1.7 V) and high energy density (46.27 W h kg^{-1}) at a power density of 850 W kg^{-1}. The asymmetric device also exhibited good coulombic efficiency (92.73%) and a stable cycle life (90.56% capacitance retention) after 6000 cycles. These encouraging results suggest that the highly scalable ternary hierarchical

microspheres composed of PANI, rGO, and CNRs could be a viable electrode material candidate for practical supercapacitor applications.

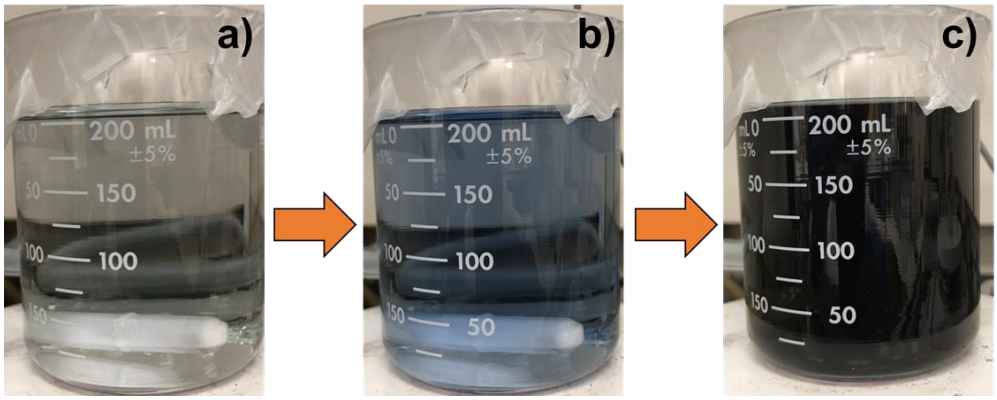

Figure 3.1: Digital photographs showing the progress of the PANI oxidation polymerization reaction at room temperature at different time points. a) few seconds after rapid mixing for 30 s. b) ~1 m after stopping the vigorous mechanical agitation. The onset of color change is a clear indicator of the start of the polymerization reaction. c) ~10 m after the initiation of the polymerization reaction

3.2 Experimental Section

3.2.1 Materials

Aniline, ammonium persulphate (APS) ((NH4)2S2O8), cerium nitrate hexahydrate (Ce(NO3)3•6H2O), sodium hydroxide (NaOH) were all purchased from Aldrich Chemical Co. N-methyl-2 pyrrolidone (NMP) and polytetrafluoroethylene (PTFE) were purchased from Alfa-Aesar. Carbon paper was purchased from FuelCellsEtc (AvCarb GDS3260). Microscope glass slides were purchased from Fisher. All materials were analytical grade and the reagents were used without any additional purification.

rGO was provided by Garmor Inc, a spin-off company from the University of Central Florida, which specializes in low-cost and bulk production of graphene derivatives.

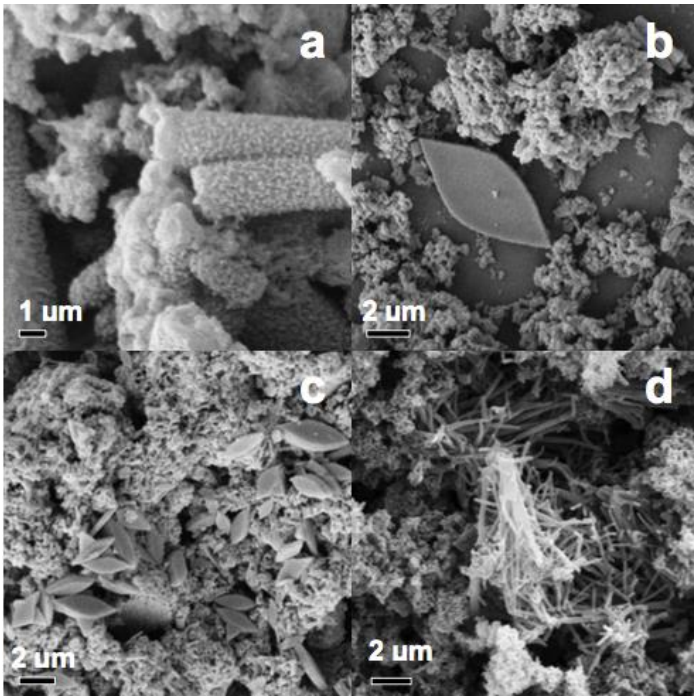

Figure 3.2: Morphologies of PANI obtained by different synthesis conditions. Aniline to APS molar ratio (1:1.25) in 1M HCl with constant stirring a) 4 °C 2 h, b) 4 °C 4 h. Aniline to APS molar ratio (1:1.4) 4 °C 2h and d) Room temperature (~25°C) 6 h.

3.2.2 Synthesis of PANI nanofibers

PANI nanofibers were synthesized through a modified oxidative polymerization route. [120, 121] In summary, 3 mL of aniline monomer was mixed thoroughly with 100mL of 1M HCl. Next, 1.8 g of APS was mixed with 100mL of 1M HCl. Finally, the APS solution was poured into the monomer solutions and rapidly mixed for ~ 30 s. The reaction was then allowed to proceed without any mechanical agitation for 2 h. The resulting greenish-blue solution was vacuum filtered and washed with copious amounts of 1M

HCl and acetone (Aldrich). The washed precipitates were vacuum dried at 60 °C for 12h and stored in glass vials for future use. It is worth mentioning that other popular PANI synthesis techniques, which involve low temperatures (due to the exothermic nature of the oxidative polymerization reaction), slow addition and continuous mixing of the reactants resulted in PANI with various morphologies and wide range of sizes (**Figure 3.2(a-d)** shows the typical morphologies obtained under such conditions). This is unfavorable because only the nanofiber morphology properly aids the formation of 3D microspheres by the spray drying process

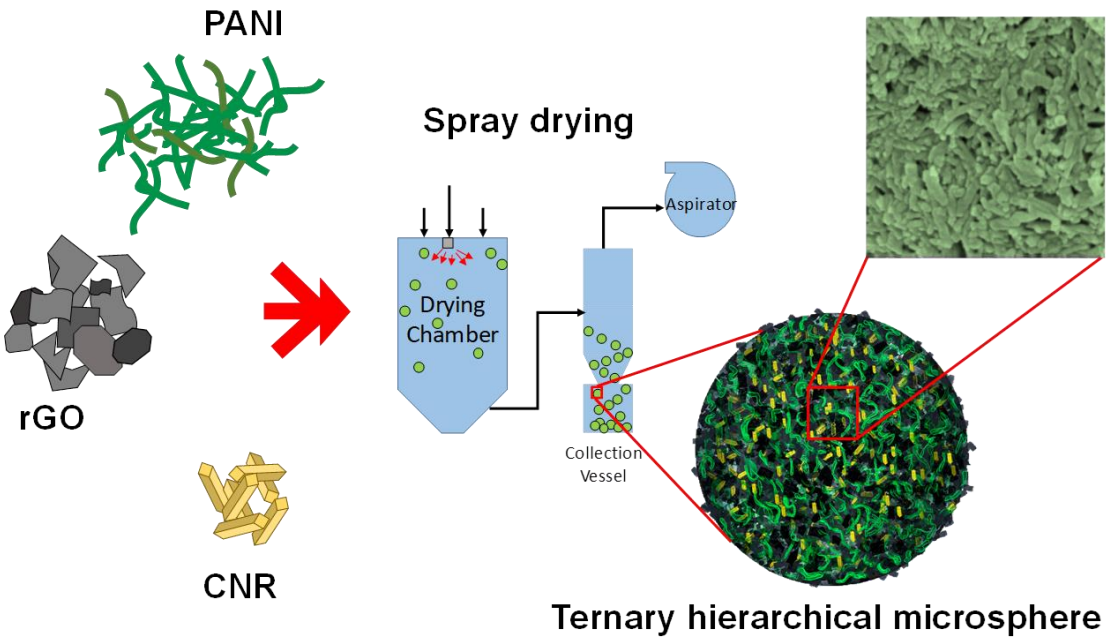

Figure 3.3: Schematic illustration of the synthesis process of the porous ternary hierarchical compound composed of PANI, rGO, and CNRs

3.2.3 Synthesis of CeO_2 nanorods

The CNRs were synthesized using a hydrothermal method. The details of which can be found in our previous work.[62] In brief, stoichiometric amounts of $Ce(NO_3)_3 \cdot 6H_2O$ and NaOH were mixed to 20 mL of deionized water (DI H_2O), separately. Next, the solutions were mixed vigorously together. This mixture was then transferred to a Teflon-lined stainless steel autoclave to ~85% volume capacity, sealed and held in an electric oven 120 °C for 24 h to yield CNRs. The precipitates were then collected, washed several times with DI H_2O through centrifugation, and vacuum-dried at 80 °C overnight. CNRs are formed by a self-assembly of CeO_2 nanoparticles through Ostwald ripening and oriented attachment, which have been previously documented. [122-124]

3.2.4 Synthesis of ternary hierarchical microspheres

The ternary microspherical compound was synthesized by spray drying method. The overall preparation of the hierarchical ternary microspheres is illustrated in **Figure 3.3** First, 270mg PANI was mixed thoroughly in 50 mL DI H_2O and ethanol for 30 mins using a horn ultrasonicator. To this, 15 mg of rGO was then added and the ultrasonication was continued for 15 mins. Finally, 15 mg CNRs was added to this solution and further ultrasonicated for 15 more mins. The resulting solution was spray dried with in-situ ultrasonication using a Buchi B-290 spray dryer fitted with an ultrasonic nozzle. The dried microspheres were collected and stored in glass vials for further use. This ternary compound is labeled PR_5C_5 (i.e 90 wt% PANI, 5 wt% rGO, and 5 wt% CNRs). Similarly, binary compounds: PR_{10} and PC_{10}, and ternary compounds: PR_9C_1, and PR_1C_9, were also synthesized for comparison. Optimized spray drying parameters

are crucial to obtaining the hierarchical microspheres and parameters used in this study are listed in **Table 3.1**.

Table 3.1: Optimized spray drying parameters to obtain highly porous hierarchical ternary microspheres.

Inlet temperature (°C)	Outlet temperature (°C)	Aspirator (%)	Pump (%)	Airflow (mm Hg)	Nozzle power (W)
180	93	90	6	25	2.6

3.2.5 Materials Characterization

The X-ray diffraction (XRD) patterns of the ternary hierarchical microspheres and other compounds were recorded using a PANalytical Empyrean diffractometer operated with a Cu X-ray source for 2θ from 10° to 90°. The morphology of the spray dried composites was analyzed using a Zeiss ULTRA-55 SEM. The morphology of the CNRs was analyzed using a Philips Tecnai 300 kV HRTEM. FT-IR spectrums of the ternary compounds were recorded using PerkinElmer Spectrum One FT-IR spectrometer. Raman spectra were collected from 300 cm^{-1} to 3000 cm^{-1} using a Renishaw RM 1000B spectrometer with an Ar 514.5 nm laser source. Surface areas and pore size distribution of the samples were measured using Quantachrome Nova-e surface area analyzer. All PANI based samples were vacuum degassed at 80 °C for 12 h and CNRs were vacuum degassed at 120 °C for 12 h before surface area measurements. X-ray photoelectron spectroscopy (XPS) measurements were performed on an ESCALAB-250Xi

spectrometer at room temperature in ultra-high vacuum chamber (below $7x10^{-9}$ mbar) using a monochromatic Al-Kα radiation source, operating at a power of 300 W (15 kV, 20 mA). The spot size of the beam was 650 µm. C 1s peak at 284.6 eV was used as a reference for calibration. Avantage Peakfit® software was used to deconvolute XPS spectra and identify the chemical functional groups.

3.2.6 Electrochemical characterization

Electrochemical measurements were performed with 1 M H_2SO_4 aqueous electrolyte at room temperature. In a three-electrode configuration, saturated Ag/AgCl (saturated NaCl) and Pt mesh were used as the reference and counter electrodes, respectively. Carbon paper was used as the current collector. Working electrodes were fabricated by thoroughly mixing the active material, PTFE, and carbon black in an 85:5:10 mass ratio, respectively. A homogeneous slurry of this mixture prepared using small volumes of NMP was applied to a carbon paper electrode, which was dried under vacuum overnight at 60 °C. ~2 to 3 mg of active material was loaded on to all working electrodes. All electrochemical measurements were carried out using a Bio-logic VSP electrochemical workstation. Cyclic voltammograms (CVs) were performed over a voltage range of -0.2 to 0.8 V at potential sweep rates from 5 to 100 mV s^{-1}. Galvanic charge/discharge curves (GCDs) were recorded over the voltage range of 0 to 0.8 V at specific currents from 1 to 20 A g^{-1}. The electrochemical impedance spectroscopy (EIS) studies were carried out near open circuit potential with an ac amplitude of 10 mV from 100 KHz to 0.1 Hz. In a two-electrode configuration, a glass fiber filter paper saturated

with 1M H_2SO_4 is sandwiched between two carbon paper electrodes loaded with the active material; this assembly was finally held between two microscope glass slides.

3.3 Results and discussion

The morphology and structure of the individual nanostructured components and the spray dried hierarchical compounds characterized through SEM and TEM is presented in **Figure 3.4(a-f)**. PANI in **Figure 3.4a** displays a clear nanofibrous structure which is ~50 nm in width and 500 nm to 1 µm in length. **Figure 3.4b** shows that rGO exhibit clear sheet-like structures. The TEM and HRTEM images of CNRs in **Figure 3.4c** and insert exhibits rod shaped structures of width 20-30 nm and length 350-450 nm. The lattice fringes displayed in the HRTEM insert image exhibit interplanar spacing of 0.31 nm, 0.28 nm, and 0.19 nm that corresponds to the (111), (200), and (220) family of planes. Furthermore, it can also be observed that CNRs exhibit 1D growth along the [110] direction and are enclosed by (111), (200), and (220) planes. The spray dried hierarchical microspheres are shown in **Figure 3.4(d-f)**. **Figure 3.4d** clearly shows that spray drying using an ultrasonic nozzle offers a tight distribution over the size of the microspheres. From **Figure 3.4d** insert and **Figure 3.4f** is can be observed that hierarchical structures are highly porous and displays pores of different sizes which can be beneficial to achieve the maximum charge storage capacity of the active material.

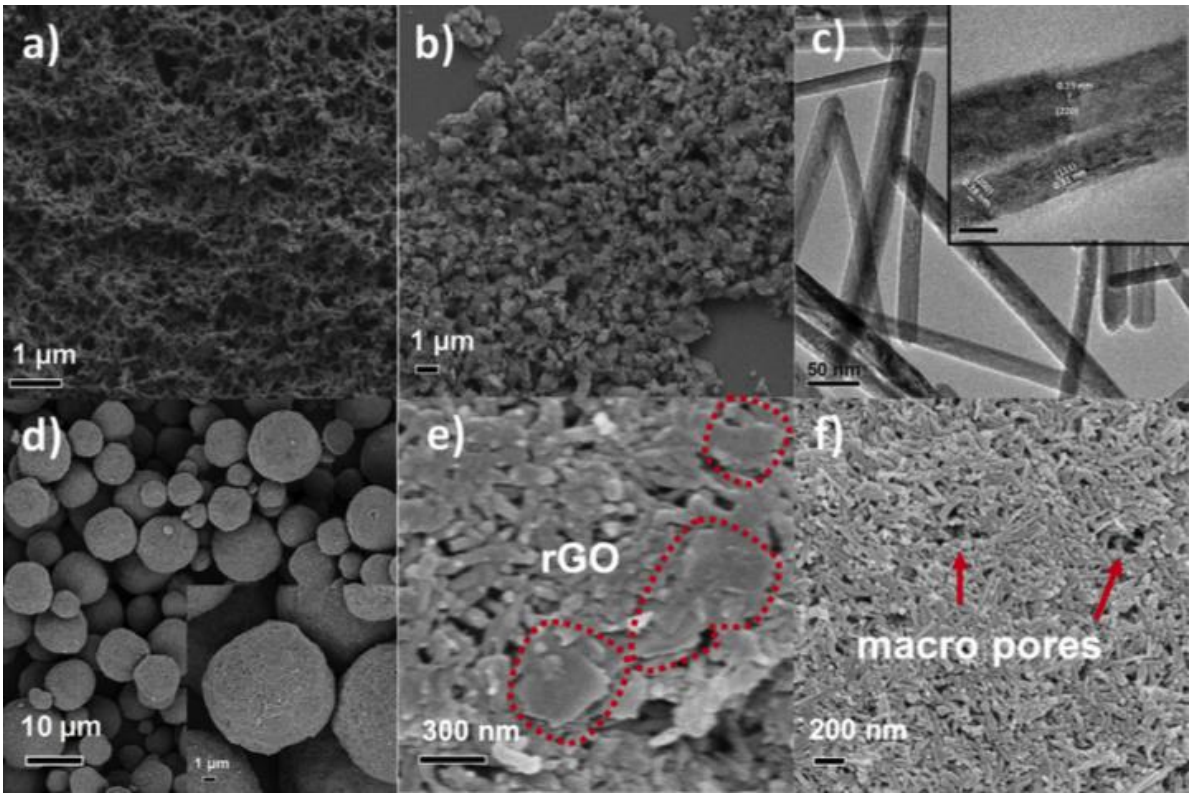

Figure 3.4: Morphological characterization of ternary hierarchical microspheres and nano sub-structures. SEM image of a) PANI nanofibers and b) rGO sheets. c) TEM image and HRTEM of the CNRs displayed in the insert. FESEM image of d) spray dried hierarchical structures; higher magnification 3D microsphere shown in the insert, e) rGO sheets embedded into the 3D PANI network, and f) the porous morphology of microspheres.

The high magnification SEM image (**Figure 3.4e**) displays a PANI 3D microspherical network with 2D rGO embedded into it. The 3D network of PANI could also prevent the aggregation of CNRs during repeated cycling. Thus, the ternary porous

3D hierarchical microspherical morphology could be highly beneficial for supercapacitor application.

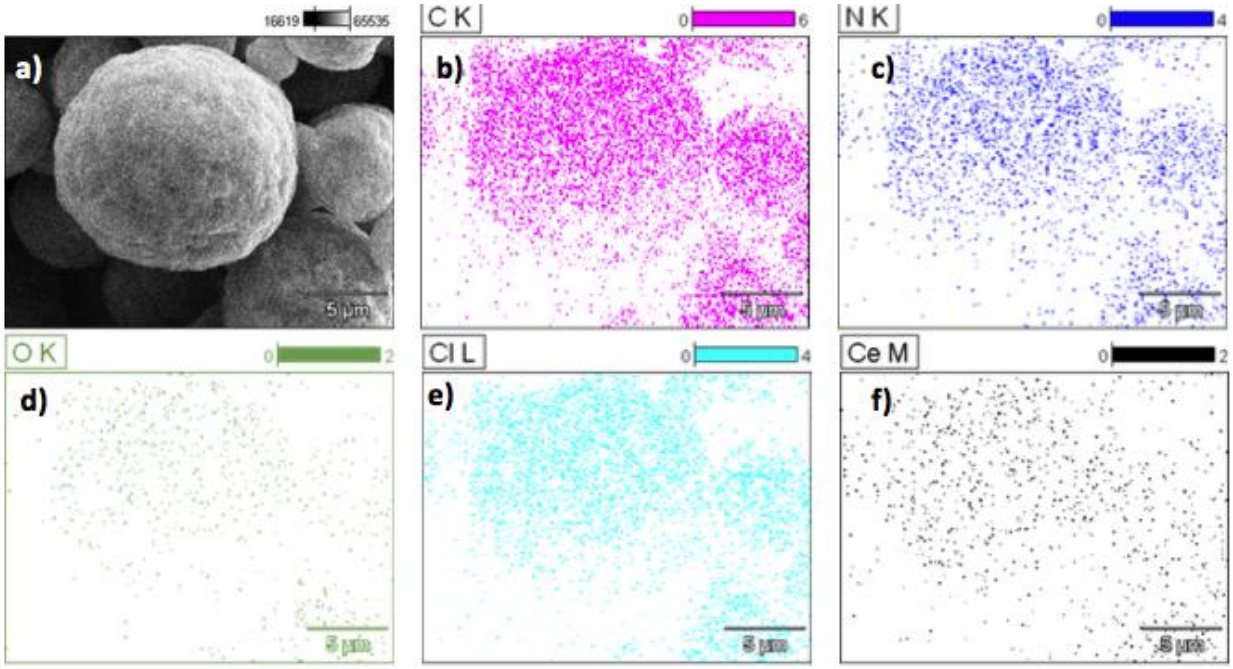

Figure 3.5: Elemental mapping images of hierarchical microspheres. a) SEM image of the microsphere. (b-f) EDX mapping of the total C, N, O, Cl, and Ce content in a typical ternary PR_5C_5 sample.

The elemental mapping of the hierarchical microspheres (**Figure 3.5 (a-f)**) in shows the presence of the various elements such as C, N, O, Cl and Ce, which are uniformly distributed throughout the ternary microspheres. It is worth mentioning that the use of PANI nanofibers is highly essential for proper formation of the microspherical morphology.

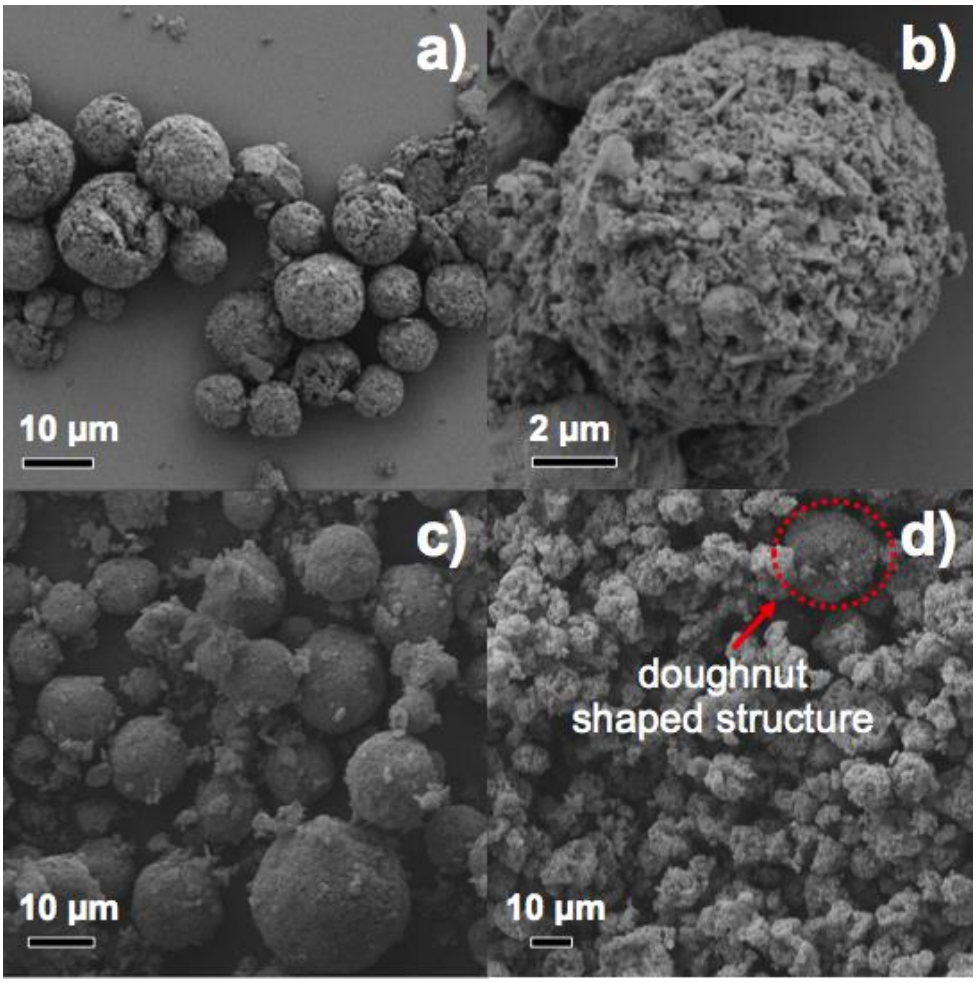

Figure 3.6: Effect of PANI morphology and spray drying parameters on the morphology of the hierarchical microspheres. (a-b) Spray dried PC_{10} composition using irregular PANI morphologies. Spray dried microspheres with non-optimized spray drying parameters: c) PC_{10}, and d) PR_5C_5 shows highly irregular, non-spherical, and doughnut-shaped structures.

From **Figure 3.6(a-b)** it can be clearly seen that PANI with mixed nano and microstructures and different morphologies lead to the formation of non-spherical/ broken spheres during the spray drying process. These structures are undesirable and

could have poor electrochemical properties. Optimized spray drying settings are another crucial parameter to obtain hierarchical microspheres (**Figure 3.6(c-d)**). Non-optimized parameters also lead to non-spherical/ broken spheres

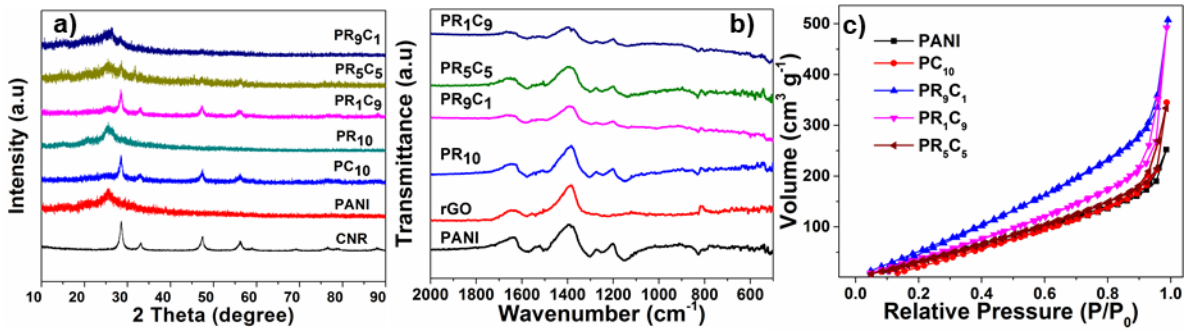

Figure 3.7: Structural and chemical analysis of PANI, CNR, and spray dried composites. a) XRD pattern of CNR, PANI, PC_{10}, PR_{10}, PR_9C_1, PR_5C_5, and PR_1C_9. b) FT-IR spectra of PANI, rGO and other binary and ternary compounds. C) Nitrogen adsorption-desorption isotherms of PANI, PC_{10}, PR_9C_1, PR_5C_5, and PR_1C_9 at 77k. PR_9C_1 exhibits highest surface area (418 m^2 g^{-1}) and porous structure, which could be highly beneficial for maximum charge storage

Figure 3.7a shows the XRD spectra of PANI, CNR, and different binary and ternary structures. Peaks in the CNR XRD spectra can be assigned to the pure cubic fluorite phase of CeO_2 (JCPDS 34–0394, space group Fm-3m). Diffraction peaks are indexed as (111), (200), (220), (311), (222), (400), (331), and (420) planes of CeO_2. [124] The crystallite size of CNRs is estimated as 39.77 nm using the Scherrer equation ($d = C\lambda/B\cos\theta$), where, d is the mean crystallite size, C is a shape factor (crystallite dependent), λ is the X-ray wavelength, B and θ are the full width at half maximum

intensity, and the Bragg angle, respectively. PANI is known to have a semi-crystalline structure, with islands of crystalline zones surrounded by amorphous regions.[125] This gives rise to several XRD peaks. The pronounced XRD peaks at 15°, 21°, and 25.5° correspond to the (011), (020) and (200) plane reflections of the emeraldine form of PANI.[125, 126] rGO shows a broad reflection at 26°, which overlaps with PANI peaks, leading to broad peaks in the binary and ternary microspheres. The clear peaks of PANI, rGO, and CNRs suggest the successful incorporation of three nano-substructures into the spray dried ternary compounds. The lower intensity of the CNR peaks in PR_5C_5 and PR_9C_1 compared to PR_1C_9 and PC_{10} can be attributed to the reduced concentrations of CNRs in these compounds.

The FT-IR spectra of PANI nanofibers, rGO, and spray dried composites are presented in **Figure 3.7b**. Neat PANI shows typical peaks at 1582 cm^{-1} and 1507 cm^{-1} associated with the stretching of the quinoid and benzenoid rings. The C-N stretching of the aromatic amines is observed by the peaks at 1380 cm^{-1}, 1311 cm^{-1}, and 1240 cm^{-1}.

The 1158 cm^{-1} peak is ascribed to in-plane C-H bending, which is a degree of localization of the electrons. Peaks at 828 cm^{-1} and 514 cm^{-1} are attributed to the out of plane C-H bending. The shoulder peak at 810 cm^{-1} represents the C-Cl stretching, which confirms that PANI is doped by HCl.[127] The main rGO peak at 1580 cm^{-1} is due to the stretching of C=C. rGO also shows weak peaks at 1728, 1627, and 1247 cm^{-1} associated with the C=O, adsorbed H_2O, and C-O, respectively.

The binary and ternary compounds show all the peaks of PANI and rGO. However, the PANI peaks are shifted to lower wavenumbers (**Figure 3.8b**), which could

be attributed to the π-π interaction between PANI and rGO.[128] Moreover, the Ce-O vibrational peak centered at 517 cm^{-1} indicates the presence of CeO_2 in the ternary mixture.[129] These verify the successful incorporation of PANI, rGO, and CeO_2 into the ternary compound.

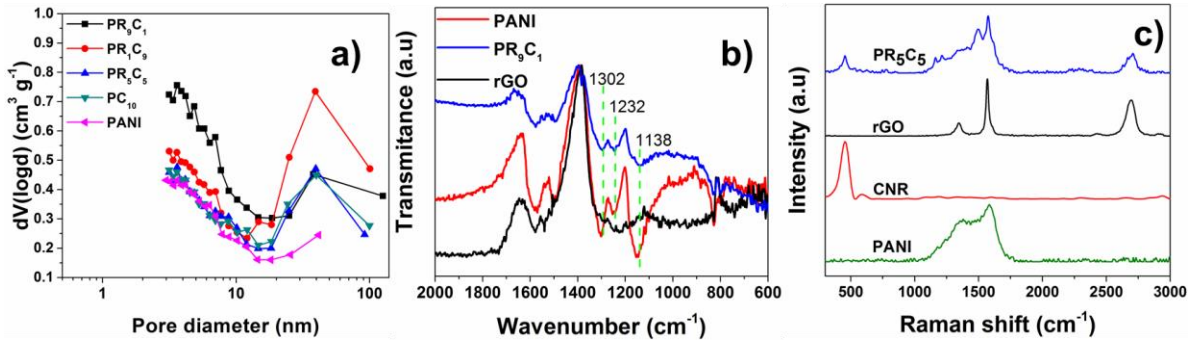

Figure 3.8: a) BJH Pore size distribution of PR_9C_1, PR_5C_5, PR_1C_9, PC_{10}, and PANI. b) FT-IR spectra of PANI, rGO and PR_9C_1. c) Raman spectra of PANI, CNR, rGO, and PR_5C_5.

Raman analysis was further performed on PANI, rGO, CNR, and ternary compound to verify the π-π interactions (**Figure 3.8c**). rGO shows D band and G band at 1324 cm^{-1} and 1568 cm^{-1} associated with the defects and the sp^2 structure, respectively. The strong 2D band at 2696 cm^{-1} suggests the multilayered nature of rGO. CNR show a peak at 455 cm^{-1} associated with the F2g Raman active mode of the fluorite structure and a weak peak at 586 cm^{-1} due to the surface defects.[130] PANI shows peaks at 1625 cm^{-1} and 1601 cm^{-1} associated with the benzenoid and quinoid ring stretching. The peaks at 1201 cm^{-1} and 1164 cm^{-1} can be related to the in-plane C-H bending of the the benzenoid and quinoid structures. The $C\text{-}N^+$ stretching peak

appears at 1343 cm^{-1}.[131]The ternary structure exhibits peaks of PANI, rGO and CNR. In addition, the ternary compound showed a shift in the G band to 1573 cm^{-1} and 2D band to 2710 cm^{-1}, which suggests π-π interactions between rGO and PANI.[132]

The surface area and porosity of the spray dried hierarchical microspheres were analyzed from the N_2 adsorption/desorption isotherms at 77 K shown in **Figure 3.7c**. The isotherms can be classified as type II (IUPAC classification) and show a H3 type hysteresis.[133] This is a characteristic feature of a mixture composed of plate-like substructures. It also suggests the existence of macropores, in agreement with SEM images. PR_9C_1 shows the highest adsorption capacity suggesting highest surface area. All structures show a hysteresis loop, at relative pressures of 0.8-0.9, which suggest the presence of mesopores.[134] The sudden increase/decrease in the isotherms close to the saturation pressure suggests the filling of large mesopores and macropores.[134] PR_5C_5 shows the highest increase near the saturation pressure, suggesting PR_5C_5 could possess a high marcopore density.

The surface area obtained by Brunauer-Emmett-Teller (BET) analysis was estimated as 418 $m^2\ g^{-1}$, 313 $m^2\ g^{-1}$, 309 $m^2\ g^{-1}$, 266 $m^2\ g^{-1}$, and 237 $m^2\ g^{-1}$ for PR_9C_1, PR_5C_5, PR_1C_9, PC_{10}, and PANI, respectively. The pore volume distribution estimated through the Barrett-Joyner-Halenda (BJH) method is presented in **Figure 3.8a**. It can be observed that there is a good distribution of pores in the mesoporous and macroporous region. The presence of meso and macropores ensures maximum charge storage utilization of the active material, as they can act as not only as pathways, but also serve

as electrolyte ion buffer zones which can ensure the maximum supply of ions even to the remote interior regions in the microsphere. [110] [135]

XPS (**Figure 3.9**) was carried out on all the starting materials and ternary compounds to detail surface elemental compositions, oxidation states, and doping efficacy for PANI-derived materials. The full XPS survey spectral lines of PANI, rGO, and PR_9C_1 are presented in **Figure 3.9a**. PANI contains C, O, N, and Cl as the primary elements, which is in good agreement with the previous reports.[136, 137] The survey spectrum of rGO shows the typical peak of C with a negligible quantity of O, suggesting only a minimal presence of surface oxygen moieties. The ternary compound, PR_1C_9, clearly exhibits the individual peaks of C, O, N, Cl, and Ce, resulting from the PANI, rGO, and CNRs. The relative concentrations of C, O, N, Cl, and Ce in the PANI derivatives, quantified from the equivalent photoelectron peak area are itemized in **Table 3.2**. The C/N ratio of neat PANI and PR_9C_1 are 6.15 to 6.4, respectively, which is close to the theoretical value of 6. The quantified atomic % of Ce element was 0.12 which is equivalent to 1.19 wt %, in good agreement with the 1 wt % of CeO_2 in PR_9C_1. The high-resolution XPS Ce (3d) spectrum presented in **Figure 3.9b** shows the mixed oxidation state ($3^+/4^+$) of the 1 wt% CNRs in PR_9C_1. **Figure 3.9c** shows the N 1s envelop of PR_1C_9 fitted into four peaks. The peaks centered at 398.4 and 399.3 eV are characteristic peaks of di-imine nitrogen (-N=) and benzenoid di-amine nitrogen (-NH-), respectively.[138, 139] In addition, the peaks at 400.4 and 402.4 eV are ascribed to N^+ state.[139]

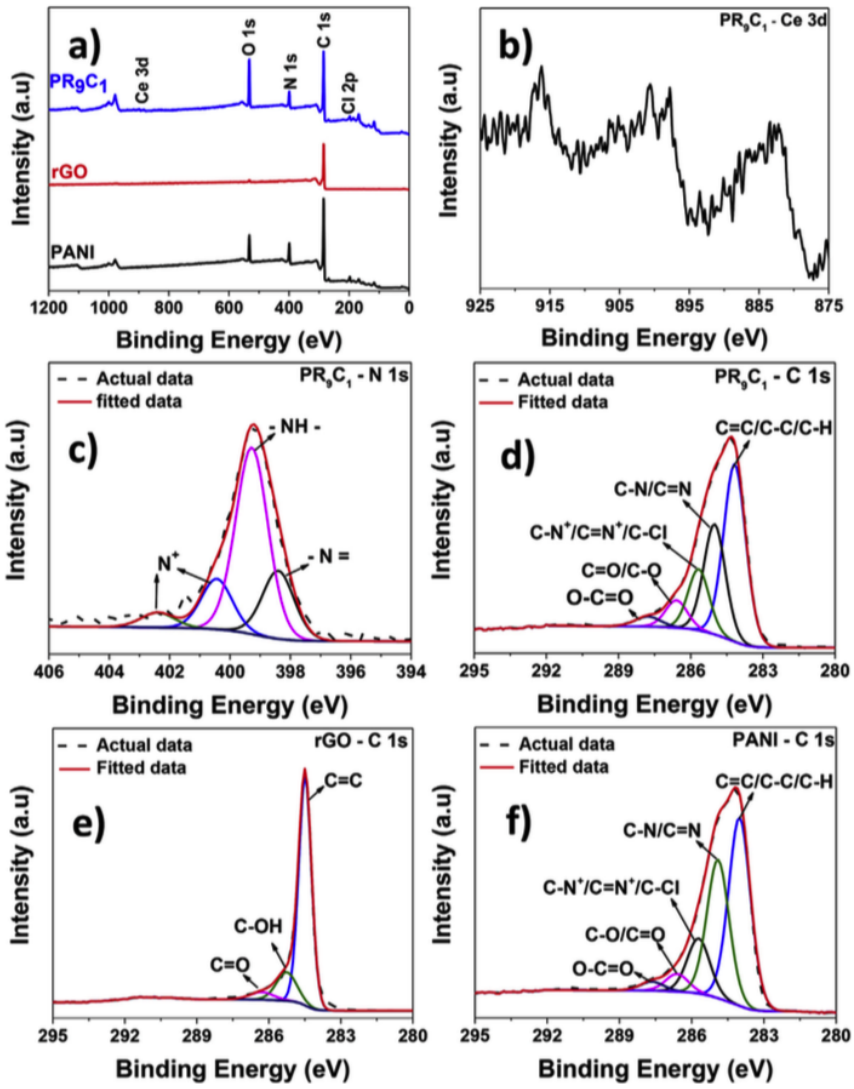

Figure 3.9: Surface elemental analysis of hierarchical ternary microspheres and nano-substructures. Survey spectra (a) and selective high-resolution XPS spectra (b-f) of PANI, rGO, and PR_9C_1. (a) Survey spectrum of PANI show clear presence of C, N, O, and Cl. PR_9C_1 survey spectrum matches with PANI and exhibits clear Ce peak. (b) Ce 3d spectral emission from PR_9C_1 depicts the mixed cerium oxidation peaks of 1 wt% of CNR. (c) and (d) deconvoluted high resolution N 1s and C 1s spectra of PR_9C_1. (e) and (f) deconvoluted and fitted C 1s XPS spectra of rGO and PR_9C_1

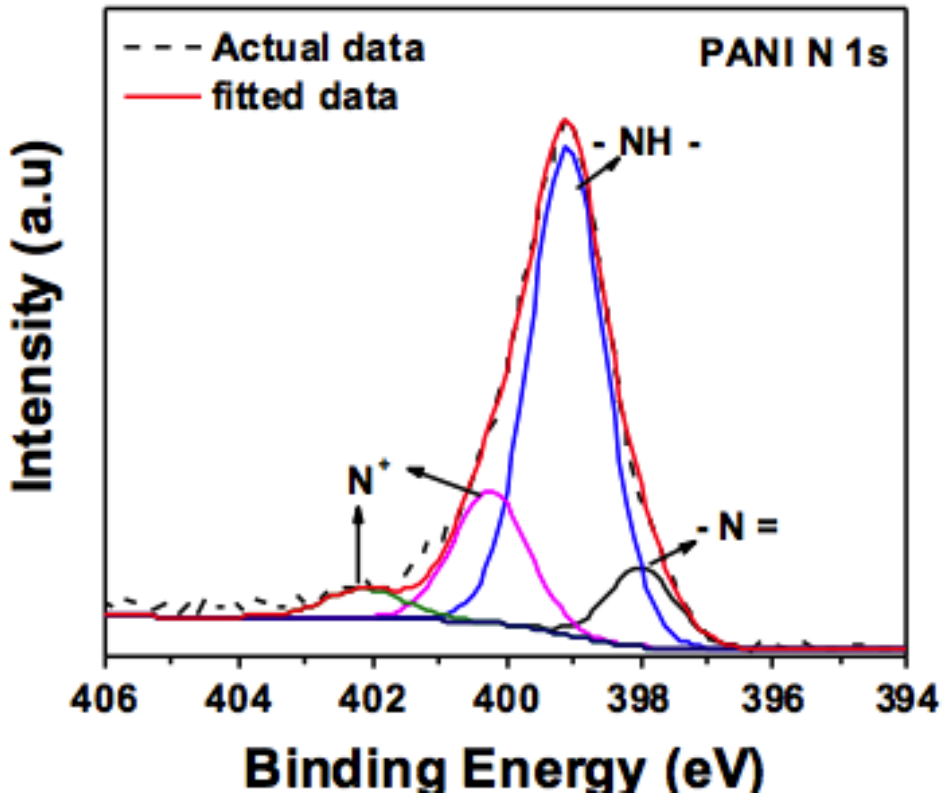

Figure 3.10: Deconvoluted and fitted high resolution N 1s spectrum of PANI.

Two important factors that can be extracted from the deconvoluted N 1s high-resolution spectrum are oxidation state and doping level of the PANI-based compounds. The general form of PANI can be expressed as $[(\text{-B-NH-B-NH-})_x(\text{-B-N=Q=N-})_{1-x}]_n$ where B and Q are the benzenoid and quinoid rings, respectively. The oxidation state of PANI can range from the fully reduced leucoemeraldine (x = 1), protoemeraldine (x = 0.75), emeraldine (x = 0.5), to the fully oxidized pernigraniline (x = 0). Thus, the oxidation state can be estimated based on the -NH-/-NH= ratio. PR_9C_1 and neat PANI contains 59%, 67% amine nitrogen and 21%, 10% imine nitrogen, respectively. This corresponds to a PANI oxidation state between emeraldine and protoemeraldine.[138, 140] Conductivity of PANI is achieved through either protonation of amine nitrogen (-NH-) in emeraldine or

oxidation of imine nitrogen (-NH=) in leucoemeraldine. Thus, the level of doping could be used as a measure of conductivity. The doping level in neat PANI and the binary and ternary samples is estimated through the ratio of the positively charged nitrogen (N+) to the total nitrogen present. The slight increase (~11%) in the imine nitrogen from PANI to PR_9C_1 could be due to mild oxidation during the spray drying process. However, the doping level in both the compounds remain relatively similar; 22.5% and 20% for PANI and PR_9C_1, respectively.

Figure 3.9d displays the five deconvoluted peaks of the high-resolution C 1s spectral line. The peaks at 284.4, 285.1, 285.7, 286.7, and 287.9 eV are attributed to the C-C/C=C/C-H, C-N/C=N, C-N+/C=N+/C-Cl, C-O/C=O, and O-C=O species, respectively. The first two peaks at 284.4 and 285.1 eV associated with C-C/C=C/C-H and C-N/C=N form the backbone of the PANI structure and exhibit relatively higher intensity. All deconvoluted peaks in the C 1s envelope of PR_9C_1 match with the fitted C 1s envelope of neat PANI in **Figure 3.9e**. And the existence C-Cl confirms the protonated state of the polymer compounds.[138] This clearly suggests the incorporation of PANI in the ternary mixture.

The peaks at the lower binding energies ((C-O/C=O) and O-C=O) saw a shift to higher energies by 0.28 eV and peak broadening of C-C/C=C peak (see the narrow C-C peak and minor C-O, and C-OH peak in **Figure 3.9e**. This result suggests that the electronegativity of PR_9C_1 ternary compound is stronger than that of neat PANI.[141] This may be attributed to the interaction between CNRs, rGO, and PANI, in the spray dried

compound. This is good agreement with the peak shifts in FTIR results, which suggests interactions between PANI and rGO in the ternary mixture.

Table 3.2: Compositions (at%) of PANI, rGO, and PR_9C_1 quantified from corresponding XPS survey spectra.

	C	**O**	**N**	**Cl**	**Ce**
PANI	76.3	9.27	12.41	2.02	-
rGO	97.68	2.32	-	-	-
PR_9C_1	68.45	18.81	10.66	1.96	0.12

The electrochemical properties of the spray dried hierarchical microspheres and neat PANI nanofibers were first evaluated by cyclic voltammetry (CV) in a three electrode configuration with 1 M H_2SO_4 electrolyte between -0.2 V and 0.8 V at various scan rates from 5 to 100 mV s^{-1}.

All CVs in **Figure 3.11a**. exhibit a rectangular shape, with sharp redox peaks suggestive of the active material's pseudocapacitive nature.[128, 142] The three distinctive redox peaks are associated with the transition between different states of PANI. Specifically, the first redox pair labeled O_1/R_1 between 0 - 0.3 V is attributed to the transition between the semiconductive and conductive states of PANI (leucoemeraldine to emeraldine). O_2/R_2 peaks between 0.3 V - 0.65 V are associated with other structure such as benzoquinone-hydroquinone couple. Lastly, the third set of peaks O_3/R_3

between 0.65 V - 0.8 V, is associated with the transition between pernigraniline and quinone diimine.[143, 144] The redox type charge storage in CNRs can be expressed by **Equation 2.1**.[96] Besides the redox processes, PANI and CNRs also contribute to store charge from the accumulation of ions at the electrode/electrolyte interface (EDLC). The charge storage in rGO is purely EDLC in nature. [7, 38]

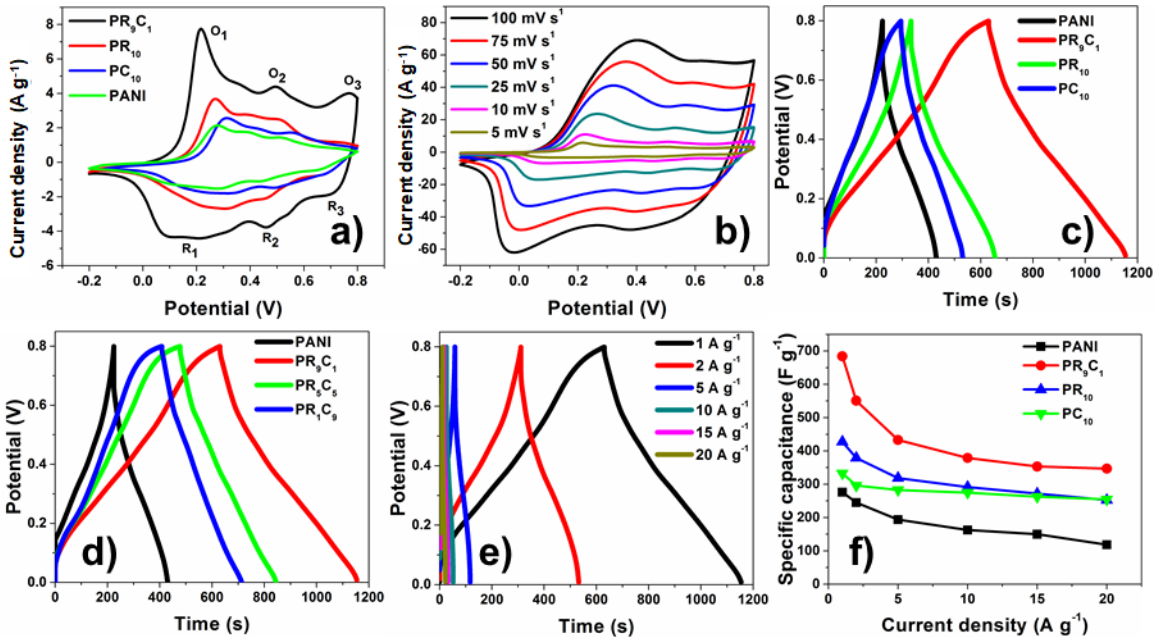

Figure 3.11: Electrochemical characterization of neat PANI nanofibers with binary and ternary hierarchical compounds in a three electrode system in 1M H_2SO_4. a) CVs of PANI, PR_{10}, PC_{10}, PR_9C_1 at 5 mV s^{-1} and b) CVs of PR_9C_1 at different scan rates. GCD comparison curves of d) PANI, PR_{10}, PC_{10}, and PR_9C_1 and d) all ternary composites with PANI at 1 A g^{-1}. e) GCD curves PR_9C_1 at different current densities. Specific capacitance values as a function of current density for PANI, PR_{10}, PC_{10}, PR_9C_1.

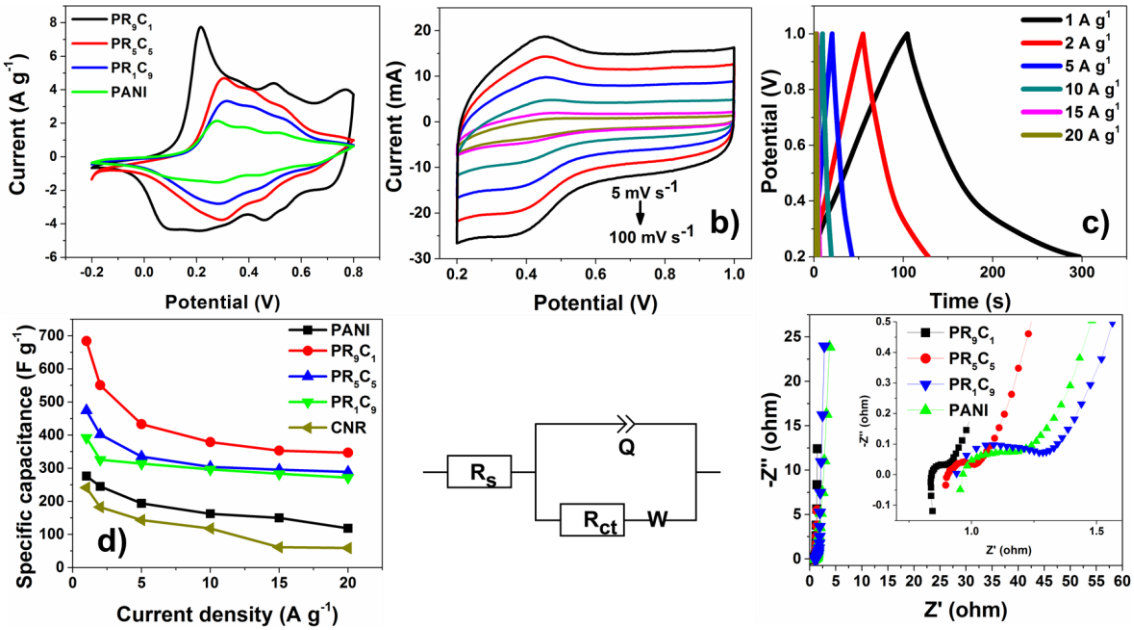

Figure 3.12: Three electrode electrochemical characterization of neat PANI, CNR and other hierarchical compounds in 1M H_2SO_4. a) CVs of PANI, PR_9C_1, PR_5C_5, and PR_1C_9 at 5 mV s^{-1}. c) CVs of CNRs from 5 to 100 mV s^{-1}. c) CDs of CNRs 1 to 20 A g^{-1}. d) Specific capacitance as a function of current density for PANI, CNR, PR_9C_1, PR_5C_5, and PR_1C_9. e) equivalent circuit model used to extract the R_s and R_{ct} values from the EIS curves. f) EIS curves of neat PANI compared to other ternary compounds.

Figure 3.12a compares the CVs of PANI, binary PC_{10} and PR_{10}, and ternary PR_9C_1 at a scan rate of 5 mV s^{-1}. It is clear that the area enclosed by the CV of PR_9C_1 is much larger than neat PANI and the binary counterparts. The higher current response clearly suggests PR_9C_1 possesses the largest specific capacitance. **Figure 3.12a**. compares the CVs of the three ternary compounds to neat PANI. The response current in the CVs indicate that the charge storage performance follows the trend: PR_9C_1 > PR_5C_5 > PR_1C_9. Though CNRs are highly redox active and can prevent the restacking

of the graphene sheets, large quantities of CNRs may result in agglomerated structures; limiting supercapacitor performance.[128, 137, 145] This clearly shows an optimal ratio of the three components is crucial for maximum charge storage.

The CVs of the PR_9C_1 from 5 to 100 mV s^{-1} are compared in **Figure 3.11b**. The CVs still retains an almost rectangular shape and show clear redox peaks even at higher scan rates, suggesting good rate performance and high kinetic reversibility of the electrode.[146] With an increase in potential scan rate, the oxidation peaks shift slightly to a more positive potential and reduction peaks shift to more negative potentials. The peak shifts could be attributed to the increased diffusion resistance at higher scan rates.[128, 142]

To further understand the supercapacitive properties of the hierarchical microspheres, GCD measurements were carried out in a potential range between 0 V and 0.8 V at current densities varying from 1 A g^{-1} to 20 A g^{-1}.

The GCDs in **Figure 3.11(c-e)** exhibit an almost symmetric shape at all current densities, which further suggest the excellent reversibility of the electrodes.[129, 132] Slight deviations from the symmetry in shape of GCDs could be attributed to the faradaic reactions.[136] **Figure 3.11e** displays the typical GCD curves of PR_9C_1 from 1 A g^{-1} to 20 A g^{-1}. The small iR drop, at the beginning of the discharge portion of the curve, is attributed to the internal resistance of active electrode material.[129, 147] **Figure 3.11c** represents the GCDs of PR_9C_1, PC_{10}, PR_{10}, and Neat PANI at 1 A g^{-1}. From the discharge times, it can be predicted that the specific capacitance of PR_9C_1 > PR_{10} > PC_{10} > PANI. **Figure 3.11d** compares the GCDs of the various ternary compositions. It

is clear from the discharge time that PR_9C_1 possesses the highest charge storage, which is in good agreement with the CV results.

From the GCD curves, the specific capacitance (*SC*) of all electrodes can be estimated using **Equation 2.4**.The SC of PR_9C_1, PR_{10}, PC_{10}, and PANI was 684 F g^{-1}, 427.5 F g^{-1}, 332.5 F g^{-1}, and 278 at 1 A g^{-1} and 347F g^{-1}, 252 F g^{-1}, 255 F g^{-1}, and 117.5 F g^{-1} at 20 A g^{-1}. This clearly shows that optimized, well-integrated ternary hierarchical structures exhibit superior electrochemical properties relative to the binary and ternary counterparts.

Figure 3.11f shows the change in *SC* with respect to the current density. It is clearly observed that the SC decreases with increasing current density. Lower *SC* at higher current densities is due to the higher electrolyte diffusion resistance into the electrode.[71] This could severely restrict the charge storage to just the surface of the composite, leading to underutilization of active material. The slower response of the active materials at higher current densities could also affect the charge storage capacity. However, this is not the case(minimal diffusion resistance) at lower current densities which allows for maximum charge storage.[70]

To further understand the charge transfer characteristics of hierarchical 3D structures EIS was performed on the electrodes. Nyquist plots of the various electrodes are shown in **Figure 3.13a**. The intersection of impedance response to the X-axis gives R_s, which is the sum of the solution and internal electrode resistance.[145, 148] Since the electrolyte solution resistance remains constant, the smaller R_s of PR_9C_1 (0.84 Ω) compared to PR_5C_5 (0.91 Ω), PR_1C_9 (0.94 Ω), and other active material implies lower

electrode resistance. At high frequencies, the Nyquist diagrams exhibit a semicircular region attributed to the accumulation of electrolyte ions at the electrode-electrolyte interface that happens concomitantly with the protonic ion exchange.[128] These events together produce a charge transfer resistance (R_{ct}), which can be estimated from the diameter of the semicircle.[128, 149] From **Figure 3.13a** insert, it can be clearly seen that PR_9C_1 (33 mΩ) exhibits a much lower R_{ct} than neat PANI (74.2 mΩ), PR_{10} (42.5 mΩ), and PC_{10} (114.2 mΩ); suggesting the combination of the three components and high surface area leads better electrolyte-active material interaction and lower charge transfer resistance.

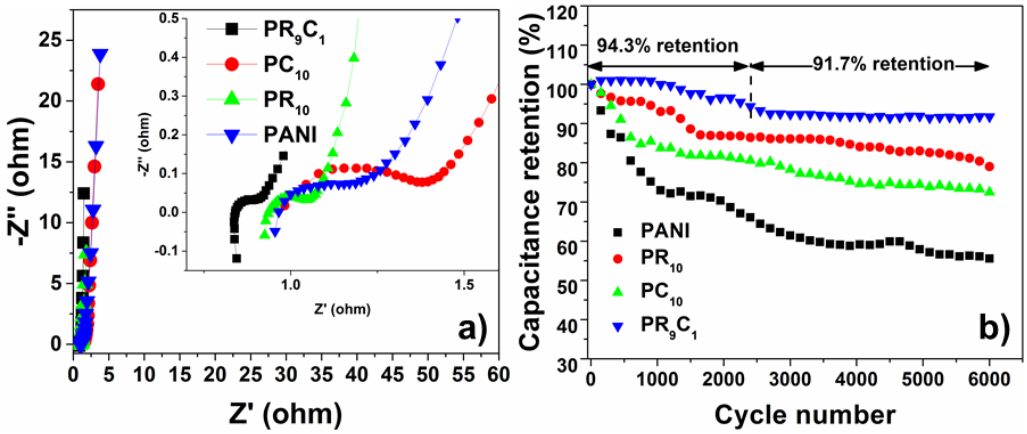

Figure 3.13: Electrochemical impedance spectroscopy and cyclability of the electrodes in a 3 electrode configuration. (a) EIS curves of neat PANI compared to the binary and ternary hierarchical compounds. b) Cyclic stability of PANI, PR_{10}, PC_{10}, PR_9C_1 at 4 A g^{-1}. PR_9C_1 exhibited excellent cyclability (91.7% capacitance retention) after 6000 cycles

Mid frequencies show a characteristic sloped line associated with Warburg diffusion; indicative of the semi-infinite diffusion of the electrolyte ions into the electrode.[149, 150] The higher slope of PR_9C_1 indicates better supercapacitor properties.

This is in good agreement with the porosity analysis measurements, which showed a good distribution of interconnected pores. The micro and mesopores act as pathways for electrolyte ion movement and macropores provide a constant supply of electrolyte to the interconnected pores.[110] At low frequencies, the impedance response raises to an almost vertical line, which can be associated with ideal capacitive behavior.[128] **Figure 3.12f** compares the impedance spectra from all three ternary compounds to neat PANI. It can be observed that increasing the CNR content leads to higher R_s and R_{ct} values, which could be due to the inherently poor conductivity of the CNRs.

Another plausible reason could be that excessive CNRs could lead to agglomeration, which might lead to lowered effective contact between the active material and electrolyte. The EIS results are in good agreement with the results from other electrochemical techniques.

Figure 3.13b shows the cyclic stability of the ternary structure and controls evaluated by GCD measurements at 4 A g^{-1}. Stable long term cyclic performance is a crucial factor that determines the viability of any EED. The repeated mechanical strains during the charge/discharge process severely cripple the cyclic stability of PANI.[93, 151] From literature, is clear that the capacitance fade in PANI can reach 50% within the first 1000 cycles.[93, 143] However, from **Figure 3.13b** it is clear that the ternary PR_9C_1 synthesized in this study shows only a gradual decrease in capacity of 94.3% after 2400 cycles. The capacitance retention stabilized thereon and showed very minimal decay to ~ 92% after 6000 cycles. For comparison, the cycle life of the controls were also evaluated. After 6000 cycles, binary CNR and rGO composites, and neat PANI

electrodes show a capacitance retention of ~85% ~72.5 and ~55%, respectively. The excellent cyclic performance of the optimized 3D hierarchical porous ternary structure can be attributed to the combinational effect of highly conductive rGO and CNRs which work synergistically to effectively mitigate strains on the PANI structure during repeated cycling. [136, 152]

To understand the device performance, symmetric and asymmetric devices (ASD) were constructed. Though aqueous electrolytes are only stable over a potential window of ~1.23 V, the voltage window of these electrolytes can be extended well beyond by this limit by careful selection of different electrode materials. Such ASDs take advantage of the high oxygen and hydrogen overpotential limits of the respective positive and negative electrode.[153, 154] Here, an ASD is assembled with the ternary hierarchical composite as the positive electrode and rGO as the negative electrode (PR_9C_1 // rGO).

Usually, ASDs need to be charge balanced ($q^+=q^-$) such that the applied voltage is equally split between the electrodes for optimal performance.[153, 154] This leads to the mass balance equation $m^+/m^- = C^-V^-/ C^+V^+$, where m is the mass, C is the specific capacity, and V is the working potential window of positive/negative electrode. Accordingly, the mass ratio of the active materials (PR_9C_1 to rGO) is ~4.3. From the operation potential window of rGO and PR_9C_1 shown in **Figure 3.15c** the optimal working window of the ASD device was estimated to be 0 to 1.7 V. The ACD device exhibits no signs of polarization and decomposition of PANI in this region. The quasi-rectangular shape (**Figure 3.14b**) of the CVs even at a high scan rate of 100 mV s^{-1}

suggests the fast charge-discharge characteristics of the ASD. The GCDs in **Figure 3.14c** also display excellent symmetry between the charge-discharge regions and minimal IR drop suggesting excellent supercapacitor properties.

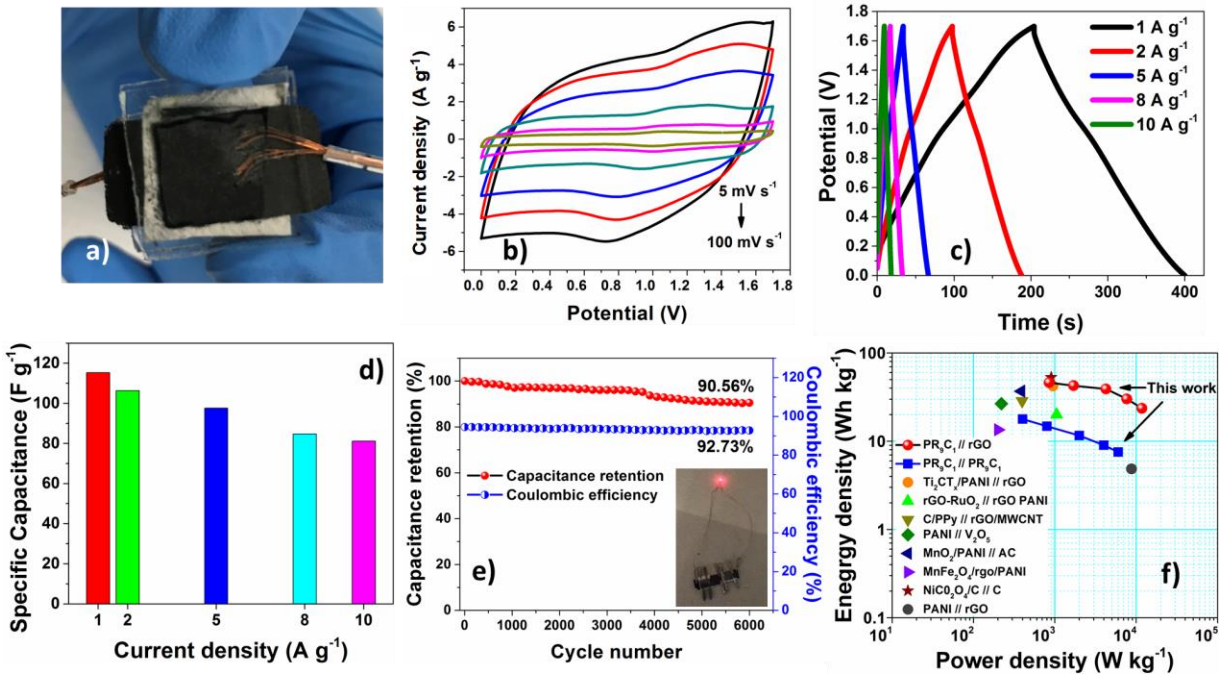

Figure 3.14: Capacitance and performance evaluation of the asymmetric device (ASD). a) Digital photograph of a fabricated device, which shows two electrodes with a filter paper separator. b) CVs of PR_9C_1 // rGO ASD at different scan rates at a voltage window of 1.7 V. c) GCD profiles of ASD at different current densities from 1 to 10 A g^{-1}. d) Specific capacitance of the ASD from 1 to 10 A g^{-1}. e) ASD shows excellent cyclability and coulombic efficiency after 6000 cycles. e insert) Digital photograph of a red LED power by two asymmetric supercapacitors connected in series. f) Ragone chart showing the energy and power densities of PR_9C_1//rGO and PR_9C_1//PR_9C_1 in comparison with other relevant supercapacitor.

Table 3.3: Summary of commercial supercapacitors with maximum energy and power densities.

Product	Operating voltage (V)	Max. Energy density (Wh kg^{-1})	Max. Power density (W kg^{-1})
Maxwell (BCAP0050 P300 X11)*	3	5.4	7200
ESMA	1.3	1.1	156
Ness	2.7	2.5	3040
Panasonic	2.5	3.44	1890
EPCOS	2.5	4.3	760
SkelCap(SCA32)*	2.85	6.8	34600
Maxwell	2.3	9.1	14000

The specific capacitance (C_s) of the asymmetric device was calculated from the following equation:

$$C_s = \frac{I\Delta t}{m\Delta V} \quad (3.1)$$

where *I* is the current (A), Δt is the discharge time (s), *m and* ΔV are the mass (g) of the active material in both the electrodes and the potential window (V), respectively. The ASD exhibited a C_s of 115.3 F g^{-1} at 1 A g^{-1} to 81.2 F g^{-1} at 10 A g^{-1} (**Figure 3.14d**)

The energy density (*E*) and power density (*P*) of the device are two crucial parameters that determine the practical applicability of an EED. And these were calculated using the equations:

$$E = \frac{1}{2} C_s \frac{V^2}{3.6} \tag{3.2}$$

$$P = \frac{E}{\Delta t} 3600 \tag{3.3}$$

where C_s is the specific capacitance (F g^{-1}) of the device, *V* is the potential window and *Δt* is the discharge time (*s*) of the device.

Ragone plots in **Figure 3.14f** show that the ASD exhibits an energy density of 46.3 Wh kg^{-1} at a power density of 850 W kg^{-1} and retains an energy density of 21.63 Wh kg^{-1} at a high power density of 11730 W kg^{-1}. It is clear that the energy density of ASD is more than double that of the symmetric device. From the Ragone plot and **Table 3.4**, it is clear that the ternary hierarchical microspheres exhibit a much higher energy and power density than most polyaniline based materials and very competitive properties compared to other aqueous high performance supercapacitor materials. The energy density of our ASD is also much higher than commercially available supercapacitors listed in **Table 3.3**. Moreover, the ASD also exhibited excellent cyclic performance with 90.56% capacitance retention and a high coulombic efficiency (92.7%) after 6000 cycles (**Figure 3.14e**). As a practical application, **Figure 3.14e** insert shows a digital photograph of a red LED (forward voltage 2.0 V) powered by two ASDs connected in series.

Table 3.4: Energy and power densities of some PANI based materials and other comparable supercapacitor materials.

Active materials (Positive // negative material)	**Energy density (Wh kg^{-1})**	**Power density (W kg^{-1})**	**Ref.**
PANI nf/rGO/CeO_2//rGO	46.3	850	**This work**
rGO-RuO_2//rGO PANI	20.1	1050	[26]
Ti_2CT_x/PANI//rGO	43.5	950	[31]
CFP/PPy//rGO/MWCNT	28.6	395	[156]
PANI//V_2O_5	26.7	220	[154]
$NiCO_2O_4$/C//C	53.1	900	[157]
MnO_2/G//PANI/G	41	787.3	[158]
PANI/N doped C // N doped C	60.3	900	[159]
$MnMoO_4 \cdot H_2O/MnO_2$ //AC	45.6	507	[160]
MnO_2/CNF//AC	35.1	497.3	[161]
PANI/MnO_2//rGO	19	2500	[129]
Sulf. PANI/rGO//rGO	31.4	992.78	[162]
GF/CNT/MnO_2//GF/CNT/PPy	22.8	860	[93]

The excellent supercapacitor properties of the 3D hierarchical microspheres could be attributed to the design of the ternary structure and synergistic effect of the

three active components. The addition of rGO greatly enhances the electrical conductivity. The addition of the third component -CNR, brings various advantages to the ternary structure. First, CNR is pseudocapacitive and provides significant charge storage. Second, addition CNRs could prevent the restacking of rGO sheets. These factors together enable higher accessible area for charge storage, improved conductivity, and enhanced cyclic performance. The combination of CNRs and rGO also could alleviate structural damage to the PANI structure during repeated cycling. The 3D network of PANI and rGO could also mitigate the aggregation of CNRs. The high surface area and the 3D structure of the hierarchical structure with a good distribution of meso and macropores not only provide pathways for the electrolyte ions to reach interior regions of the structure, but also ensures a constant supply of electrolyte ions. This could accelerate the ion transport between the active material and electrolyte leading to maximum charge storage.[128, 155] Thus, the synergic effect between PANI, rGO, and CNR yields a high-performance supercapacitor active material. Additionally, the simple synthesis methods can be easily scaled-up for industry-scale production.

3.4 Conclusions

A template-free, ternary hierarchical microstructure composed of PANI, rGO, and CNR was synthesized using a simple spray drying method for supercapacitor application. Spray drying allows for bulk production of hierarchical structures in very short processing times and low cost. The unique structure and high surface area of the hierarchical microstructure exhibit various advantages for charge storage application. The interconnected porous structure ensures a constant supply of electrolyte ions for

maximum charge storage utilization by the active materials. The 3D network of PANI acts as a conductive network and also prevents the aggregation of CNRs. rGO significantly improves the overall conductivity of the active material. CNRs also effectively prevent the restacking of the rGO sheets. The optimized ternary composite (PR_9C_1) shows a high specific capacitance (684 Fg^{-1}), good rate performance and excellent cyclability (~91% capacitance retention after 6000 cycles). An asymmetric supercapacitor device assembled using the optimized ternary composite and rGO exhibited a high energy density (46.27 W h kg^{-1}) and high power density (11730 W kg^{-1}). Thus, we demonstrate a simple, yet highly effective method that can be easily scaled up to industrial-scale to produce ternary hierarchical structures as a high-performance active material for supercapacitor applications. This method can be further extended to produce other highly scalable multi-component hierarchical structures for other energy storage applications.

CHAPTER 4:NANOCERIA GRAPHENE COMPOSITE AEROGELS FOR HIGH PERFORMANCE SUPERCAPACITORS

4.1 Introduction

Single layer graphene sheets exhibit outstanding electrochemical charge storage properties due to their high electrical conductivity, large surface area, and high mechanical strength.[163, 164] However, several issues that prevent them from being used to assemble a practical energy storage device. These include high cost, need for harsh chemicals and scalability issues. Furthermore, the strong pi-pi interactions and the van der Waals force between the adjacent layers leads to attraction and restacking. The reduction in available surface area due to restacked/aggregated graphene sheets produces subpar electrochemical charge storage performance.[99, 165]

Assembly of the graphene sheets into an interconnected 3D hierarchical structure through a 'bottom-up' approach is a promising strategy to overcome the issue of aggregation.[165-167] 3D hierarchical structures have known to exhibit properties much different from their bulk forms and their building blocks. As a result of the open structure, the graphene 3D network has various advantages for charge storage such as increased mass transport, lowered aggregation and decreased diffusion distances.[168]

Aerogels are one of the most popular forms of 3D hierarchical graphene structures, apart from hydrogels and organogels. Aerogels are usually synthesized by freeze-drying or supercritical drying of the hydrogels or organogels. Graphene Oxide (GO) is usually preferred for the preparation of graphene hydrogels, as their hydrophilic nature offer ease of processing. During the hydrothermal self-assembly process, the

GO is partially reduced (rGO). The interactions between the basal planes and the functional groups aid the assembly of the hydrogel.[166, 167] The residual functional groups in rGO also contribute towards redox type charge storage. The electrochemical charge storage properties of the rGO aerogels can be further improved by decoration with metal oxide nanoparticles. Though metal oxide nanoparticles generally possess high pseudocapacitance, when used separately, they suffer from drawbacks such as aggregation, poor conductivity, etc. The synergistic effect of the hybrid metal oxide decorated rGO aerogel structure poses multiple advantages such as larger electrochemical surface area, lower aggregation and better cyclic performance.[169-173]

In this study, we report rGO- nano CeO_2 composite aerogel (rC aerogel), a novel nano CeO_2 particle supported on a 3D rGO aerogel structure. The hybrid aerogel exhibits a macroporous interconnected structure of rGO sheets with a uniform distribution of nano CeO_2. Electrochemical testing reveals that the hybrid rC aerogels exhibit a high specific capacitance of (503 F g^{-1}), excellent rate performance and stable cycle life (only ~94% capacitance retention after 10000 cycles).

4.2 Experimental Section

First, 4 mg/ml aqueous GO suspension (Graphenea Inc), 0.045 M $Ce(NO_3)_3 \cdot 6H_2O$ and 1M NaOH are thoroughly mixed with a probe sonicator for 15 mins. This mixture is then transferred to a Teflon-lined stainless-steel autoclave to ~85% volume capacity, sealed and held in an electric oven 180 °C for 48 h to yield hydrogels. The gels are washed thoroughly with copious DI H_2O to remove any residual impurities. The washed composite gel is frozen at -70 °C for 6h and lyophilized overnight to yield

rC composite aerogels. rGO aerogels are synthesized similarly without the addition $Ce(NO_3)_3 \cdot 6H_2O$ and NaOH.

4.3 Results and discussion

4.3.1 Materials Characterization

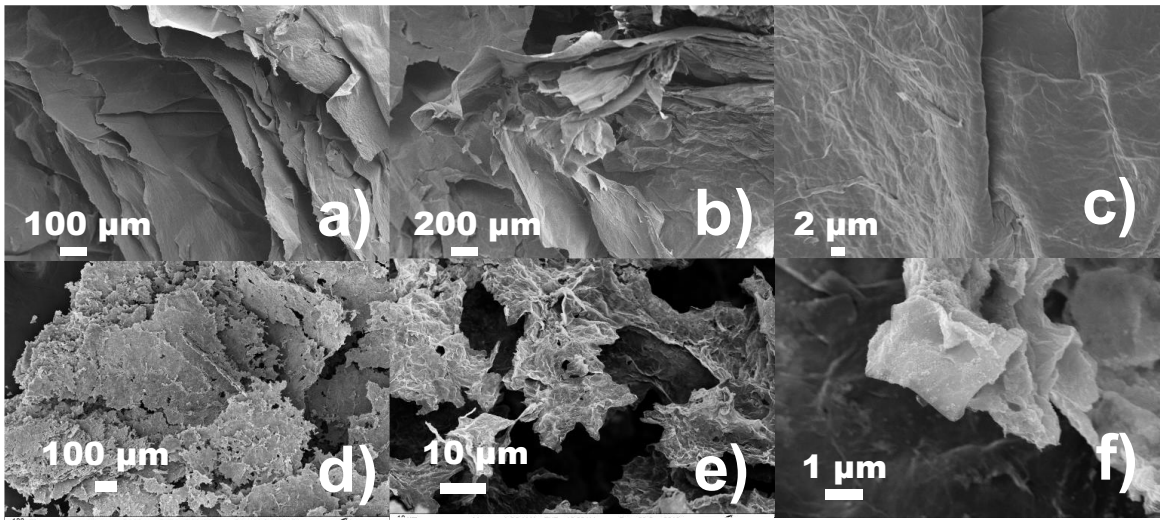

Figure 4.1: Representative SEM images of rGO aerogels (a-c) and hybrid rC aerogels (d-f). Hybrid rC aerogels show nano CeO_2 deposits and a highly porous structure.

The SEM images show the interconnected sheet-like structure of rGO and hybrid rC aerogels (Figure 4.1 a-f). The SEM images of rGO aerogels show clear rGO sheets with mild wrinkles (Figure 4.1 c). However, they rGO sheets itself do not exhibit any pores. The hybrid rC aerogels (Figure 4.1 d-f) show clear deposits of nano CeO2. Compared to rGO aerogels, the individual rGO sheets in the hybrid material exhibit a very porous structure, which could be attributed to the activation by NaOH.174 The porous structure could be highly beneficial for the electrochemical performance, as these pores can act as pathways for the transport of electrolyte ions. The highly porous

nature also enables higher exposure of the active material. Figure 4.2 shows the elemental maps of the hybrid rC aerogel. The elemental maps reveal the presence of C, Ce and O. These images confirm the uniform distribution of nano CeO_2 over the porous rGO layers.

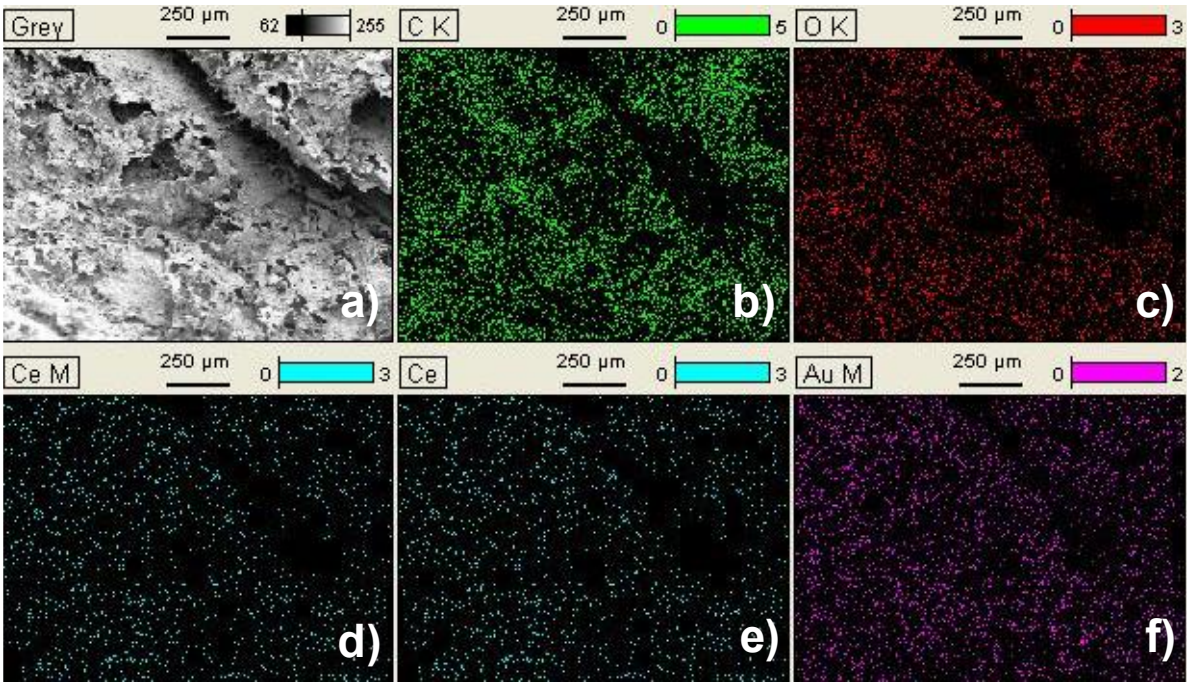

Figure 4.2: Elemental mapping images of the hybrid rC aerogel. a) SEM image of rC aerogel. (b-e) C,O, and Ce EDX maps in a typical rC aerogel. EDX analysis reveal an even distribution of nano CeO_2 over the rGO sheets.

Figure 4.3 a shows the XRD pattern of nano CeO_2, rGO, and the rC composite aerogels. The diffraction peaks of nano CeO_2 can be indexed as (111), (200), (220), (311), (222), (400), (331), and (420) planes of CeO_2, corresponding to the pure cubic fluorite phase of CeO_2 (JCPDS 34e0394, space group Fm-3m). The rGO aerogel exhibit

a peak at 2θ = 12.8° that is indicative of a layered GO layer and decent crystallinity. This corresponds to an interlayer spacing of 0.691 nm. The broad peak at 2θ = 23.5° corresponds to the graphene sheets aligned along the (002) direction. The occurrence of well-defined CeO_2 peaks suggests the incorporation of nano CeO_2 in the hybrid rC aerogel.

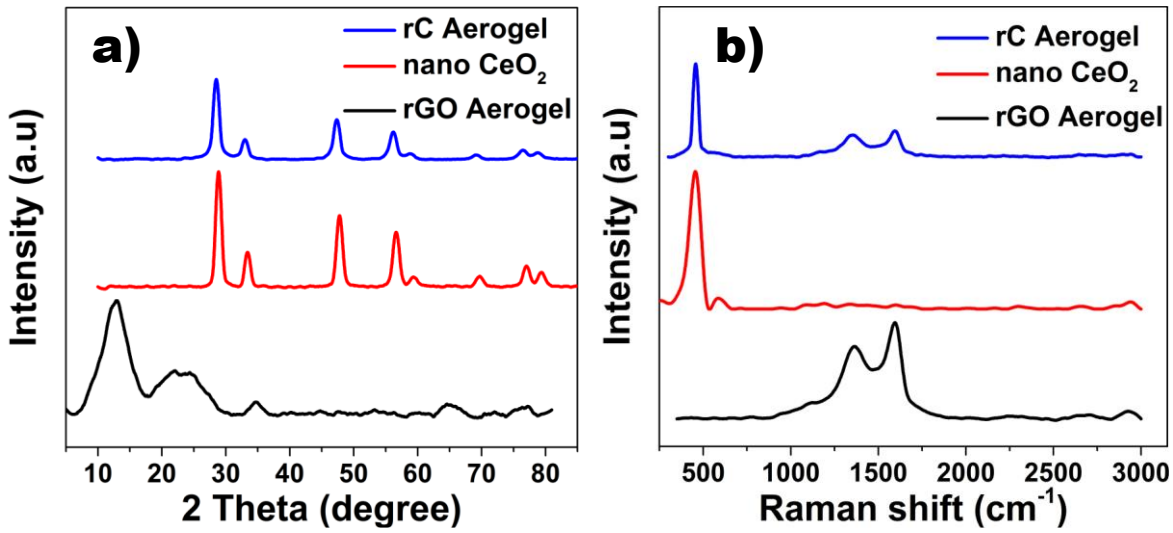

Figure 4.3: Structural and chemical analysis of aerogels. a) XRD pattern and (b) Raman spectra of nano CeO_2, rGO aerogel, and hybrid rC aerogel.

The Raman spectra of the three structures are shown in Figure 4.3 b. In nano CeO2, the raman peak at 455 cm-1 is associated with the F2g Raman active mode of the fluorite structure. A weak peak at 586 cm-1 is attributed to the surface defects. Raman spectra of rGO show peaks at 1351 cm-1 and 1602 cm-1, corresponding to the D band and G band. A weak peak at 2696 cm-1 corresponds to the 2D band. The hybrid aerogels exhibit features of rGO and nano CeO2. The ID/IG ratios for the rGO

and rC hybrid aerogels are 0.81 and 0.87, respectively. This clearly suggests that the hybrid aerogels exhibit slightly higher defects than the rGO aerogels.

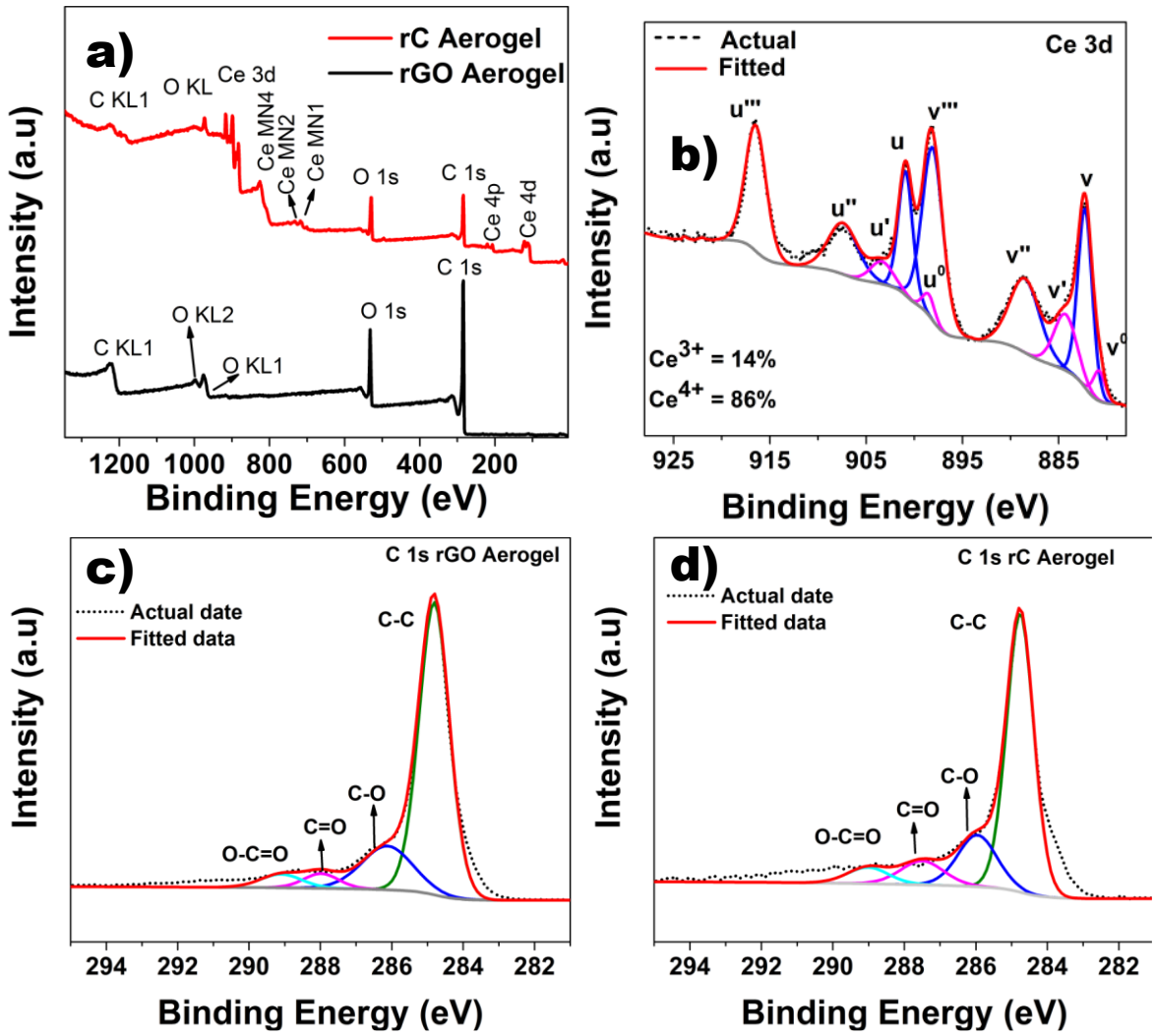

Figure 4.4: XPS surface analysis of rGO and hybrid rC aerogels. a) Survey spectra b) Ce 3d spectra of rC aerogels. C 1s spectra of rGO aerogel (c) and hybrid rC aerogels (d). Nano CeO_2 in the hybrid aerogel is present in a mixed oxidation state (+3 and +4).

The survey spectra of rGO and rC aerogels are shown in **Figure 4.4 a**. Neat rGO aerogels show only C and O peaks. Apart from C and O peaks, hybrid rC aerogels also

exhibit Ce peaks, which clearly suggests the presence of nano CeO_2. Furthermore, the high-resolution 3d spectra of rC composite aerogel (**Figure 4.4 b**) reveal nano CeO_2 is present in a mixed oxidation state (+3 and +4).[175] After deconvolution, the four peaks associated with Ce^{3+} are marked as $u^0+u'+v^0+v'$, and the six peaks Ce^{4+} peaks are marked as $u+u''+u'''+v+v''+v'''$. The amount Ce^{3+} and Ce^{4+} is estimated as 14% and 86%, respectively. **Figure 4.4 c** and **d** show the C1s spectrum of rGO and the hybrid rC composite aerogels, which can be deconvoluted to 4 peaks at 284.6, 286.6, 288, and 289.2 eV. The 284.6 eV peak corresponds to the sp^2 carbon. The minor peaks 286.6, 288, and 289.2 eV are assigned to C-O, C=O, and O-C=O residual functional groups.[176, 177] It is clear that the intensity of peaks that corresponds to the oxygen containing functional groups in the rC aerogels is much reduced than in the rGO aerogels. This could be due to the nucleation growth/attachment of nano CeO_2 on functional groups.[170, 172]

4.3.2 Electrochemical characterization

The electrochemical properties of the rGO aerogel, nano CeO_2, and rC composite aerogel electrodes were first evaluated by cyclic voltammetry in a three-electrode configuration with $1MH_2SO_4$ electrolyte between 0 V and 1.0 V at various scan rates from 5 to 100 mV s^{-1}. **Figure 4.5** shows the CVs of the rGO aerogel, nano CeO_2, and rC composite aerogel electrodes. The CVs exhibit a pseudo-rectangular shape with mild redox peaks suggesting both EDLC and redox type charge storage.

The redox peaks in rGO is associated with the redox active residual functional groups in rGO and the redox reactions in nano CeO_2, as shown in **Equation 2.1**. From

the area enclosed by the CVs in **Figure 4.5 d** it can be understood that SC of hybrid rC aerogel > rGO aerogel > nano CeO_2. The GCD show a symmetric shape, which is a characteristic of rGO based material. The specific capacitance is then estimated using **Equation 2.4**. The SC of hybrid rC aerogel, rGO aerogel, nano CeO_2 was 503 F g^{-1}, 477 F g^{-1}, and 241 F g^{1}, respectively at 1 A g^{-1}. The superior charge storage properties of hybrid aerogels can be attributed to the synergistic effect of open structure and redox type charge storage contribution by nano CeO_2.

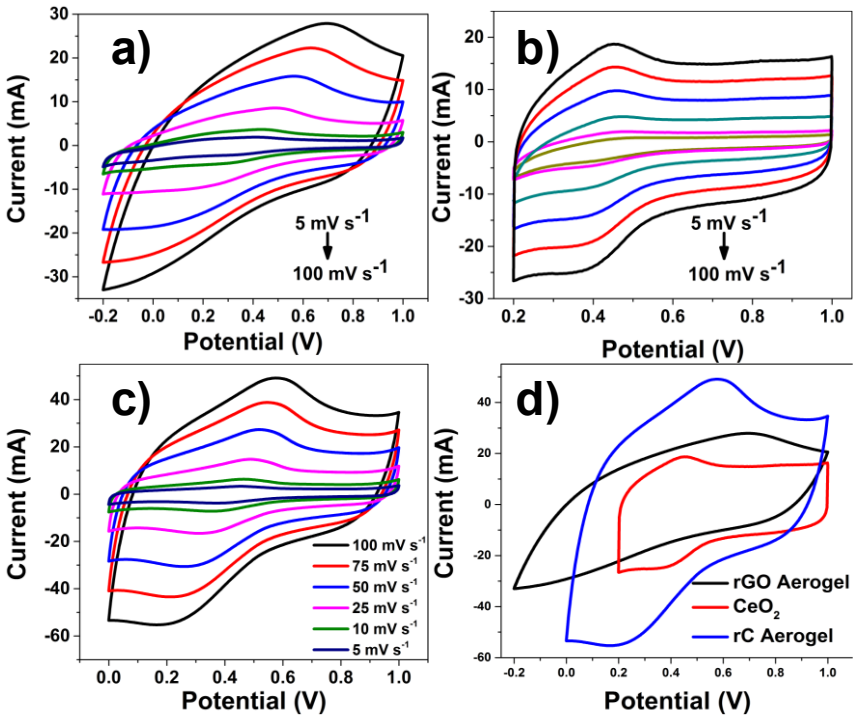

Figure 4.5: Cyclic voltammetry of rGO aerogel, nano CeO_2 and rC composite aerogel tested in 1M H_2SO_4. CVs of rGO aerogel (a), nano CeO_2 (b) and rC composite (c) cycled at different sweep rates. (d) CVs of rGO aerogel, nano CeO_2 and rC composite aerogel at 100 mV s^{-1}.

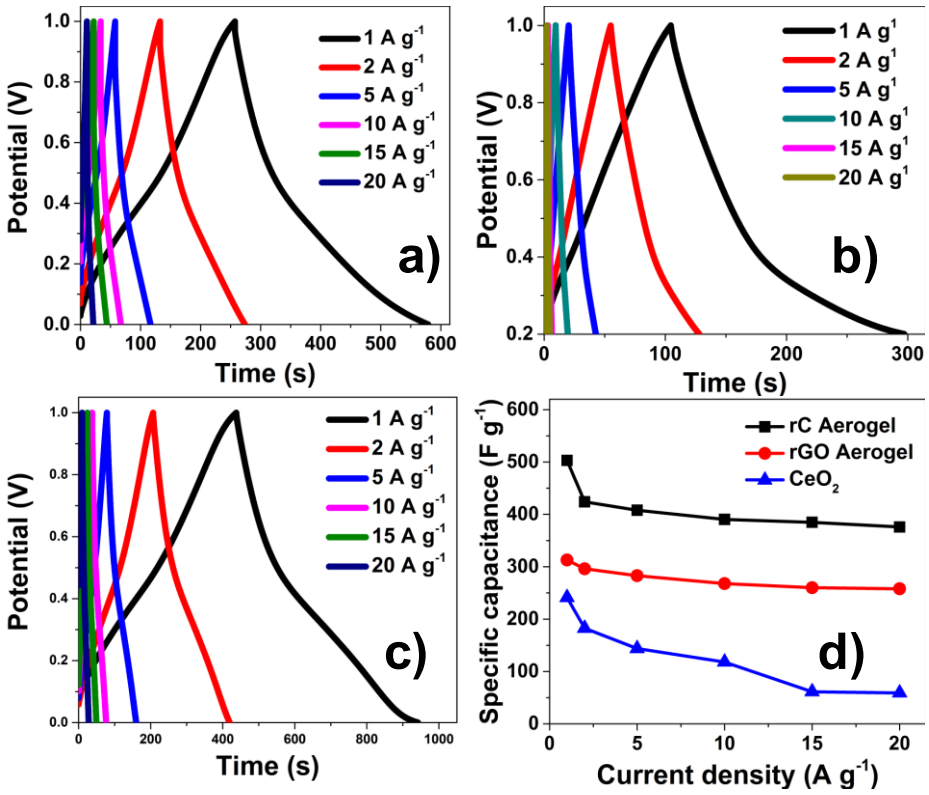

Figure 4.6: GCD curves of of rGO aerogel (a), nano CeO_2 (b) and rC composite aerogel (c). Specific capacitance of rGO aerogel, nano CeO_2 and rC composite plotted as a function of current density.

The change in SC with current density is shown in **Figure 4.6d**. The SC of all three materials monotonously increases with a decrease in current density. The SC of rGO does not significantly reduce at higher current densities. This could be attributed to the fast EDLC mechanism in rGO. However, nano CeO_2 exhibits a significant drop in SC at higher current densities. This could be attributed to higher electrolyte diffusion resistance into the electrode at higher current densities. The high SC and the excellent rate performance of the rC composite aerogel could be attributed to the combinational effect of rGO and nano CeO_2 on charge storage and the higher available surface area.

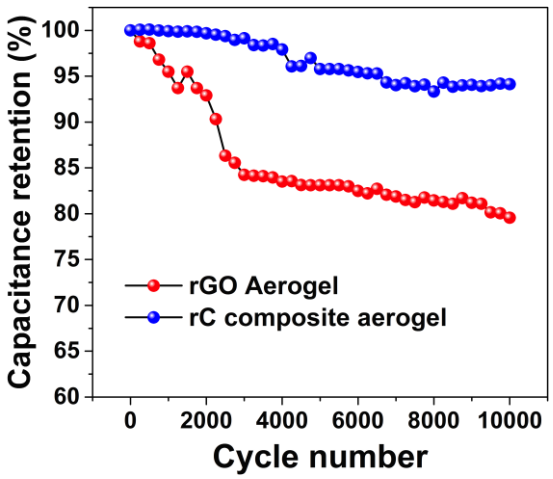

Figure 4.7: Cyclic stability of rGO aerogel and rC composite aerogel at 10 A g^{-1}. Nano CeO_2 in the composite aerogels successfully prevents the restacking of rGO sheets and improves cyclic performance.

Long term cycle life is a crucial performance indicator of any energy storage device. The cyclic stability of the composite aerogel electrodes evaluated repeated GCD cycling 0 - 1.0 V at a current density of 10 A g^{-1}. From **Figure 4.7** it is clear that the capacitance retention of the rGO aerogels reaches ~ 83% after the first 4000 cycles and remains stable after that. After 10,000 cycles, rGO aerogels exhibit a capacitance retention of ~ 79%. The initial capacity fade is attributed to two factors: restacking of the graphene sheets and the presence of residual function groups. rGO layers tend to restack during repeated cycling, which eventually leads to lower exposed area for EDLC type storage. The residual functional groups on rGO are not stable enough for repeated long term cyclability. However, they are redox active and contribute significantly to pseudocapacitive type storage. [178, 179]Thus, it is necessary to find a balance of specific capacitance and cyclic stability. The composite aerogels deliver a stable cyclic

performance and exhibit 94% capacitance retention after 10,000 cycles. Nano CeO_2 in the composite aerogels can act as mechanical spacers between the rGO layers and can successfully prevent their restacking.

4.3.3 Kinetics of charge storage

As stated previously, the stored charge has two components: the faradaic contribution from the rapid redox reactions and the nonfaradaic EDLC portion. Both, the EDLC and faradaic contributions could be high due to the high surface area of the composite aerogel material. The contributions from the individual components have been analyzed from cyclic voltammetry data using the following power law equation:

$$i = av^b \tag{4.1}$$

where the current (*i*) has a power law dependence on the sweep rate (v). a and b are fitting parameters. **Equation 4.1** can be re-written in log form as follows:

$$\log i = b \log v + a \tag{4.2}$$

Thus, the constants *b* and *a* can be estimated from the slope and the intercept of the *log i vs log* v plot, respectively. There are two well-stated condition for *b*: *b*=1 and *b*=0.5. The condition, *b*=1 is representative of a pure capacitive type response that does not exhibit any diffusion limitation.[180, 181] Here, the current *i* has a linear relationship with sweep rate v, which can be represented as follows:

$$i = ACv \tag{4.3}$$

where *C* is the capacitance and *A* is the electrode surface area. The other condition, *b*=0.5 is indicative of a diffusion limited faradaic intercalation process. The

current response in this case has a square root dependence on sweep rate. In this case, the peak current can be represented by the following Randles-Sevcik eqation:

$$i_p = 0.446nFAC_eD_e^{1/2}\left(\frac{nF}{RT}\right)^{1/2}\nu^{1/2} \quad (4.4)$$

where i_p is the peak current, n is the number of electrons in the redox process, F is the Faraday's constant, A is the electrode surface area, C_e is the concentration of the electrolyte, D_e is the diffusion coefficient of the species e, R is the ideal gas constant, T is the temperature, and ν sweep rate. The b-values are in the range 0.7-0.85, indicating the material has a primary capacitive response.

Following the discussion on b-values, it is highly desirable to quantitatively estimate the contributions from the capacitive and diffusion controlled processes. This could also be estimated from the cyclic voltammetry data. Here, the response current i is representative of two components: a capacitive type process, where the response current varies linearly with sweep rate and a semi-infinite linear diffusion type process, where the current varies linearly with squareroot of sweep rate $\nu^{1/2}$.[182] This is can be represented as follows:

$$i(V) = k_1\nu + k_2\nu^{1/2} \quad (4.5)$$

where k_1 and k_2 correspond to constants related to the current response from the capacitive and diffusion effects, respectively. for convenience, this equation can be rearranged as:

$$\frac{i(V)}{\nu^{1/2}} = k_1\nu^{1/2} + k_2 \quad (4.6)$$

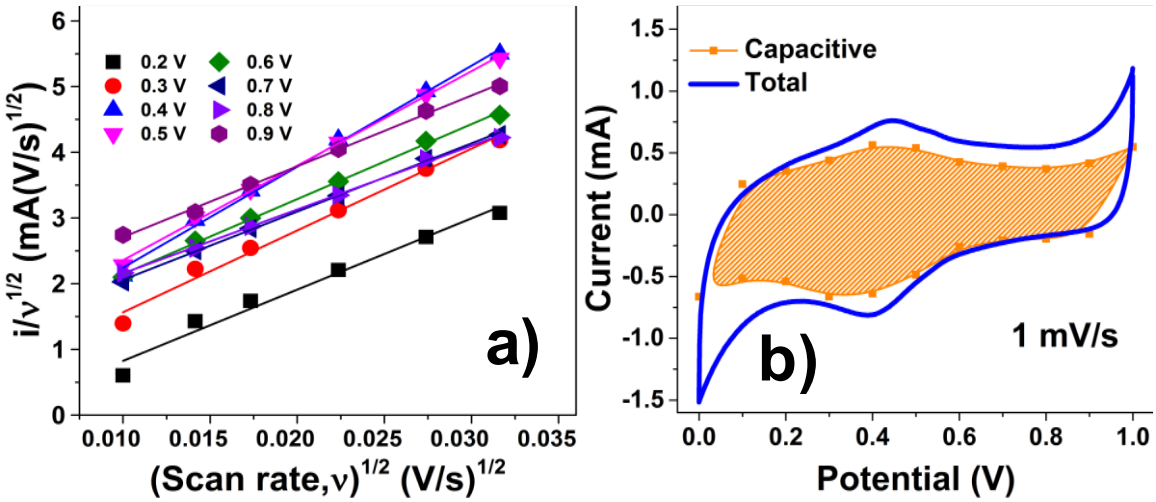

Figure 4.8: Separation of diffusion and capacitive contributions in CeO_2-rGO composite aerogel. a) Typical plots of anodic currents i(V) $\nu^{-1/2}$ vs $\nu^{1/2}$ for k_1 and k_2 estimation. b) Map of capacitive contributions (shaded region) at 1 mV s^{-1}.

By plotting the current response as function of sweep rate according equation (4.6), the constants k_1 and k_2 can be estimated from the slope and the Y-incept, respectively.[180, 183] **Figure 4.8a** shows the plot of the anodic current response as function of sweep rates for different potentials from which the k_1 and k_2 are estimated. Similarly, k_1 and k_2 are also estimated for the cathodic currents. From these k_1 values, the capacitive contributions in the cyclic voltammetry curves for a specific sweep rate can be mapped by plotting the response current for different potentials according to:

$$i(V) = k_1 v \tag{4.7}$$

Figure 4.8b shows a CV of the composite aerogel material at 1 mV s^{-1}. The shaded region shows the capacitive current contributions and the non-shaded region shows the diffusion dominated current response. A slower sweep rate is chosen to demonstrate the capacitive contributions as the diffusion contributions are much

higher. This is clear from the anodic and cathodic peak at 0.45 V and 0.4 V. However, the capacitive response does not exhibit prominent peaks, suggesting the only minor diffusion type processes.

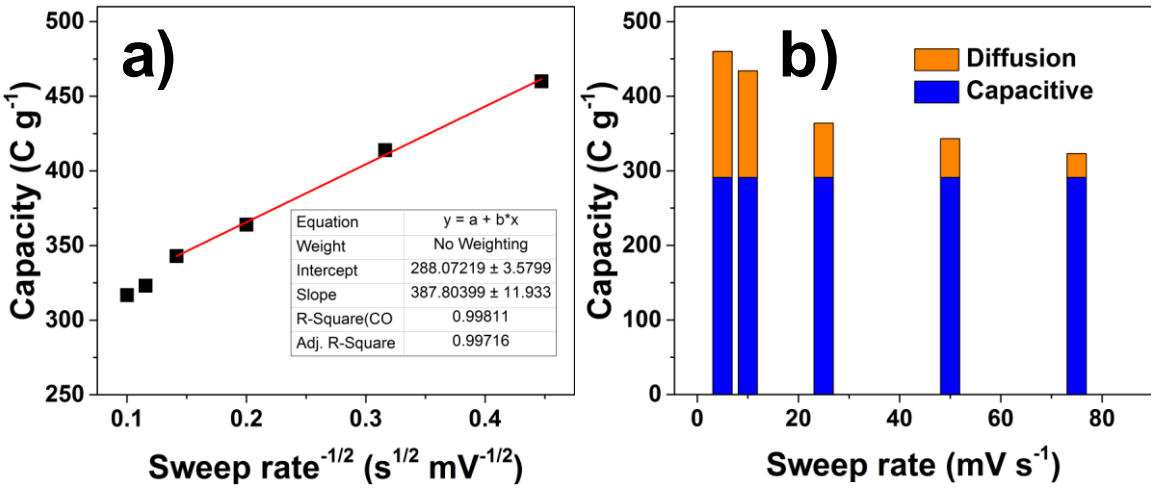

Figure 4.9: Infinite sweep rate capacity determination of CeO_2-rGO composite aerogel: a) Typical plot of capacity as function of $\nu^{-1/2}$. The surface capacitive contribution at infinite sweep rate (Y-intercept) is estimated as 291 C g^{-1}. b) Ratios of capacitive and diffusion type charge storage for different sweep rates. Diffusion contributions to charge storage are much higher at lower sweep rates.

The charge capacity contributions from the capacitive and diffusion controlled processes can also be quantitatively estimated though a method proposed by Trasatti et al.[184] Here, the total charge capacity is assumed to be composed of two components: a surface dominated capacitive component Q_s and inner or bulk charge storage component Q_b. This can be expressed as:

$$Q = Q_s + Q_b \tag{4.8}$$

The bulk charge storage component Q_b is dependent on the diffusion time of the electrolyte species. For semi-infinite linear diffusion, Q_b has a square root dependence on time. As sweep rate is inversely related to time, **equation 3.8** can then be rewritten in terms of sweep rate as:

$$Q(\nu) = Q_s + k\left(\nu^{-1/2}\right) \tag{4.9}$$

The diffusion contributions are maximum for infinite time ($\nu \rightarrow 0$) and minimum for very short times ($\nu \rightarrow \infty$). Thus, it is clear the clear that the y-intercept of **equation 4.9** yields the surface contributions Q_s ($\nu \rightarrow \infty$). Due to polarization effects, the capacity values at high sweep rates tend to deviate away from the linear trend.[185] Thus, capacities in the medium sweep rate are chosen to extrapolate the capacitive contribution. **Figure 4.9 a** and **b** shows the surface and bulk contributions of the composite aerogel estimated through Trasatti's method. By extrapolation, the surface capacity at infinite sweep rate is estimated to be around 291 C g^{-1}. This arises purely from surface oriented EDLC type process. From **Figure 4.9 b**, it is clear that diffusion type charge storage is very minimal at higher sweep rates. However, the ratio of the diffusion contributions significantly increases at slower sweep rates. The diffusion contributed charge storage is only 9.8 % at sweep rate of 75 mV s^{-1} and increases up to 36.5 % at sweep rate of 5 mV s^{-1}.

4.4 Conclusions

In summary, hybrid rGO aerogels decorated with nano CeO_2 can be successfully synthesized using a one-pot synthesis. The hybrid rC aerogels exhibit a high specific capacitance of 503 F g^{-1}, excellent rate performance and stable cycle life (only ~6%

capacitance fade after 10,000 cycles). The superior electrochemical performance is attributed to the synergistic effect of the high conductive rGO layers in the aerogel network and an even distribution of nano CeO_2. The microporous nature and the 3D network of the aerogel allows for maximum electrolyte-electrode contact and minimizes the diffusion distance. Furthermore, addition of nano CeO_2 not only contributes to charge storage but also prevents restacking of the rGO sheets, which significantly improves the high-rate performance and cycle life of the rC composite aerogels. Besides supercapacitor applications, nano CeO_2 decorated rGO aerogels could be used for other applications such as sensors, catalysts and environmental applications.

CHAPTER 5:CONCLUSIONS

In this work, nano CeO_2 is thoroughly examined as an active material for electrochemical capacitor applications. The surface area of the nanostructure is generally used as a major descriptor for charge storage capacity. However, electrochemical and MD studies reveal morphology of the nanostructure and the exposed crystal planes as more important factors that determine the charge storage capacity and the rate performance of nano CeO_2. Electrochemical studies on three popular CeO_2 nanostructures show that specific capacitance of nanorods >> nanocubes > nanoparticles. The highest charge storage in nanorods is ascribed to the exposure of high energy crystal facets ({110} and {100}) and high surface area. Nanocubes and nanoparticles exhibit a comparable surface area. However, the exposure of high energy {100} planes in nanocubes, offer them better electrochemical properties than nanoparticles, which primarily expose the low energy {111} planes.

In the next chapter, nano CeO_2 and rGO are used as additives to enhance the poor cyclic performance of a conductive polymer (polyaniline). Herein, a ternary hierarchical microsphere composed of CeO_2 nanorods, polyaniline nanofibers, and rGO is obtained through a simple and industry-scalable spray-drying technique. The optimized ternary compound displayed a 3D hierarchical structure and a high surface area (418 $m^2\ g^{-1}$), which is highly beneficial for charge storage. Electrochemical studies reveal that the ternary compound exhibit a high specific capacity (~710 F g^{-1}), good rate performance and excellent cycle life (~90% capacitance retention after 5000 cycles). An asymmetric device fabricated using this material and rGO exhibited a high energy

density (~47 Wh Kg^{-1}) at a power density of 850 W kg^{-1}, which is much higher than other conductive-polymer based supercapacitor materials. The excellent electrochemical performance of the spray-dried microspheres was attributed to the unique architecture and synergistic effect of the three components. Moreover, this technique could be extended to massproduce hierarchical structures for other energy storage applications.

In the last part of this work, nano CeO_2 is demonstrated as an effective active spacer in rGO aerogels. The high electrical conductivity and large surface area of rGO make them an attractive EDLC type supercapacitor material. However, the strong pi-pi interactions and van der Waals force between the 2D layers lead to irreversible aggregation/restacking, which results in a decrease in the available electroactive surface area and charge storage capacity. 3D assembly of the rGO layers with an open/porous structure and an interconnected network of 2D layers can effectively combat the restacking. The advantages of the 3D structure can significantly improve the cyclability and rate performance. However, the specific capacity is still low as charge storage is primarily limited to just an EDLC type mechanism. The addition of nano CeO_2 leads to a multidimensional improvement in charge storage performance. Nano CeO_2 significantly improves the charge storage capacity due to its pseudocapacitive contributions. Moreover, the uniformly distributed nano CeO_2 over the rGO sheets also act as spacers that can further suppress restacking. The conductive nature of the rGO network can offset the poor conductivity of nano CeO_2. Therefore, the synergistic effect of the hybrid nano CeO_2-rGO aerogels results in a high specific capacitance of 503 F g^{-}

[1], excellent rate performance and stable cycle life (only ~6% capacitance fade after 10,000 cycles).

Overall, nano CeO_2 appears to be a promising active material for supercapacitor applications. Though the electrochemical properties of nano CeO_2 are highly dependent on various factors such as morphology, exposed crystal planes, surface area, and electrolyte, we demonstrate that effective nanoengineering could result in electrochemical properties compared to the state-of-the-art supercapacitor materials. The major advantage of nano CeO_2 is that it can be used as a standalone material and additive that could considerably enhance the performance of other supercapacitor materials. Successful implementation of nano CeO_2 as a supercapacitor material could lead to more sustainable energy infrastructure through the development low cost EEDs with higher power, energy density and improved safety.

APPENDIX A: COPYRIGHT PERMISSION LETTER FOR FIGURE 1.2

Copyright Clearance Center | RightsLink®

Home | Help | Email Support | Aadithya Jeyaranjan

SPRINGER NATURE

Materials for electrochemical capacitors

Author: Patrice Simon et al
Publication: Nature Materials
Publisher: Springer Nature
Date: Dec 31, 1969

Order Completed

Thank you for your order.

This Agreement between University of Central Florida -- Aadithya Jeyaranjan ("You") and Springer Nature ("Springer Nature") consists of your license details and the terms and conditions provided by Springer Nature and Copyright Clearance Center.

Your confirmation email will contain your order number for future reference.

Printable Details

License Number	4806691173579
License date	Apr 12, 2020

Licensed Content

Licensed Content Publisher	Springer Nature
Licensed Content Publication	Nature Materials
Licensed Content Title	Materials for electrochemical capacitors
Licensed Content Author	Patrice Simon et al
Licensed Content Date	Dec 31, 1969

Order Details

Type of Use	Thesis/Dissertation
Requestor type	academic/university or research institute
Format	print and electronic
Portion	figures/tables/illustrations
Number of figures/tables/illustrations	1
Will you be translating?	no
Circulation/distribution	1 - 29
Author of this Springer Nature content	no

About Your Work

Title	CERIUM OXIDE BASED NANOCOMPOSITES FOR SUPERCAPACITORS
Institution name	University of Central Florida
Expected presentation date	Apr 2020

Additional Data

Portions	Figures 1

Requestor Location

Requestor Location	University of Central Florida 12760 Pegasus Dr, ENG I, Suite 207 ORLANDO, FL 32816 United States Attn: University of Central Florida

Tax Details

APPENDIX B: COPYRIGHT PERMISSION LETTER FOR FIGURE 1.4

APPENDIX C: COPYRIGHT PERMISSION LETTER FOR FIGURE 1.6

Order Details

1. Energy & environmental science

Billing Status: Open

Print License

Order license ID	1028088-1	Type of use	Republish in a thesis/dissert...
Order detail status	Completed	Publisher	RSC Publishing
ISSN	1754-5706	Portion	Chart/graph/table/figure
			0.00 USD
Hide Details			Republication Permission

LICENSED CONTENT

Publication Title	Energy & environmental scie...	Country	United Kingdom of Great Bri...
Author/Editor	Royal Society of Chemistry (...	Rightsholder	Royal Society of Chemistry
Date	01/01/2008	Publication Type	e-journal
Language	English	URL	http://www.rsc.org/Publishi...

REQUEST DETAILS

Portion Type	Chart/graph/table/figure	Distribution	Worldwide
Number of charts / graphs / tables / figures requested	1	Translation	Original language of publica...
		Copies for the disabled?	No
Format (select all that apply)	Print,Electronic	Minor editing privileges?	Yes
Who will republish the content?	Academic institution	Incidental promotional use?	No
		Currency	USD
Duration of Use	Life of current edition		
Lifetime Unit Quantity	Up to 499		
Rights Requested	Main product		

NEW WORK DETAILS

Title	CERIUM OXIDE BASED NAN...	Institution name	University of Central Florida
Instructor name	Sudipta Seal	Expected presentation date	2020-05-02

ADDITIONAL DETAILS

The requesting person / organization to appear on the license	Aadithya Jeyaranjan

REUSE CONTENT DETAILS

Title, description or numeric reference of the portion(s)	Fig. 3	Title of the article/chapter the portion is from	Types of pseudocapacitive ...
Editor of portion(s)	N/A	Author of portion(s)	Royal Society of Chemistry (...
Volume of serial or monograph	N/A	Publication date of portion	2013-03-13
Page or page range of portion	1600		

Total Items: 1

Subtotal: 0.00 USD

Order Total: 0.00 USD

Back To Orders

APPENDIX D: COPYRIGHT PERMISSION LETTER FOR FIGURE 1.7,11.8,1.9

Copyright Clearance Center | RightsLink®

Home | Help | Email Support | Aadithya Jeyaranjan

Engineering electrochemical capacitor applications

Author: John R. Miller
Publication: Journal of Power Sources
Publisher: Elsevier
Date: 15 September 2016

Order Completed

Thank you for your order.

This Agreement between University of Central Florida -- Aadithya Jeyaranjan ("You") and Elsevier ("Elsevier") consists of your license details and the terms and conditions provided by Elsevier and Copyright Clearance Center.

Your confirmation email will contain your order number for future reference.

Printable Details

License Number	4806710603528
License date	Apr 12, 2020

Licensed Content

Licensed Content Publisher	Elsevier
Licensed Content Publication	Journal of Power Sources
Licensed Content Title	Engineering electrochemical capacitor applications
Licensed Content Author	John R. Miller
Licensed Content Date	Sep 15, 2016
Licensed Content Volume	326
Licensed Content Issue	n/a
Licensed Content Pages	10
Journal Type	S&T

Order Details

Type of Use	reuse in a thesis/dissertation
Portion	figures/tables/illustrations
Number of figures/tables/illustrations	3
Format	both print and electronic
Are you the author of this Elsevier article?	No
Will you be translating?	No

About Your Work

Title	CERIUM OXIDE BASED NANOCOMPOSITES FOR SUPERCAPACITORS
Institution name	University of Central Florida
Expected presentation date	Apr 2020

Additional Data

Portions	Fig. 1, Fig 2, Fig. 3

Requestor Location

Requestor Location	University of Central Florida 12760 Pegasus Dr, ENG I, Suite 207 ORLANDO, FL 32816 United States Attn: University of Central Florida

Tax Details

Publisher Tax ID	98-0397604

$ Price

APPENDIX E: COPYRIGHT PERMISSION LETTER FOR FIGURE 1.10

Copyright Clearance Center | RightsLink®

Home | Help | Email Support | Aadithya Jeyaranjan

Review on supercapacitors: Technologies and materials

Author: Ander González,Eider Goikolea,Jon Andoni Barrena,Roman Mysyk
Publication: Renewable and Sustainable Energy Reviews
Publisher: Elsevier
Date: May 2016

Order Completed

Thank you for your order.

This Agreement between University of Central Florida -- Aadithya Jeyaranjan ("You") and Elsevier ("Elsevier") consists of your license details and the terms and conditions provided by Elsevier and Copyright Clearance Center.

Your confirmation email will contain your order number for future reference.

Printable Details

License Number	4806721436465
License date	Apr 12, 2020

Licensed Content

Licensed Content Publisher	Elsevier
Licensed Content Publication	Renewable and Sustainable Energy Reviews
Licensed Content Title	Review on supercapacitors: Technologies and materials
Licensed Content Author	Ander González,Eider Goikolea,Jon Andoni Barrena,Roman Mysyk
Licensed Content Date	May 1, 2016
Licensed Content Volume	58
Licensed Content Issue	n/a
Licensed Content Pages	18
Journal Type	S&T

Order Details

Type of Use	reuse in a thesis/dissertation
Portion	figures/tables/illustrations
Number of figures/tables/illustrations	1
Format	both print and electronic
Are you the author of this Elsevier article?	No
Will you be translating?	No

About Your Work

Title	CERIUM OXIDE BASED NANOCOMPOSITES FOR SUPERCAPACITORS
Institution name	University of Central Florida
Expected presentation date	Apr 2020

Additional Data

Portions	Fig. 7

Requestor Location

Requestor Location	University of Central Florida 12760 Pegasus Dr. ENG I, Suite 207 ORLANDO, FL 32816 United States Attn: University of Central Florida

Tax Details

Publisher Tax ID	98-0397604

APPENDIX F: COPYRIGHT PERMISSION LETTER FOR FIGURE 1.11

1. Energy & environmental science

Billing Status: Open

Print License

Order license ID	1028091-1	Type of use	Republish in a thesis/dissert...
Order detail status	Completed	Publisher	RSC Publishing
ISSN	1754-5706	Portion	Chart/graph/table/figure

0.00 USD
Republication Permission

Hide Details

LICENSED CONTENT

Publication Title	Energy & environmental scie...	Country	United Kingdom of Great Bri...
Author/Editor	Royal Society of Chemistry (...	Rightsholder	Royal Society of Chemistry
Date	01/01/2008	Publication Type	e-Journal
Language	English	URL	http://www.rsc.org/Publishi...

REQUEST DETAILS

Portion Type	Chart/graph/table/figure	Distribution	Worldwide
Number of charts / graphs / tables / figures requested	2	Translation	Original language of publica...
		Copies for the disabled?	No
Format (select all that apply)	Print,Electronic	Minor editing privileges?	Yes
Who will republish the content?	Academic institution	Incidental promotional use?	No
		Currency	USD
Duration of Use	Life of current edition		
Lifetime Unit Quantity	Up to 499		
Rights Requested	Main product		

NEW WORK DETAILS

Title	CERIUM OXIDE BASED NAN...	Institution name	University of Central Florida
Instructor name	Sudipta Seal	Expected presentation date	2020-05-02

ADDITIONAL DETAILS

The requesting person / organization to appear on the license	Aadithya Jeyaranjan

REUSE CONTENT DETAILS

Title, description or numeric reference of the portion(s)	Fig. 13	Title of the article/chapter the portion is from	3.4 Nanostructured layered ...
Editor of portion(s)	N/A	Author of portion(s)	Royal Society of Chemistry (...
Volume of serial or monograph	N/A	Publication date of portion	2014-03-13
Page or page range of portion	1606		

Total Items: 1

Subtotal: 0.00 USD

Order Total: 0.00 USD

APPENDIX G: COPYRIGHT PERMISSION LETTER FOR CHAPTER 2

Copyright Clearance Center | RightsLink®

Home | Help | Email Support | Aadithya Jeyaranjan

Morphology and Crystal Planes Effects on Supercapacitance of CeO2 Nanostructures: Electrochemical and Molecular Dynamics Studies

Author: Sudipta Seal, Dean C. Sayle, Marco Molinari, et al
Publication: Particle & Particle Systems Characterization
Publisher: John Wiley and Sons
Date: Aug 9, 2018

Order Completed

Thank you for your order.

This Agreement between University of Central Florida -- Aadithya Jeyaranjan ("You") and John Wiley and Sons ("John Wiley and Sons") consists of your license details and the terms and conditions provided by John Wiley and Sons and Copyright Clearance Center.

Your confirmation email will contain your order number for future reference.

License Number	4806740204498
License date	Apr 12, 2020

Printable Details

Licensed Content

Licensed Content Publisher	John Wiley and Sons
Licensed Content Publication	Particle & Particle Systems Characterization
Licensed Content Title	Morphology and Crystal Planes Effects on Supercapacitance of CeO2 Nanostructures: Electrochemical and Molecular Dynamics Studies
Licensed Content Author	Sudipta Seal, Dean C. Sayle, Marco Molinari, et al
Licensed Content Date	Aug 9, 2018
Licensed Content Volume	35
Licensed Content Issue	10
Licensed Content Pages	9

Order Details

Type of use	Dissertation/Thesis
Requestor type	Author of this Wiley article
Format	Print and electronic
Portion	Full article
Will you be translating?	No

About Your Work

Title	CERIUM OXIDE BASED NANOCOMPOSITES FOR SUPERCAPACITORS
Institution name	University of Central Florida
Expected presentation date	Apr 2020

Additional Data

Requestor Location

	University of Central Florida 12760 Pegasus Dr, ENG I, Suite 207
Requestor Location	ORLANDO, FL 32816 United States Attn: University of Central Florida

Tax Details

Publisher Tax ID	EU826007151

APPENDIX H: COPYRIGHT PERMISSION LETTER FOR CHAPTER 3

APPENDIX I: LIST OF PUBLICATIONS

1. T K Das, T S Sakthivel, **A Jeyaranjan,** S Seal, A N Bezbaruaha. (2020) Ultra-high Arsenic Adsorption by Graphene Oxide Iron Nanohybrid: Removal Mechanisms and Potential Applications, Chemosphere, (accepted)
2. Sudipta Seal, **Jeyaranjan, Aadithya**, Craig J. Neal, Tamil Selvan Sakthivel, and Udit Kumar. “Engineering Defects in Cerium Oxides: Tuning Chemical Reactivity for Biomedical, Environmental, & Energy Applications.” Nanoscale
3. **Jeyaranjan, Aadithya**, Tamil Selvan Sakthivel, Craig J. Neal, and Sudipta Seal. "Scalable ternary hierarchical microspheres composed of PANI/rGO/CeO2 for high performance supercapacitor applications." Carbon 151 (2019): 192-202.
4. **Jeyaranjan, Aadithya,** Tamil Selvan Sakthivel, Marco Molinari, Dean C. Sayle, and Sudipta Seal. "Morphology and crystal planes effects on supercapacitance of CeO2 nanostructures: electrochemical and molecular dynamics studies." Particle & Particle Systems Characterization 35, no. 10 (2018): 1800176
5. Niu, Wenhan, **Aadithya Jeyaranjan**, Sudipta Seal, and Yang Yang. "Correction to Amorphous MOF Introduced N-Doped Graphene: An Efficient and Versatile Electrocatalyst for Zinc–Air Battery and Water Splitting." ACS Applied Energy Materials 1, no. 8 (2018): 4413-4413.
6. Shen, Chen, Jean E. Calderon, Elizabeth Barrios, Mikhael Soliman, Ali Khater, **Aadithya Jeyaranjan**, Laurene Tetard, Ali Gordon, Sudipta Seal, and Lei Zhai. "Anisotropic electrical conductivity in polymer derived ceramics induced

by graphene aerogels." Journal of Materials Chemistry C 5, no. 45 (2017): 11708-11716.

REFERENCES

1. U.S. Energy Information Administration EIA projects nearly 50% increase in world energy usage by 2050, led by growth in Asia. https://www.eia.gov/todayinenergy/detail.php?id=41433.

2. Simon, P.; Gogotsi, Y., Materials for electrochemical capacitors. *Nature Materials* **2008,** *7* (11), nmat2297.

3. Simon, P.; Gogotsi, Y.; Dunn, B., Where do batteries end and supercapacitors begin? *Science* **2014,** *343* (6176), 1210-1211.

4. Conway, B. E., *Electrochemical Supercapacitors: Scientific Fundamentals and Technological Applications*. Springer Science & Business Media: 2013; p 714.

5. Conway, B. E., Transition from “Supercapacitor” to “Battery” Behavior in Electrochemical Energy Storage. *J. Electrochem. Soc.* **1991,** *138* (6), 1539-1548.

6. Rauda, I. E.; Augustyn, V.; Dunn, B.; Tolbert, S. H., Enhancing pseudocapacitive charge storage in polymer templated mesoporous materials. *Acc Chem Res* **2013,** *46* (5), 1113-24.

7. Augustyn, V.; Simon, P.; Dunn, B., Pseudocapacitive oxide materials for high-rate electrochemical energy storage. *Energy Environ. Sci.* **2014,** *7* (5), 1597-1614.

8. Miller, J. R.; Burke, A. F., Electrochemical capacitors: challenges and opportunities for real-world applications. *The Electrochemical Society Interface* **2008,** *17* (1), 53.

9. Miller, J. R., Engineering electrochemical capacitor applications. *Journal of Power Sources* **2016,** *326*, 726-735.

10. González, A.; Goikolea, E.; Barrena, J. A.; Mysyk, R. J. R.; Reviews, S. E., Review on supercapacitors: technologies and materials. **2016,** *58*, 1189-1206.

11. Snook, G. A.; Kao, P.; Best, A. S., Conducting-polymer-based supercapacitor devices and electrodes. *Journal of Power Sources* **2011,** *196* (1), 1-12.

12. Eftekhari, A.; Li, L.; Yang, Y., Polyaniline supercapacitors. *Journal of Power Sources* **2017,** *347*, 86-107.

13. Wang, H.; Lin, J.; Shen, Z. X., Polyaniline (PANi) based electrode materials for energy storage and conversion. *Journal of Science: Advanced Materials and Devices* **2016,** *1* (3), 225-255.

14. Liu, Y.; Zhou, G. In *Key Technologies and Applications of Internet of Things*, 2012 Fifth International Conference on Intelligent Computation Technology and Automation, 2012/01//; 2012; pp 197-200.

15. Yun, M.; Yuxin, B. In *Research on the architecture and key technology of Internet of Things (IoT) applied on smart grid*, 2010; IEEE: 2010; pp 69-72.

16. Atzori, L.; Iera, A.; Morabito, G., The Internet of Things: A survey. *Computer Networks* **2010,** *54* (15), 2787-2805.

17. Khan, R.; Khan, S. U.; Zaheer, R.; Khan, S. In *Future Internet: The Internet of Things Architecture, Possible Applications and Key Challenges*, 2012 10th International Conference on Frontiers of Information Technology, 2012/12//; 2012; pp 257-260.

18. Swan, M., Sensor mania! the internet of things, wearable computing, objective metrics, and the quantified self 2.0. *Journal of Sensor and Actuator Networks* **2012,** *1* (3), 217-253.

19. Curtin, T. B.; Bellingham, J. G.; Catipovic, J.; Webb, D., Autonomous oceanographic sampling networks. *Oceanography* **1993,** *6* (3), 86-94.

20. Vullers, R. J. M.; Van Schaijk, R.; Visser, H. J.; Penders, J.; Van Hoof, C., Energy harvesting for autonomous wireless sensor networks. *IEEE Solid-State Circuits Magazine* **2010,** *2* (2), 29-38.

21. Weimer, M. A.; Paing, T. S.; Zane, R. A., Remote area wind energy harvesting for low-power autonomous sensors. *system* **2006,** *2* (1), 2.

22. Haight, R.; Haensch, W.; Friedman, D., Solar-powering the Internet of Things. *Science* **2016,** *353* (6295), 124-125.

23. Gogotsi, Y.; Simon, P., True performance metrics in electrochemical energy storage. *Science* **2011,** *334* (6058), 917-918.

24. Conway, B. E., *Electrochemical supercapacitors: scientific fundamentals and technological applications*. Springer Science & Business Media: 2013.

25. Reddy, R. N.; Reddy, R. G., Sol–gel MnO 2 as an electrode material for electrochemical capacitors. *Journal of Power Sources* **2003,** *124* (1), 330-337.

26. Chen, Z.; Augustyn, V.; Wen, J.; Zhang, Y.; Shen, M.; Dunn, B.; Lu, Y., High-Performance Supercapacitors Based on Intertwined CNT/V2O5 Nanowire Nanocomposites. *Advanced materials* **2011,** *23* (6), 791-795.

27. Brezesinski, T.; Wang, J.; Tolbert, S. H.; Dunn, B., Ordered mesoporous [alpha]-MoO3 with iso-oriented nanocrystalline walls for thin-film pseudocapacitors. *Nature materials* **2010,** *9* (2), 146-151.

28. Zhang, X.; Shi, W.; Zhu, J.; Zhao, W.; Ma, J.; Mhaisalkar, S.; Maria, T. L.; Yang, Y.; Zhang, H.; Hng, H. H., Synthesis of porous NiO nanocrystals with controllable surface area and their application as supercapacitor electrodes. *Nano Research* **2010,** *3* (9), 643-652.

29. Yuan, C.; Zhang, X.; Su, L.; Gao, B.; Shen, L., Facile synthesis and self-assembly of hierarchical porous NiO nano/micro spherical superstructures for high performance supercapacitors. *J. Mater. Chem.* **2009,** *19* (32), 5772-5777.

30. Xiong, S.; Yuan, C.; Zhang, X.; Xi, B.; Qian, Y., Controllable synthesis of mesoporous Co3O4 nanostructures with tunable morphology for application in supercapacitors. *Chemistry-A European Journal* **2009,** *15* (21), 5320-5326.

31. Fu, Y.; Gao, X.; Zha, D.; Zhu, J.; Ouyang, X.; Wang, X., Yolk–shell-structured MnO2 microspheres with oxygen vacancies for high-performance supercapacitors. *Journal of Materials Chemistry A* **2018,** *6* (4), 1601-1611.

32. Bhojane, P.; Sinha, L.; Devan, R. S.; Shirage, P. M., Mesoporous layered hexagonal platelets of Co 3 O 4 nanoparticles with (111) facets for battery applications: high performance and ultra-high rate capability. *Nanoscale* **2018**.

33. Zhao, X.; Mendoza Sánchez, B.; J. Dobson, P.; S. Grant, P., The role of nanomaterials in redox-based supercapacitors for next generation energy storage devices. *Nanoscale* **2011,** *3* (3), 839-855.

34. Anasori, B.; Lukatskaya, M. R.; Gogotsi, Y., 2D metal carbides and nitrides (MXenes) for energy storage. *Nature Reviews Materials* **2017,** *2* (2), natrevmats201698.

35. Zhou, H.; Chen, H.; Luo, S.; Lu, G.; Wei, W.; Kuang, Y., The effect of the polyaniline morphology on the performance of polyaniline supercapacitors. *Journal of Solid State Electrochemistry* **2005,** *9* (8), 574-580.

36. Acerce, M.; Voiry, D.; Chhowalla, M., Metallic 1T phase MoS₂ nanosheets as supercapacitor electrode materials. *Nature Nanotechnology* **2015,** *10* (4), nnano.2015.40.

37. Zhu, Y.; Li, N.; Lv, T.; Yao, Y.; Peng, H.; Shi, J.; Cao, S.; Chen, T., Ag-Doped PEDOT:PSS/CNT composites for thin-film all-solid-state supercapacitors with a stretchability of 480%. *J. Mater. Chem. A* **2018,** *6* (3), 941-947.

38. Brezesinski, T.; Wang, J.; Senter, R.; Brezesinski, K.; Dunn, B.; Tolbert, S. H., On the Correlation between Mechanical Flexibility, Nanoscale Structure, and Charge Storage in Periodic Mesoporous CeO2 Thin Films. *ACS Nano* **2010,** *4* (2), 967-977.

39. Heydari, H.; Gholivand, M. B., A novel high-performance supercapacitor based on high-quality CeO2/nitrogen-doped reduced graphene oxide nanocomposite. *Applied Physics A* **2017,** *123* (3), 187.

40. Dezfuli, A. S.; Ganjali, M. R.; Naderi, H. R.; Norouzi, P., A high performance supercapacitor based on a ceria/graphene nanocomposite synthesized by a facile sonochemical method. *RSC Advances* **2015,** *5* (57), 46050-46058.

41. Kumar, R.; Agrawal, A.; Nagarale, R. K.; Sharma, A., High performance supercapacitors from novel metal-doped ceria-decorated aminated graphene. *J. Phys. Chem. C* **2016,** *120* (6), 3107-3116.

42. Tao, Y.; Ruiyi, L.; Haiyan, Z.; Zaijun, L., Ceria nanoparticles uniformly decorated on graphene nanosheets with coral-like morphology for high-performance supercapacitors. *Materials Research Bulletin* **2016,** *78*, 163-171.

43. Corma, A.; Atienzar, P.; García, H.; Chane-Ching, J.-Y., Hierarchically mesostructured doped CeO2 with potential for solar-cell use. *Nature materials* **2004,** *3* (6), 394-397.

44. Karakoti, A.; Singh, S.; Dowding, J. M.; Seal, S.; Self, W. T., Redox-active radical scavenging nanomaterials. *Chemical Society Reviews* **2010,** *39* (11), 4422-4432.

45. Trovarelli, A., Catalytic properties of ceria and CeO2-containing materials. *Catalysis Reviews* **1996,** *38* (4), 439-520.

46. Montini, T.; Melchionna, M.; Monai, M.; Fornasiero, P., Fundamentals and catalytic applications of CeO2-based materials. *Chemical reviews* **2016,** *116* (10), 5987-6041.

47. Sayle, D. C.; Seal, S.; Wang, Z.; Mangili, B. C.; Price, D. W.; Karakoti, A. S.; Kuchibhatla, S. V. T. N.; Hao, Q.; Mobus, G.; Xu, X., Mapping nanostructure: a systematic enumeration of nanomaterials by assembling nanobuilding blocks at crystallographic positions. *ACS Nano* **2008,** *2* (6), 1237-1251.

48. Sayle, D. C.; Feng, X.; Ding, Y.; Wang, Z. L.; Sayle, T. X. T., “Simulating synthesis”: Ceria nanosphere self-assembly into nanorods and framework architectures. *J. Am. Chem. Soc.* **2007,** *129* (25), 7924-7935.

49. Aravinda, L. S.; Bhat, K. U.; Bhat, B. R., Nano CeO 2/activated carbon based composite electrodes for high performance supercapacitor. *Materials Letters* **2013,** *112*, 158-161.

50. Ji, Z.; Shen, X.; Zhou, H.; Chen, K., Facile synthesis of reduced graphene oxide/CeO 2 nanocomposites and their application in supercapacitors. *Ceramics International* **2015,** *41* (7), 8710-8716.

51. Kalubarme, R. S.; Kim, Y.-H.; Park, C.-J., One step hydrothermal synthesis of a carbon nanotube/cerium oxide nanocomposite and its electrochemical properties. *Nanotechnology* **2013,** *24* (36), 365401.

52. Maheswari, N.; Muralidharan, G., Supercapacitor behavior of cerium oxide nanoparticles in neutral aqueous electrolytes. *Energy & Fuels* **2015,** *29* (12), 8246-8253.

53. Padmanathan, N.; Selladurai, S., Shape controlled synthesis of CeO 2 nanostructures for high performance supercapacitor electrodes. *RSC Advances* **2014,** *4* (13), 6527-6534.

54. Maiti, S.; Pramanik, A.; Mahanty, S., Extraordinarily high pseudocapacitance of metal organic framework derived nanostructured cerium oxide. *Chemical Communications* **2014,** *50* (79), 11717-11720.

55. Kyerematen, N. A.; Brousse, T.; Pech, D., Microsupercapacitors as miniaturized energy-storage components for on-chip electronics. *Nature Nanotechnology* **2016,** *12* (1), nnano.2016.196.

56. Liu, X.; Liu, J.; Chang, Z.; Sun, X.; Li, Y., Crystal plane effect of Fe 2 O 3 with various morphologies on CO catalytic oxidation. *Catalysis Communications* **2011,** *12* (6), 530-534.

57. Wang, Y.; Zhong, Z.; Chen, Y.; Ng, C. T.; Lin, J., Controllable synthesis of Co3O4 from nanosize to microsize with large-scale exposure of active crystal planes and their excellent rate capability in supercapacitors based on the crystal plane effect. *Nano Research* **2011,** *4* (7), 695.

58. Xiao, X.; Liu, X.; Zhao, H.; Chen, D.; Liu, F.; Xiang, J.; Hu, Z.; Li, Y., Facile Shape Control of Co3O4 and the Effect of the Crystal Plane on Electrochemical Performance. *Advanced Materials* **2012,** *24* (42), 5762-5766.

59. Mai, H.-X.; Sun, L.-D.; Zhang, Y.-W.; Si, R.; Feng, W.; Zhang, H.-P.; Liu, H.-C.; Yan, C.-H., Shape-selective synthesis and oxygen storage behavior of ceria nanopolyhedra, nanorods, and nanocubes. *The Journal of Physical Chemistry B* **2005,** *109* (51), 24380-24385.

60. Huang, W.; Gao, Y., Morphology-dependent surface chemistry and catalysis of CeO 2 nanocrystals. *Catalysis Science & Technology* **2014,** *4* (11), 3772-3784.

61. Sayle, T. X. T.; Parker, S. C.; Catlow, C. R. A., The role of oxygen vacancies on ceria surfaces in the oxidation of carbon monoxide. *Surface Science* **1994,** *316* (3), 329-336.

62. Sakthivel, T.; Das, S.; Kumar, A.; Reid, D. L.; Gupta, A.; Sayle, D. C.; Seal, S., Morphological Phase Diagram of Biocatalytically Active Ceria Nanostructures as a

Function of Processing Variables and Their Properties. *ChemPlusChem* **2013,** *78* (12), 1446-1455.

63. Feng, X.; Sayle, D. C.; Wang, Z. L.; Paras, M. S.; Santora, B.; Sutorik, A. C.; Sayle, T. X. T.; Yang, Y.; Ding, Y.; Wang, X., Converting ceria polyhedral nanoparticles into single-crystal nanospheres. *Science* **2006,** *312* (5779), 1504-1508.

64. Caddeo, F.; Corrias, A.; Sayle, D. C., Tuning the Properties of Nanoceria by Applying Force: Stress-Induced Ostwald Ripening. *J. Phys. Chem. C* **2016,** *120* (26), 14337-14344.

65. Sayle, T. X. T.; Parker, S. C.; Sayle, D. C., Shape of CeO 2 nanoparticles using simulated amorphisation and recrystallisation. *Chemical Communications* **2004,** (21), 2438-2439.

66. Sayle, D. C.; Maicaneanu, S. A.; Watson, G. W., Atomistic models for CeO2 (111),(110), and (100) nanoparticles, supported on yttrium-stabilized zirconia. *J. Am. Chem. Soc.* **2002,** *124* (38), 11429-11439.

67. Chang, J.; Lee, W.; Mane, R. S.; Cho, B. W.; Han, S.-H., Morphology-dependent electrochemical supercapacitor properties of indium oxide. *Electrochemical and Solid-State Letters* **2008,** *11* (1), A9-A11.

68. Choi, D.; Blomgren, G. E.; Kumta, P. N., Fast and reversible surface redox reaction in nanocrystalline vanadium nitride supercapacitors. *Advanced Materials* **2006,** *18* (9), 1178-1182.

69. Mai, L.-Q.; Yang, F.; Zhao, Y.-L.; Xu, X.; Xu, L.; Luo, Y.-Z., Hierarchical MnMoO 4/CoMoO 4 heterostructured nanowires with enhanced supercapacitor performance. *Nature communications* **2011,** *2*, ncomms1387.

70. Kim, J. W.; Augustyn, V.; Dunn, B., The Effect of Crystallinity on the Rapid Pseudocapacitive Response of Nb2O5. *Adv Energy Mater* **2012,** *2* (1), 141-148.

71. Wang, J.; Polleux, J.; Lim, J.; Dunn, B., Pseudocapacitive Contributions to Electrochemical Energy Storage in TiO2 (Anatase) Nanoparticles. *J. Phys. Chem. C* **2007,** *111* (40), 14925-14931.

72. Yan, J.; Fan, Z.; Sun, W.; Ning, G.; Wei, T.; Zhang, Q.; Zhang, R.; Zhi, L.; Wei, F., Advanced asymmetric supercapacitors based on Ni (OH) 2/graphene and porous graphene electrodes with high energy density. *Advanced Functional Materials* **2012,** *22* (12), 2632-2641.

73. Kong, L.-B.; Lang, J.-W.; Liu, M.; Luo, Y.-C.; Kang, L., Facile approach to prepare loose-packed cobalt hydroxide nano-flakes materials for electrochemical capacitors. *Journal of Power Sources* **2009,** *194* (2), 1194-1201.

74. Dubal, D. P.; Fulari, V. J.; Lokhande, C. D., Effect of morphology on supercapacitive properties of chemically grown β-Ni (OH) 2 thin films. *Microporous and Mesoporous Materials* **2012,** *151*, 511-516.

75. Gund, G. S.; Dubal, D. P.; Patil, B. H.; Shinde, S. S.; Lokhande, C. D., Enhanced activity of chemically synthesized hybrid graphene oxide/Mn3O4 composite for high performance supercapacitors. *Electrochimica Acta* **2013,** *92*, 205-215.

76. González, A.; Goikolea, E.; Barrena, J. A.; Mysyk, R., Review on supercapacitors: technologies and materials. *Renewable and Sustainable Energy Reviews* **2016,** *58*, 1189-1206.

77. Ghodbane, O.; Pascal, J.-L.; Favier, F., Microstructural effects on charge-storage properties in MnO2-based electrochemical supercapacitors. *Acs Appl Mater Inter* **2009,** *1* (5), 1130-1139.

78. Molinari, M.; Parker, S. C.; Sayle, D. C.; Islam, M. S., Water adsorption and its effect on the stability of low index stoichiometric and reduced surfaces of ceria. *J. Phys. Chem. C* **2012,** *116* (12), 7073-7082.

79. Sayle, T. X. T.; Molinari, M.; Das, S.; Bhatta, U. M.; Möbus, G.; Parker, S. C.; Seal, S.; Sayle, D. C., Environment-mediated structure, surface redox activity and reactivity of ceria nanoparticles. *Nanoscale* **2013,** *5* (13), 6063-6073.

80. Sayle, T. X. T.; Cantoni, M.; Bhatta, U. M.; Parker, S. C.; Hall, S. R.; Möbus, G.; Molinari, M.; Reid, D.; Seal, S.; Sayle, D. C., Strain and Architecture-Tuned Reactivity in Ceria Nanostructures; Enhanced Catalytic Oxidation of CO to CO2. *Chem. Mater.* **2012,** *24* (10), 1811-1821.

81. Watson, G. W., ET Kelsey, NH de Leeuw, DJ Harris and SC Parker J. *Chem. Soc. Faraday Trans* **1996,** *92*, 433-438.

82. Smith, W.; Forester, T. R., DL_POLY_2. 0: A general-purpose parallel molecular dynamics simulation package. *Journal of molecular graphics* **1996,** *14* (3), 136-141.

83. Conesa, J., Computer modeling of surfaces and defects on cerium dioxide. *Surface Science* **1995,** *339* (3), 337-352.

84. Nolan, M.; Grigoleit, S.; Sayle, D. C.; Parker, S. C.; Watson, G. W., Density functional theory studies of the structure and electronic structure of pure and defective low index surfaces of ceria. *Surface Science* **2005,** *576* (1), 217-229.

85. Miller, J. R.; Simon, P., Electrochemical Capacitors for Energy Management. *Science* **2008,** *321* (5889), 651-652.

86. Miller, J. M. In *Energy storage technology markets and application's: ultracapacitors in combination with lithium-ion*, 2007 7th Internatonal Conference on Power Electronics, 2007/10//; 2007; pp 16-22.

87. Abioye, A. M.; Ani, F. N., Recent development in the production of activated carbon electrodes from agricultural waste biomass for supercapacitors: A review. *Renewable and Sustainable Energy Reviews* **2015,** *52*, 1282-1293.

88. Li Zhang, L.; S. Zhao, X., Carbon-based materials as supercapacitor electrodes. *Chemical Society Reviews* **2009,** *38* (9), 2520-2531.

89. Liu, C.; Yu, Z.; Neff, D.; Zhamu, A.; Jang, B. Z., Graphene-Based Supercapacitor with an Ultrahigh Energy Density. *Nano Lett.* **2010,** *10* (12), 4863-4868.

90. Zhu, Y.; Murali, S.; Stoller, M. D.; Ganesh, K. J.; Cai, W.; Ferreira, P. J.; Pirkle, A.; Wallace, R. M.; Cychosz, K. A.; Thommes, M.; Su, D.; Stach, E. A.; Ruoff, R. S., Carbon-Based Supercapacitors Produced by Activation of Graphene. *Science* **2011,** *332* (6037), 1537-1541.

91. Meher, S. K.; Rao, G. R., Ultralayered Co3O4 for High-Performance Supercapacitor Applications. *J. Phys. Chem. C* **2011,** *115* (31), 15646-15654.

92. Fusalba, F.; Gouérec, P.; Villers, D.; Bélanger, D., Electrochemical Characterization of Polyaniline in Nonaqueous Electrolyte and Its Evaluation as Electrode Material for Electrochemical Supercapacitors. *J. Electrochem. Soc.* **2001,** *148* (1), A1-A6.

93. Liu, T.; Finn, L.; Yu, M.; Wang, H.; Zhai, T.; Lu, X.; Tong, Y.; Li, Y., Polyaniline and Polypyrrole Pseudocapacitor Electrodes with Excellent Cycling Stability. *Nano Lett.* **2014,** *14* (5), 2522-2527.

94. Gong, Q.; Li, Y.; Huang, H.; Zhang, J.; Gao, T.; Zhou, G., Shape-controlled synthesis of Ni-CeO2@PANI nanocomposites and their synergetic effects on supercapacitors. *Chemical Engineering Journal* **2018,** *344*, 290-298.

95. Wang, Y.; Xian Guo, C.; Liu, J.; Chen, T.; Yang, H.; Ming Li, C., CeO 2 nanoparticles / graphene nanocomposite-based high performance supercapacitor. *Dalton Transactions* **2011,** *40* (24), 6388-6391.

96. Jeyaranjan, A.; Sakthivel, T. S.; Molinari, M.; Sayle, D. C.; Seal, S., Morphology and Crystal Planes Effects on Supercapacitance of CeO2 Nanostructures: Electrochemical and Molecular Dynamics Studies. *Particle & Particle Systems Characterization* **2018,** *35* (10), 1800176.

97. Jeon, I.-Y.; Bae, S.-Y.; Seo, J.-M.; Baek, J.-B., Scalable Production of Edge-Functionalized Graphene Nanoplatelets via Mechanochemical Ball-Milling. *Advanced Functional Materials* **2015,** *25* (45), 6961-6975.

98. Tung, V. C.; Allen, M. J.; Yang, Y.; Kaner, R. B., High-throughput solution processing of large-scale graphene. *Nature Nanotechnology* **2009,** *4* (1), 25-29.

99. Wang, Y.; Wu, Y.; Huang, Y.; Zhang, F.; Yang, X.; Ma, Y.; Chen, Y., Preventing Graphene Sheets from Restacking for High-Capacitance Performance. *J. Phys. Chem. C* **2011,** *115* (46), 23192-23197.

100. Xu, Y.; Lin, Z.; Huang, X.; Wang, Y.; Huang, Y.; Duan, X., Functionalized Graphene Hydrogel-Based High-Performance Supercapacitors. *Advanced Materials* **2013,** *25* (40), 5779-5784.

101. Xu, D. F.; Chen, C. J.; Xie, J.; Zhang, B.; Miao, L.; Cai, J.; Huang, Y. H.; Zhang, L. N., A Hierarchical N/S-Codoped Carbon Anode Fabricated Facilely from Cellulose/Polyaniline Microspheres for High-Performance Sodium-Ion Batteries. *Adv Energy Mater* **2016,** *6* (6), 1501929.

102. Xu, Q.; Li, J. Y.; Sun, J. K.; Yin, Y. X.; Wan, L. J.; Guo, Y. G., Watermelon-Inspired Si/C Microspheres with Hierarchical Buffer Structures for Densely Compacted Lithium-Ion Battery Anodes. *Adv Energy Mater* **2017,** *7* (3), 1601481.

103. Ai, Z. H.; Ho, W. K.; Lee, S. C.; Zhang, L. Z., Efficient Photocatalytic Removal of NO in Indoor Air with Hierarchical Bismuth Oxybromide Nanoplate Microspheres under Visible Light. *Environ Sci Technol* **2009,** *43* (11), 4143-4150.

104. Hu, F. Y.; Chen, J. J.; Peng, Y.; Song, H.; Li, K. Z.; Li, J. H., Novel nanowire self-assembled hierarchical CeO2 microspheres for low temperature toluene catalytic combustion. *Chemical Engineering Journal* **2018,** *331*, 425-434.

105. Lee, J.-H., Gas sensors using hierarchical and hollow oxide nanostructures: Overview. *Sensors and Actuators B: Chemical* **2009,** *140* (1), 319-336.

106. Zhou, X.; Li, X.; Sun, H.; Sun, P.; Liang, X.; Liu, F.; Hu, X.; Lu, G., Nanosheet-assembled ZnFe2O4 hollow microspheres for high-sensitive acetone sensor. *ACS Appl. Mater. Interfaces* **2015,** *7* (28), 15414-21.

107. Lei, Y.; Li, J.; Wang, Y. Y.; Gu, L.; Chang, Y. F.; Yuan, H. Y.; Xiao, D., Rapid Microwave-Assisted Green Synthesis of 3D Hierarchical Flower-Shaped NiCo2O4 Microsphere for High-Performance Supercapacitor. *Acs Appl Mater Inter* **2014,** *6* (3), 1773-1780.

108. Wang, Q.; Zhu, L.; Sun, L.; Liu, Y.; Jiao, L., Facile synthesis of hierarchical porous ZnCo 2 O 4 microspheres for high-performance supercapacitors. *Journal of Materials Chemistry A* **2015,** *3* (3), 982-985.

109. Yuan, C. Z.; Zhang, X. G.; Su, L. H.; Gao, B.; Shen, L. F., Facile synthesis and self-assembly of hierarchical porous NiO nano/micro spherical superstructures for high performance supercapacitors. *J. Mater. Chem.* **2009,** *19* (32), 5772-5777.

110. Zhang, D.; Zhao, J.; Feng, C.; Zhao, R.; Sun, Y.; Guan, T.; Han, B.; Tang, N.; Wang, J.; Li, K.; Qiao, J.; Zhang, J., Scalable synthesis of hierarchical macropore-rich activated carbon microspheres assembled by carbon nanoparticles for high rate performance supercapacitors. *Journal of Power Sources* **2017,** *342*, 363-370.

111. Li, Y.; Liu, J.; Huang, X.; Li, G., Hydrothermal synthesis of Bi2WO6 uniform hierarchical microspheres. *Crystal growth & design* **2007,** *7* (7), 1350-1355.

112. Eun Lee, J.; Yu, S.-H.; Jun Lee, D.; Lee, D.-C.; Ihn Han, S.; Sung, Y.-E.; Hyeon, T., Facile and economical synthesis of hierarchical carbon-coated magnetite

nanocomposite particles and their applications in lithium ion battery anodes. *Energy Environ. Sci.* **2012,** *5* (11), 9528-9533.

113. Jeong, J.-M.; Choi, B. G.; Lee, S. C.; Lee, K. G.; Chang, S.-J.; Han, Y.-K.; Lee, Y. B.; Lee, H. U.; Kwon, S.; Lee, G., Hierarchical hollow spheres of Fe2O3@ polyaniline for lithium ion battery anodes. *Advanced Materials* **2013,** *25* (43), 6250-6255.

114. Wang, S.; Langrish, T., A review of process simulations and the use of additives in spray drying. *Food Research International* **2009,** *42* (1), 13-25.

115. Vehring, R., Pharmaceutical Particle Engineering via Spray Drying. *Pharm Res* **2008,** *25* (5), 999-1022.

116. Bertrand, G.; Filiatre, C.; Mahdjoub, H.; Foissy, A.; Coddet, C., Influence of slurry characteristics on the morphology of spray-dried alumina powders. *Journal of the European Ceramic Society* **2003,** *23* (2), 263-271.

117. Sánchez, E.; Moreno, A.; Vicent, M.; Salvador, M. D.; Bonache, V.; Klyatskina, E.; Santacruz, I.; Moreno, R., Preparation and spray drying of Al2O3–TiO2 nanoparticle suspensions to obtain nanostructured coatings by APS. *Surface and Coatings Technology* **2010,** *205* (4), 987-992.

118. Iskandar, F.; Nandiyanto, A. B. D.; Yun, K. M.; Hogan, C. J.; Okuyama, K.; Biswas, P., Enhanced Photocatalytic Performance of Brookite TiO2 Macroporous Particles Prepared by Spray Drying with Colloidal Templating. *Advanced Materials* **2007,** *19* (10), 1408-1412.

119. Nandiyanto, A. B. D.; Okuyama, K., Progress in developing spray-drying methods for the production of controlled morphology particles: From the nanometer to submicrometer size ranges. *Advanced Powder Technology* **2011,** *22* (1), 1-19.

120. Huang, J.; Kaner, R. B., Nanofiber Formation in the Chemical Polymerization of Aniline: A Mechanistic Study. *Angewandte Chemie* **2004,** *116* (43), 5941-5945.

121. Li, D.; Kaner, R. B., Shape and Aggregation Control of Nanoparticles: Not Shaken, Not Stirred. *J. Am. Chem. Soc.* **2006,** *128* (3), 968-975.

122. Du, N.; Zhang, H.; Chen, B.; Ma, X.; Yang, D., Ligand-free Self-Assembly of Ceria Nanocrystals into Nanorods by Oriented Attachment at Low Temperature. *J. Phys. Chem. C* **2007,** *111* (34), 12677-12680.

123. Wu, Q.; Zhang, F.; Xiao, P.; Tao, H.; Wang, X.; Hu, Z.; Lü, Y., Great Influence of Anions for Controllable Synthesis of CeO2 Nanostructures: From Nanorods to Nanocubes. *J. Phys. Chem. C* **2008,** *112* (44), 17076-17080.

124. Zhang, D.; Du, X.; Shi, L.; Gao, R., Shape-controlled synthesis and catalytic application of ceria nanomaterials. *Dalton Transactions* **2012,** *41* (48), 14455-14475.

125. Jozefowicz, M. E.; Laversanne, R.; Javadi, H. H. S.; Epstein, A. J.; Pouget, J. P.; Tang, X.; MacDiarmid, A. G., Multiple lattice phases and polaron-lattice---spinless-defect competition in polyaniline. *Phys. Rev. B* **1989,** *39* (17), 12958-12961.

126. Yan, J.; Wei, T.; Shao, B.; Fan, Z.; Qian, W.; Zhang, M.; Wei, F., Preparation of a graphene nanosheet/polyaniline composite with high specific capacitance. *Carbon* **2010,** *48* (2), 487-493.

127. Tang, J.; Jing, X.; Wang, B.; Wang, F., Infrared spectra of soluble polyaniline. *Synthetic Metals* **1988,** *24* (3), 231-238.

128. Zhang, X.; Lin, Q.; Zhang, X.; Peng, K., A novel 3D conductive network-based polyaniline/graphitic mesoporous carbon composite electrode with excellent electrochemical performance. *Journal of Power Sources* **2018,** *401*, 278-286.

129. Pan, C.; Gu, H.; Dong, L., Synthesis and electrochemical performance of polyaniline @MnO2/graphene ternary composites for electrochemical supercapacitors. *Journal of Power Sources* **2016,** *303*, 175-181.

130. Wu, Z.; Li, M.; Howe, J.; Meyer, H. M.; Overbury, S. H., Probing Defect Sites on CeO2 Nanocrystals with Well-Defined Surface Planes by Raman Spectroscopy and O2 Adsorption. *Langmuir* **2010,** *26* (21), 16595-16606.

131. Lindfors, T.; Ivaska, A., Raman based pH measurements with polyaniline. *Journal of Electroanalytical Chemistry* **2005,** *580* (2), 320-329.

132. Zhu, S.; Wu, M.; Ge, M.-H.; Zhang, H.; Li, S.-K.; Li, C.-H., Design and construction of three-dimensional CuO/polyaniline/rGO ternary hierarchical architectures for high performance supercapacitors. *Journal of Power Sources* **2016,** *306*, 593-601.

133. Thommes, M.; Kaneko, K.; Neimark, A. V.; Olivier, J. P.; Rodriguez-Reinoso, F.; Rouquerol, J.; Sing, K. S. W., Physisorption of gases, with special reference to the evaluation of surface area and pore size distribution (IUPAC Technical Report). *Pure and Applied Chemistry* **2015,** *87* (9-10), 1051-1069.

134. Ayad, M.; Zaghlol, S., Nanostructured crosslinked polyaniline with high surface area: Synthesis, characterization and adsorption for organic dye. *Chemical Engineering Journal* **2012,** *204-206*, 79-86.

135. Yan, Y.; Cheng, Q.; Zhu, Z.; Pavlinek, V.; Saha, P.; Li, C., Controlled synthesis of hierarchical polyaniline nanowires/ordered bimodal mesoporous carbon nanocomposites with high surface area for supercapacitor electrodes. *Journal of Power Sources* **2013,** *240*, 544-550.

136. Xiong, P.; Hu, C.; Fan, Y.; Zhang, W.; Zhu, J.; Wang, X., Ternary manganese ferrite/graphene/polyaniline nanostructure with enhanced electrochemical capacitance performance. *Journal of Power Sources* **2014,** *266*, 384-392.

137. Xia, X.; Hao, Q.; Lei, W.; Wang, W.; Sun, D.; Wang, X., Nanostructured ternary composites of graphene/Fe 2 O 3 /polyaniline for high-performance supercapacitors. *J. Mater. Chem.* **2012,** *22* (33), 16844-16850.

138. Kang, E. T.; Neoh, K. G.; Tan, K. L., X-ray photoelectron spectroscopic studies of electroactive polymers. In *Polymer Characteristics*, Springer Berlin Heidelberg: Berlin, Heidelberg, 1993; pp 135-190.

139. J. Waghmode, B.; Soni, R.; R. Patil, K.; D. Malkhede, D., Calixarene based nanocomposite materials for high-performance supercapacitor electrode. *New Journal of Chemistry* **2017,** *41* (18), 9752-9761.

140. Macdiarmid, A. G.; Chiang, J. C.; Richter, A. F.; Epstein, A. J., Polyaniline: a new concept in conducting polymers. *Synthetic Metals* **1987,** *18* (1), 285-290.

141. Golczak, S.; Kanciurzewska, A.; Fahlman, M.; Langer, K.; Langer, J. J., Comparative XPS surface study of polyaniline thin films. *Solid State Ionics* **2008,** *179* (39), 2234-2239.

142. Wang, Y. G.; Li, H. Q.; Xia, Y. Y., Ordered Whiskerlike Polyaniline Grown on the Surface of Mesoporous Carbon and Its Electrochemical Capacitance Performance. *Advanced Materials* **2006,** *18* (19), 2619-2623.

143. Hu, C.-C.; Chen, E.; Lin, J.-Y., Capacitive and textural characteristics of polyaniline-platinum composite films. *Electrochimica Acta* **2002,** *47* (17), 2741-2749.

144. Hu, C.-C.; Lin, J.-Y., Effects of the loading and polymerization temperature on the capacitive performance of polyaniline in NaNO3. *Electrochimica Acta* **2002,** *47* (25), 4055-4067.

145. Liu, F.; Luo, S.; Liu, D.; Chen, W.; Huang, Y.; Dong, L.; Wang, L., Facile Processing of Free-Standing Polyaniline/SWCNT Film as an Integrated Electrode for Flexible Supercapacitor Application. *Acs Appl Mater Inter* **2017,** *9* (39), 33791-33801.

146. Wang, S.; Ma, L.; Gan, M.; Fu, S.; Dai, W.; Zhou, T.; Sun, X.; Wang, H.; Wang, H., Free-standing 3D graphene/polyaniline composite film electrodes for high-performance supercapacitors. *Journal of Power Sources* **2015,** *299*, 347-355.

147. Sha, C.; Lu, B.; Mao, H.; Cheng, J.; Pan, X.; Lu, J.; Ye, Z., 3D ternary nanocomposites of molybdenum disulfide/polyaniline/reduced graphene oxide aerogel for high performance supercapacitors. *Carbon* **2016,** *99*, 26-34.

148. Li, J.; Ren, Y.; Ren, Z.; Wang, S.; Qiu, Y.; Yu, J., Aligned polyaniline nanowires grown on the internal surface of macroporous carbon for supercapacitors. *Journal of Materials Chemistry A* **2015,** *3* (46), 23307-23315.

149. Rakhi, R. B.; Chen, W.; Cha, D.; Alshareef, H. N., Substrate Dependent Self-Organization of Mesoporous Cobalt Oxide Nanowires with Remarkable Pseudocapacitance. *Nano Lett.* **2012,** *12* (5), 2559-2567.

150. Wang, K.; Huang, J.; Wei, Z., Conducting Polyaniline Nanowire Arrays for High Performance Supercapacitors. *J. Phys. Chem. C* **2010,** *114* (17), 8062-8067.

151. Wang, G.; Zhang, L.; Zhang, J., A review of electrode materials for electrochemical supercapacitors. *Chemical Society Reviews* **2012,** *41* (2), 797-828.

152. Cong, H.-P.; Ren, X.-C.; Wang, P.; Yu, S.-H., Flexible graphene –polyaniline composite paper for high-performance supercapacitor. *Energy Environ. Sci.* **2013,** *6* (4), 1185-1191.

153. Khomenko, V.; Raymundo-Piñero, E.; Béguin, F., Optimisation of an asymmetric manganese oxide/activated carbon capacitor working at 2V in aqueous medium. *Journal of Power Sources* **2006,** *153* (1), 183-190.

154. Mak, W. F.; Wee, G.; Aravindan, V.; Gupta, N.; Mhaisalkar, S. G.; Madhavi, S., High-Energy Density Asymmetric Supercapacitor Based on Electrospun Vanadium Pentoxide and Polyaniline Nanofibers in Aqueous Electrolyte. *J. Electrochem. Soc.* **2012,** *159* (9), A1481-A1488.

155. Xiong, P.; Huang, H.; Wang, X., Design and synthesis of ternary cobalt ferrite/graphene/polyaniline hierarchical nanocomposites for high-performance supercapacitors. *Journal of Power Sources* **2014,** *245*, 937-946.

156. Yang, C.; Shen, J.; Wang, C.; Fei, H.; Bao, H.; Wang, G., All-solid-state asymmetric supercapacitor based on reduced graphene oxide/carbon nanotube and carbon fiber paper/polypyrrole electrodes. *Journal of Materials Chemistry A* **2013,** *2* (5), 1458-1464.

157. Qu, Z.; Shi, M.; Wu, H.; Liu, Y.; Jiang, J.; Yan, C., An efficient binder-free electrode with multiple carbonized channels wrapped by NiCo2O4 nanosheets for high-performance capacitive energy storage. *Journal of Power Sources* **2019,** *410-411*, 179-187.

158. Wu, L.; Hao, L.; Pang, B.; Wang, G.; Zhang, Y.; Li, X., MnO2 nanoflowers and polyaniline nanoribbons grown on hybrid graphene/Ni 3D scaffolds by in situ electrochemical techniques for high-performance asymmetric supercapacitors. *Journal of Materials Chemistry A* **2017,** *5* (9), 4629-4637.

159. Yu, P.; Zhang, Z.; Zheng, L.; Teng, F.; Hu, L.; Fang, X., A Novel Sustainable Flour Derived Hierarchical Nitrogen-Doped Porous Carbon/Polyaniline Electrode for Advanced Asymmetric Supercapacitors. *Adv Energy Mater* **2016,** *6* (20), 1601111.

160. Xu, J.; Sun, Y.; Lu, M.; Wang, L.; Zhang, J.; Qian, J.; Liu, X., Fabrication of hierarchical MnMoO4·H2O@MnO2 core-shell nanosheet arrays on nickel foam as an advanced electrode for asymmetric supercapacitors. *Chemical Engineering Journal* **2018,** *334*, 1466-1476.

161. Zhao, P.; Yao, M.; Ren, H.; Wang, N.; Komarneni, S., Nanocomposites of hierarchical ultrathin MnO2 nanosheets/hollow carbon nanofibers for high-performance asymmetric supercapacitors. *Applied Surface Science* **2019,** *463*, 931-938.

162. Bandyopadhyay, P.; Kuila, T.; Balamurugan, J.; Nguyen, T. T.; Kim, N. H.; Lee, J. H., Facile synthesis of novel sulfonated polyaniline functionalized graphene using m-aminobenzene sulfonic acid for asymmetric supercapacitor application. *Chemical Engineering Journal* **2017,** *308*, 1174-1184.

163. Li, D.; Kaner, R. B., Materials science. Graphene-based materials. *Science* **2008,** *320* (5880), 1170-1.

164. Mao, J.; Iocozzia, J.; Huang, J.; Meng, K.; Lai, Y.; Lin, Z., Graphene aerogels for efficient energy storage and conversion. *Energy Environ. Sci.* **2018,** *11* (4), 772-799.

165. Lee, J. H.; Park, N.; Kim, B. G.; Jung, D. S.; Im, K.; Hur, J.; Choi, J. W., Restacking-inhibited 3D reduced graphene oxide for high performance supercapacitor electrodes. *ACS Nano* **2013,** *7* (10), 9366-74.

166. He, S.; Chen, W., 3D graphene nanomaterials for binder-free supercapacitors: scientific design for enhanced performance. *Nanoscale* **2015,** *7* (16), 6957-90.

167. Xu, Y.; Sheng, K.; Li, C.; Shi, G., Self-assembled graphene hydrogel via a one-step hydrothermal process. *ACS Nano* **2010,** *4* (7), 4324-30.

168. Fang, Q.; Shen, Y.; Chen, B., Synthesis, decoration and properties of three-dimensional graphene-based macrostructures: a review. *Chemical Engineering Journal* **2015,** *264*, 753-771.

169. Lin, Y.; Zhang, K.; Chen, W.; Liu, Y.; Geng, Z.; Zeng, J.; Pan, N.; Yan, L.; Wang, X.; Hou, J. G., Dramatically enhanced photoresponse of reduced graphene oxide with linker-free anchored CdSe nanoparticles. *ACS Nano* **2010,** *4* (6), 3033-8.

170. Qiu, B.; Xing, M.; Zhang, J., Mesoporous TiO2 nanocrystals grown in situ on graphene aerogels for high photocatalysis and lithium-ion batteries. *J Am Chem Soc* **2014,** *136* (16), 5852-5.

171. Wu, Z.-S.; Yang, S.; Sun, Y.; Parvez, K.; Feng, X.; Müllen, K., 3D nitrogen-doped graphene aerogel-supported Fe3O4 nanoparticles as efficient electrocatalysts for the oxygen reduction reaction. *J. Am. Chem. Soc.* **2012,** *134* (22), 9082-9085.

172. Yilmaz, G.; Lu, X.; Ho, G. W., Cross-linker mediated formation of sulfur-functionalized V 2 O 5/graphene aerogels and their enhanced pseudocapacitive performance. *Nanoscale* **2017,** *9* (2), 802-811.

173. Chen, K.; Xue, D., In-situ electrochemical route to aerogel electrode materials of graphene and hexagonal CeO(2). *Journal of Colloid and Interface Science* **2015,** *446*, 77-83.

174. Garcia-Bordeje, E.; Victor-Roman, S.; Sanahuja-Parejo, O.; Benito, A. M.; Maser, W. K., Control of the microstructure and surface chemistry of graphene aerogels via pH and time manipulation by a hydrothermal method. *Nanoscale* **2018,** *10* (7), 3526-3539.

175. Seal, S.; Jeyaranjan, A.; Neal, C. J.; Kumar, U.; Sakthivel, T. S.; Sayle, D. C., Engineered defects in cerium oxides: tuning chemical reactivity for biomedical, environmental, & energy applications. *Nanoscale* **2020**.

176. Cong, H. P.; Ren, X. C.; Wang, P.; Yu, S. H., Macroscopic multifunctional graphene-based hydrogels and aerogels by a metal ion induced self-assembly process. *ACS Nano* **2012,** *6* (3), 2693-703.

177. Shin, H.-J.; Kim, K. K.; Benayad, A.; Yoon, S.-M.; Park, H. K.; Jung, I.-S.; Jin, M. H.; Jeong, H.-K.; Kim, J. M.; Choi, J.-Y., Efficient reduction of graphite oxide by sodium borohydride and its effect on electrical conductance. *Advanced Functional Materials* **2009,** *19* (12), 1987-1992.

178. Jung, S. M.; Mafra, D. L.; Lin, C. T.; Jung, H. Y.; Kong, J., Controlled porous structures of graphene aerogels and their effect on supercapacitor performance. *Nanoscale* **2015,** *7* (10), 4386-93.

179. Ye, S.; Feng, J.; Wu, P., Deposition of three-dimensional graphene aerogel on nickel foam as a binder-free supercapacitor electrode. *ACS Appl. Mater. Interfaces* **2013,** *5* (15), 7122-9.

180. Liu, J.; Wang, J.; Xu, C.; Jiang, H.; Li, C.; Zhang, L.; Lin, J.; Shen, Z. X., Advanced Energy Storage Devices: Basic Principles, Analytical Methods, and Rational Materials Design. *Adv Sci (Weinh)* **2018,** *5* (1), 1700322.

181. Liu, C.; Gillette, E. I.; Chen, X.; Pearse, A. J.; Kozen, A. C.; Schroeder, M. A.; Gregorczyk, K. E.; Lee, S. B.; Rubloff, G. W., An all-in-one nanopore battery array. *Nat Nanotechnol* **2014,** *9* (12), 1031-9.

182. Brezesinski, T.; Wang, J.; Tolbert, S. H.; Dunn, B., Ordered mesoporous α-MoO 3 with iso-oriented nanocrystalline walls for thin-film pseudocapacitors. *Nature materials* **2010,** *9* (2), 146-151.

183. Cherusseri, J.; Sambath Kumar, K.; Pandey, D.; Barrios, E.; Thomas, J., Vertically Aligned Graphene-Carbon Fiber Hybrid Electrodes with Superlong Cycling Stability for Flexible Supercapacitors. *Small* **2019,** *15* (44), e1902606.

184. Ardizzone, S.; Fregonara, G.; Trasatti, S., “Inner” and “outer” active surface of RuO2 electrodes. *Electrochimica Acta* **1990,** *35* (1), 263-267.

185. Vogt, H., Note on a method to interrelate inner and outer electrode areas. *Electrochimica Acta* **1994,** *39* (13), 1981-1983.